AN ABSTRACT OF THE DISSERTATION OF

Xingfeng Wang for the degree of Doctor of Philosophy in Chemistry presented on September 13, 2017.

Title: New Chemistry for Electrochemical Energy Storage Applications.

Abstract approved:

_____

David (Xiulei) Ji

Electrochemical capacitors and batteries are two major electrochemical energy storage technologies, which have been investigated extensively to meet the rapidly-growing demand for higher energy, higher power, lower cost and enhanced safety in the past few decades. With the charge storage mechanism of electrostatic charge adsorption/desorption via electrical double layers, electrochemical capacitors deliver higher power, but store less energy, compared to batteries, where redox reactions usually take place inside bulk electrode materials. Depending on the electrolytes, electrochemical capacitors can be divided into aqueous and non-aqueous capacitors. Aqueous electrolytes are more electrically conductive, non-flammable, and more sustainable, compared to non-aqueous electrolytes. However, non-aqueous electrolytes are overwhelmingly dominating the electrochemical capacitor markets, because they provide a larger electrochemical window, and consequently enable capacitors to store more energy. To take advantages of aqueous electrolytes and facilitate safer and more sustainable electrochemical capacitors, tremendous research has been conducted to

increase energy density of aqueous capacitors. Traditional approach is to utilize redox-active electrodes, e.g. metal oxide and conducting polymers in pseudocapacitors, most of which increase energy density at the expense of largely sacrificing power and cycle life. It is important to make progress in one performance aspect of electrochemical capacitors, while retaining other desirable properties as much as possible.

There are two effective ways to store more energy in electrochemical capacitors. One is by increasing capacitance, and the other one is by increasing operating voltages.

Higher capacitance can be obtained when introducing redox reactions in electrochemical capacitors. Instead of employing redox-active electrodes, which may experience ion diffusion in solid, aqueous redox-active electrolyte was studied to retain high power while storing more energy. The redox pair of IO_x^-/I^- in 4 M KI and 1 M KOH is reported for the first time, which enables aqueous capacitors to store a maximum energy of 7.1 Wh/kg, on a par with state-of-the-art non-aqueous capacitors, while delivering a maximum power of 6222 W/kg, and retaining 93% capacitance after 14,000 cycles.

Higher operating voltages are realized in aqueous electrochemical capacitors by maintaining pH 1 and pH 10 at the positive and negative electrode, respectively, with a bipolar assembly of ion-exchange membranes. The theoretical electrochemical window of aqueous electrolytes is expanded from 1.23 to 1.76 V. A practical operating voltage of 1.8 V is proved to be safe for aqueous capacitors with the bipolar assembly,

which allows to store a specific energy of 12.7 Wh/kg, as well as retain 97% capacitance after 10,000 cycles.

Although batteries, especially lithium-ion batteries, have been successful in different fields, e.g. portable electronics, electric vehicles, etc., an intrinsic drawback still exists: low abundance of lithium and therefore high cost of lithium-ion batteries. To address this issue, different types of batteries have been studied, which utilize Earth-abundant elements, such as Na, K, Al, etc. In this dissertation, a novel battery is reported, where hydronium ions perform as charge carriers. For the first time, hydronium ions are found to be reversibly stored in 3,4,9,10-perylenetetracarboxylic dianhydride crystals, contributing 85 mAh/g at 1 A/g after an initial conditioning process. As an aqueous battery storing hydronium ions instead of metal cations, it may deliver higher power, significantly lower the battery cost, and increase the margin of safety. Although this technology is not as mature as lithium-ion batteries, it provides new opportunities and possible solutions for future energy storage.

A new deposition technology, namely ambient hydrolysis deposition, is also studied in this dissertation, which enables nanoparticles grown in porous substrate in a simple and cost-effective way. As a proof-of-concept, by controlling the amount of pre-adsorbed water vapor in the porous carbon, various amount of TiO_2 nanoparticles are grown in porous carbon. The TiO_2 nanoparticles can be converted into TiN nanoparticles by nitridation, which improve the electrical conductivity of porous carbon. Electrodes

prepared from porous carbon with TiN nanoparticles coating exhibit enhanced rate capability in electrochemical capacitors.

New Chemistry for Electrochemical Energy Storage Applications

by
Xingfeng Wang

A DISSERTATION

submitted to

Oregon State University

in partial fulfillment of
the requirements for the
degree of

Doctor of Philosophy

Presented September 13, 2017
Commencement June 2018

Doctor of Philosophy dissertation of Xingfeng Wang presented on September 13, 2017

APPROVED:

Major Professor, representing Chemistry

Chair of the Department of Chemistry

Dean of the Graduate School

I understand that my dissertation will become part of the permanent collection of Oregon State University libraries. My signature below authorizes release of my dissertation to any reader upon request.

Xingfeng Wang, Author

ACKNOWLEDGEMENTS

I would like to express my sincere appreciation to my adviser Professor Xiulei Ji, who not only offers me academic advice and guidance, but also sets a good example of diligence, serious research attitude, and non-stop learning. His commitment to the scientific inquiry has always inspired me to probe further into the unknown. His training, advice, and encouragement has been driving me to make progress all through my PhD studies.

I would like to thank my committee member, Professor Michael Lerner, who attended my group meetings and gave insightful and critical suggestions. I would like to thank my committee members, Professor May Nyman, and Professor Chong Fang. I would also like to thank Professor David Hackleman as my graduate council representative member.

I would like to thank Dr. Wei Luo, from whom I saw a great example of an excellent PhD, as well as a good lab citizen. I would like to thank Dr. Raghu Subash Chandrabose, who was always open to discuss and sharing insights. I would like to thank Dr. Bao Wang, Dr. Vadivukarasi Raju, and Dr. Zelang Jian, who were always willing to help, and giving me suggestions. I would also like to thank Dr. Zhenyu Xing, Dr. Clement Bommier, Zhifei Li, Daniel Leonard, Ismael Rodriguez Perez, Heng Jiang, Jessica Hong, and Woochul Shin.

I would like to thank my parents and all my family for always being supportive during my PhD studies. Although they were a few thousands of miles away from me, we mentally stayed together all the time.

Lastly, and most of all, I would like to thank my beloved wife, Lin Ding, for staying together with me, encouraging me, and supporting me.

TABLE OF CONTENTS

Page

TABLE OF CONTENTS (Continued)

Page

LIST OF FIGURES

Figure Page

LIST OF FIGURES (Continued)

Figure Page

LIST OF FIGURES (Continued)

LIST OF FIGURES (Continued)

Figure Page

LIST OF FIGURES (Continued)

Figure Page

LIST OF FIGURES (Continued)

Figure Page

LIST OF TABLES

1 Introduction

1.1 Background

The fast-growing population and rapid development of society lead to increasing demand for energy. The total global consumption of marketed energy is projected to expand from 549 quadrillion British thermal units (Btu) in 2012 to 815 quadrillion Btu in 2040, accounting for 48% increase from 2012 to 2040.[1] Fossil fuels, includes coal, gasoline, natural gas, etc., have been the primary energy source up till now, taking 81% share of primary energy in 2014, and are predicted to account for 78% in 2040.[1] Although fossil fuels largely meet the fast-paced growth of energy demand, there are concerns regarding their limited abundance and more importantly, the environmental issues, such as air pollution and global warming.

Greenhouse gases emissions are the main cause of global warming. As an example, world CO_2 emissions from energy generation/consumption are 32.3 billion metric tons in 2012, and predicted to be 43.2 billion metric tons in 2040.[1] Considerable attention has been drawn to the climate change caused by greenhouse gases emissions. To tackle this problem, Paris Agreement has been signed by 194 members from United Nations Framework Convention on Climate Change (UNFCCC), aiming at limiting the global temperature increase.

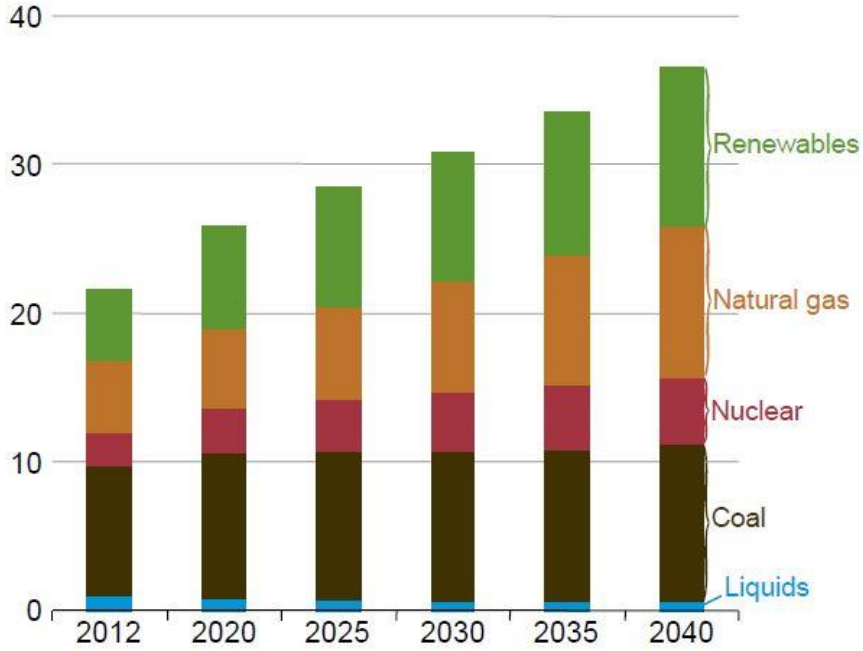

Figure 1.1 World net electricity generation by energy source, 2012–40 (trillion kilowatthours)[1]

In order to meet the fast-growing energy demand without sacrificing environment, renewable energy is expected to replace fossil fuels wherever it is available. From **Figure 1.1**, apparently, coal, the least clean energy resource, is projected to take less market share in world electricity generation, which decreases from 40% in 2012 to 29% in 2040, whereas the market share of renewables (hydropower, wind energy, solar energy, etc.) increases from 22% in 2012 to 29% in 2040.

Figure 1.2 shows the cost reduction in the past few years. Apparently cost of wind energy and solar energy have been falling constantly, due to the technology development and government support.[2] The cost reduction by no means will help

accelerate the deployment of renewable energy, which hopefully can improve the environment and slow down global warming.

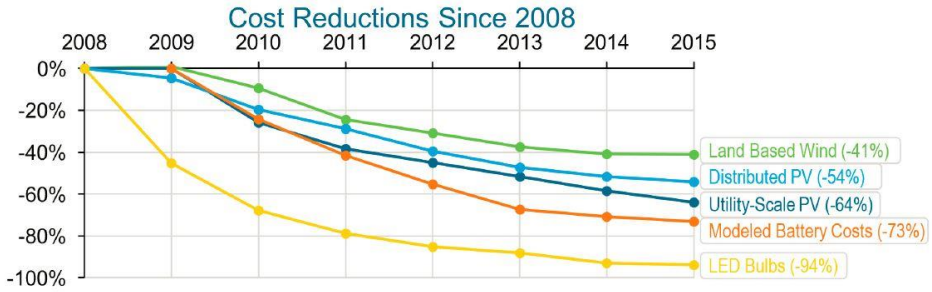

Figure 1.2 Cost reduction of five clean energy technologies[2]

Albeit renewable energy is superior clean, and shows unlimited abundance, an inevitable issue is its intermittency, as well as lack of portability. Electrochemical energy storage, offers wonderful solutions, which is crucial in the energy evolution. In the family of electrochemical energy storage devices, supercapacitors and batteries are two key members, which are investigated and discussed in this dissertation.

1.2 Capacitors

Electrochemical capacitors (ECs), also known as supercapacitors or ultracapacitors, can deliver and uptake high power, with superior cycling life, therefore provide complementary energy storage solution to batteries. Due to their fast charge/discharge (in a few seconds) and excellent reliability and safety, ECs have been widely used in uninterruptable power supplies (UPS), load-leveling, emergency doors on airplanes, cranes, and even electric buses.

1.2.1 History of capacitors

The early version of capacitors is called Leyden jar, which was built in 1740s and named after the town where it was discovered. As shown in

Figure 1.3, it is a glass jar with metal foil attached to the inside and outside bottom part of the jar, and a chain connecting inside foil to the top, as a lead to charge it.[3] The metal foil acts as electrodes, where opposite charges can accumulate upon charging. Opposite charges cannot mix and neutralize with each other, because the glass functions as dielectric between two electrodes. Later improvements were made by building parallel-plate capacitors, with two parallel metal plates separated by a layer of dielectric material (glass, air, vacuum).

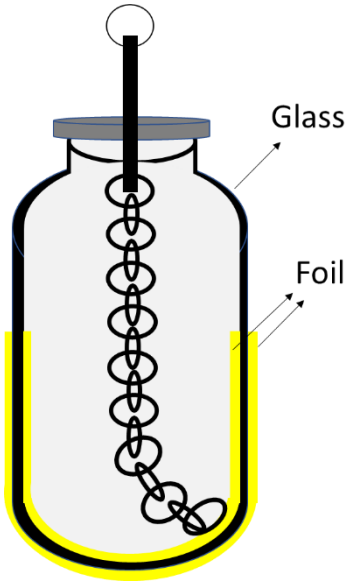

Figure 1.3 Schematic of Leyden jar.

Further development led to the birth of electrolytic capacitors. Metals, such as

aluminum, tantalum, and niobium are used as the anode materials after chemical treatment to increase the surface area. A thin layer of dielectric between anode and cathode, typically metal oxide, is formed when oxidizing electrochemically by applying a positive potential to the anode metal. Cathode covering the dielectric could be in either liquid phase, e.g. aqueous/organic electrolyte, or solid phase, e.g. polymers.

To further enhance the performance and meet different demand, electrical double layer capacitors (EDLCs) and pseudocapacitors are created and considered to be the most popular capacitors in both academia and industry.

1.2.2 Types of Capacitors

1.2.2.1 Electrical Double Layer Capacitors

(I) Mechanism

EDLCs, one of the most popular capacitors, typically employ carbon materials with high specific surface area as the electrodes. During charge/discharge, ions from the electrolyte are reversibly adsorbed/desorbed by electrostatic interaction with electrodes. One equation given by Helmholtz in 1853 is widely used to calculate the capacitance C:

$$C = \frac{\varepsilon_r \varepsilon_0 A}{d}$$

where ε_r is the electrolyte dielectric constant depending on the intrinsic properties of electrolyte, ε_0 is the dielectric constant of the vacuum, A is the surface area of the

electrode, and d is the distance between opposite charges. To enhance capacitance, increasing surface area of electrode materials and reducing charge separation distances are two common strategies. EDLCs deliver overwhelmingly higher capacitance than conventional capacitors, due to the higher surface area of the electrode materials, and the atomic range of charge separation distances.

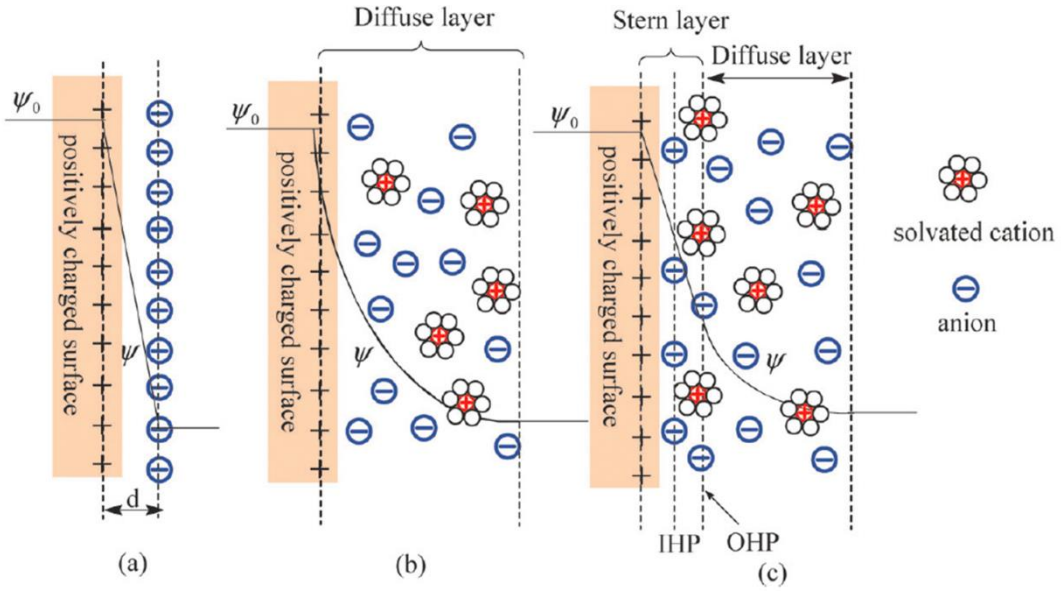

Figure 1.4 Models of electrical double layer at the positive electrode surface: (a) the Helmholtz model, (b) the Gouy-Chapman model, and (c) the Stern model.[4]

As shown in **Figure 1.4**, the early EDL model proposed by von Helmholtz shows one layer of charges on the surface of the electrode, and one layer of opposite charges from ions in the electrolyte. A modified model, Gouy-Chapman model, takes consideration of distribution of cations and anions, therefore introduces the diffuse layer, where the potential decreases exponentially rather than linearly in the former model. Further updates lead to Stern model, which proposes a compact layer, also referred as Stern

layer, in between the electrode surface and diffuse layer. Stern layer includes inner Helmholtz plane (IHP) and outer Helmholtz plane (OHP), which consist of specifically adsorbed ions, and non-specifically adsorbed ions.

(II) Self-discharge

Self-discharge is a significant problem for most capacitors. Without applying a discharge current, the open circuit voltage (OCV) of a capacitor drops spontaneously. Although self-discharge exists in batteries as well, it is way slower due to its thermodynamically stable equilibrium. With ideally polarizable electrodes, self-discharge would not occur, but inevitable Faradaic electron transfer would always cause self-discharge with non-ideally polarizable electrodes. Conway summarized the mechanism of self-discharge, and classified it into five categories.[5]

1. When an EC is overcharged beyond the electrochemical operating window of the electrolyte, electrolyte decomposition would occur and cause self-discharge, until potential drops within electrolyte operating window. For instance, when overcharging an aqueous EC, hydrogen evolution reaction (HER), and/or oxygen evolution reaction (OER) would take place, causing the decrease of OCV. It is also known as activation-controlled self-discharge process.

2. When there are soluble redox-active impurities in the electrolyte/electrode, whose redox potential is within the EC operating potential, the impurities would

act as a redox shuttle, travelling between each electrode, and causing self-discharge. Since impurities exist in small amount, this self-discharge process is typically diffusion-controlled. One typical redox shuttle is Fe^{3+}/Fe^{2+}, although in trace amount, commonly presents in carbon materials and resulting in self-discharge.

3. Surface functional groups, e.g. quinone, which reside on the edge of graphitic domains can also cause self-discharge. However, due to the low concentration and insoluble properties, they typically do not contribute sever self-discharge.

4. Ohmic leakage is another possible reason for self-discharge. When there are ohmic pathways between two electrodes, it is equivalent to a load resistor constantly consuming charges from the EC.

5. It has also been reported that charge redistribution can also cause self-discharge, especially at high charging current. Pores with different geometries are charged at different rates, therefore with different charge densities. At OCV, charge redistribution would take place when self-discharge is observed.

(III) Electrodes

Carbon materials are most widely employed as electrode materials for EDLCs, due to their high abundance, tailorable structure, good electrical conductivity, excellent chemical and electrochemical stability, low cost, and environmental friendliness.

Among all carbon materials, activated carbon (AC) predominates the commercial EDLC electrodes market, primarily due to its high specific surface area and relatively low cost. AC can be prepared from carbon-rich organic precursors, e.g. coconut shell, pitch, wood, or coal. After precursor carbonization under inert gas, selective oxidation is conducted with CO_2, H_2O, or KOH to increase specific surface area to more than 1000 m^2/g. After activation, AC obtains a broad pore size distribution including micropores (<2 nm), mesopores (2 to 50 nm), and macropores (>50 nm). The measured specific capacitance based on electrode materials is in the range of 75 to 175 F/g with aqueous electrolyte, and 40 to 100 F/g with non-aqueous electrolyte.[6]

Although some literature reports AC with a specific surface area of more than 3000 m^2/g, it did not exhibit an incredibly high specific capacitance. It is worth noting that not all the pores are accessibly to ion adsorption/desorption, and specific capacitance is not always proportional to specific surface area of electrode materials. Aurbach proposed ion sieving effect of porous carbon, and concluded that the specific capacitance is contingent upon the relationship between average pore size and effective ion size.[7] Gogotsi and Simon reported detailed studies on the pore size and ion size and their effect on capacitance by controlling pore size of carbide derived carbon and pairing them with electrolyte with different ion sizes (**Figure 1.5**). They concluded that ion desolvation would take place when pore size is smaller than solvated ions and the maximum double layer capacitance is achieved when pore size is close to the ion size.[8,

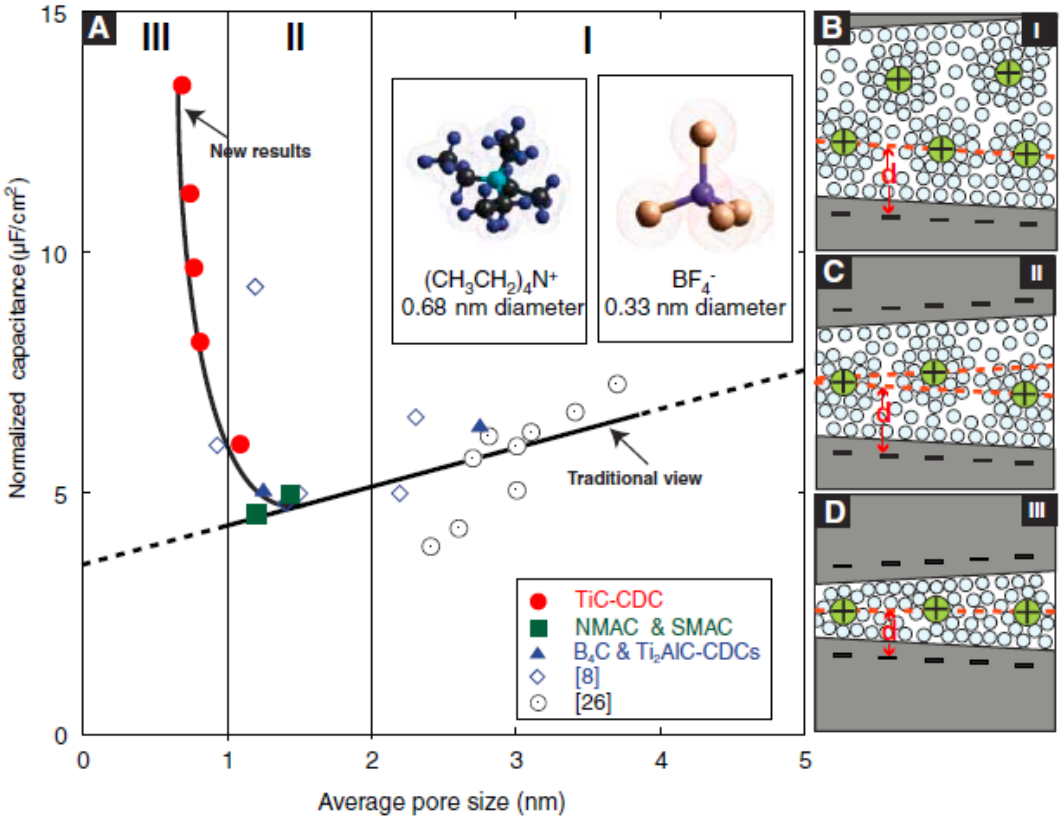

Figure 1.5 Capacitance comparison between porous carbon with different pore size distributions.[9]

Graphene stands out in many carbon materials and has been attracting extensive research interest in the past few years, due to its remarkable electrical conductivity, high surface area, and excellent mechanical properties. These superior properties make graphene a strong candidate of EDLC electrode materials. The theoretical surface area of graphene is as high as 2630 m^2/g, and the intrinsic capacitance of single-layer graphene was reported to be ~21 $\mu F/cm^2$, giving a maximum specific capacitance of ~550 F/g[10]. It was reported that graphene film prepared by laser reduction exhibits as

high as 276 F/g in organic electrolyte.

Carbon nanotubes (CNTs), including single-walled carbon nanotubes (SWNTs) and multi-walled carbon nanotubes (MWNTs), have attracted research interest for energy storage application. Due to their unique structure, CNTs exhibit superior electrical conductivity and provide fast ion migration pathways, therefore are employed as electrode materials for high-power EC applications. However, limited by the specific surface area which is generally less than 500 m^2/g, the specific capacitance and energy density of CNTs are typically less than those of ACs. With aqueous electrolyte, EDLCs based on MWNTs (specific surface area of 430 m^2/g) deliver a specific capacitance of 102 F/g and a specific power of 8 kW/kg.[11]

Templated carbon is another popular electrode material for EC applications, because the pore structure can be well designed and controlled. The general procedure is infiltration of carbon precursors into porous templates, followed by carbonization and template removal. Silica spheres, templated porous silica, and zeolite are widely used as templates to provide porous structure and polymer is the most common type pf carbon precursor. A 3-dimentional hierarchical porous structure can be obtained from templated carbon, which can help enhance the electrochemical performance of ECs. It has been proposed that macropores behave as ion reservoirs, mesopores provide fast ion diffusion pathways, and micropores help enhance charge storage.[12]

To obtain better performance of EDLCs, electrodes with higher surface area accessible to electrolyte is desirable, since they provide more active sites for ion adsorption/desorption and contribute to higher capacitance. Meanwhile, pores with suitable size and structure are important to accommodate ions and allow fast ion diffusion. A balance between surface area and porosity is essential to achieve both high capacitance and high volumetric energy. Furthermore, high electrical conductivity of electrode materials is critical for high power EDLCs.

(IV) Electrolytes

Generally, electrolytes for EDLCs can be classified into three categories: aqueous, organic, and ionic liquid. Ionic conductivity and electrochemical operating window are two key criteria when choosing electrolyte.

Aqueous electrolytes

Aqueous electrolytes usually exhibit greater ionic conductivity due to its high solute concentration and low viscosity. Additionally, with low toxicity, non-flammability and lower cost, numerous papers investigating EDLCs utilize aqueous electrolyte. However, limited by the low electrochemical operating window (1.23 V), aqueous electrolyte is not competitive in the EDLC market. Acidic electrolyte (H_2SO_4) and alkaline electrolyte (KOH) are most widely used in aqueous EDLCs, because they exhibit much higher ionic conductivity than other neutral electrolytes. This can be explained by the unique ion transport mechanism of H^+ and OH^-. As shown in **Figure 1.6**, protons in

water are hydrated and form $H_3O^+(H_2O)_x$. Ion transport follows "Grotthuss mechanism" or "structural diffusion" rather than regular ion diffusion. Briefly, one proton from Eigen ion, $H_3O^+(H_2O)_3$, is transferred and equally shared with one water molecule, forming Zundel ion, $[H_2O\cdot\cdot\cdot H\cdot\cdot\cdot OH_2]^+$, and the proton moves closer to the second water molecule and finally forms another Eigen ion, thus completing charge transfer. Similarly, OH^- can be understood as proton-hole transfer in water. This unique ion transport mechanism gives rise to high ionic conductivity, therefore allowing high power delivery of H_2SO_4 or KOH based EDLCs.

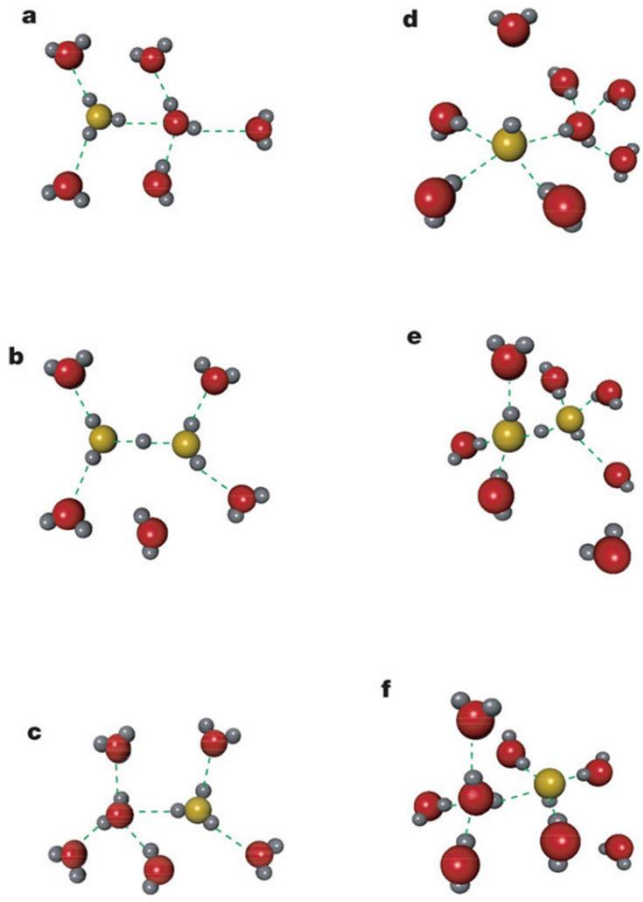

Figure 1.6 Transport mechanism in water of hydrated protons in panels a to c, and hydrated hydroxide ions in panels d to f.[13]

Organic electrolytes

Compared to aqueous electrolyte, organic electrolyte possesses a large voltage window (above 2.5 V), therefore dominates the current EDLC electrolyte market. The energy density of ECs is proportional to voltage squared, indicating a much higher energy when using organic electrolytes. Acetonitrile and propylene carbonate (PC) are two most common organic solvents. Electrolyte with acetonitrile can reach a relatively higher concentration, but its toxicity and harm to environment remain as certain concerns. PC is less harmful to environment, and offers a wider electrochemical window, but the EDLC performance based on PC is more sensitive to temperature due to the high viscosity. The most commonly used solute in organic electrolyte is tetraethylammonium tetrafluoroborate ($TEABF_4$).

Ionic liquids

Ionic liquids (ILs), also known as room temperature molten salts, is considered as another promising electrolyte, and has been attracting considerable research interest in the past few years. ILs are salts in liquid phase at room temperature, dissociating into ions without presence of solvent. A wide electrochemical window over 3 V, superior thermal stability, and non-toxicity provide opportunities of next generation EDLCs with higher energy density and higher operating temperatures. However, owing to the high viscosity and low ionic conductivity at room temperature, further research is needed to replace organic electrolyte with ILs in EDLCs. N-butyl-N-

methylpyrrolidinium bis(trifluromethanesulfonyl)imide ($PYR_{14}TFSI$) is one example of ILs, which can be operated at 3.5 V at 60 ℃ over 40,000 cycles, delivering maximum energy density of 31 Wh/kg when coupling with AC electrodes.[14]

1.2.2.2 Redox-based Electrochemical Capacitors

Charge storage with only electrostatic adsorption/desorption greatly limits the energy density. Therefore, redox reactions are introduced into ECs to enhance charge storage. Pseudocapacitors take advantage of reversible redox reactions at the surface of electrode materials, which significantly increases the capacitance and subsequently energy density. Pseudocapacitive electrode materials include transition metal oxide, functionalized carbon and conducting polymers, etc.

(I) Metal oxide

Ruthenium oxide (RuO_2) is one of the representative of pseudocapacitive materials, because of its high electrical conductivity, and multiple oxidation state of Ru from +2 to +4. Proton electro-adsorption takes place at the surface of RuO_2, accompanying fast electron transfer, as shown in the equation below:

$$RuO_2 + xH^+ + xe \leftrightarrow RuO_{2-x}(OH)_x$$

where $0 \leq x \leq 2$. A specific capacitance of 768 F/g was reported in a symmetric cell with sulfuric acid and at an average voltage of about 1 V.[15] However, high cost and low operating voltage limit its applications. MnO_2 is another pseudocapacitive material, which has been investigated extensively. It was reported that the crystallographic

pathways of MnO_2 play important roles in the electrochemical performance[16]. From **Figure 1.7**, pseudocapacitance of MnO_2 differs significantly when it possesses one-dimensional (1D), two-dimensional (2D), and three-dimensional (3D) channels. It was concluded that a narrow distribution of straight pores, a good match between ion size and pore size, and the interconnectivity of pores are crucial for better pseudocapacitor performance.

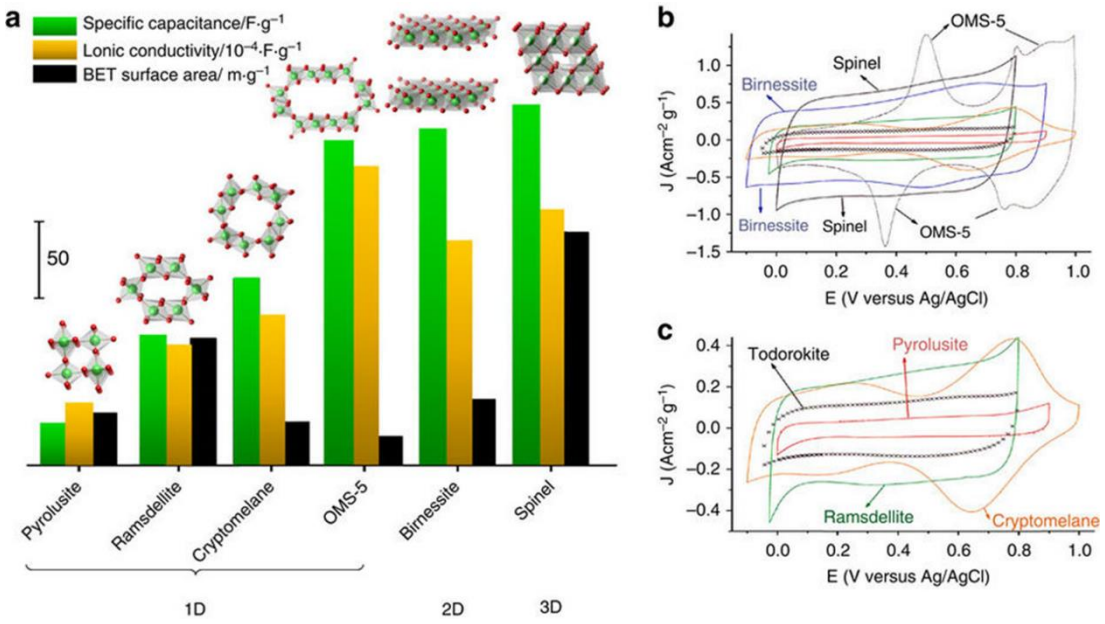

Figure 1.7 (a) Relative values of specific capacitance, ionic conductivity, and BET surface area of MnO_2 in different phases; (b) and (c) CV curves in 0.5 M K_2SO_4 at 5 mV/s of MnO_2 in different phases.[17]

Since redox reactions take place in both pseudocapacitors and batteries, it is important to understand the difference of mechanism and performance. **Figure 1.8** compares the electrochemical performance, mechanism, intrinsic kinetics and lists examples of EDLCs, pseudocapacitors, and batteries. In EDLCs and pseudocapacitors, there is no

diffusion limited process, and therefore *i* (current density) is proportional to *v* (scanning rate), giving either perfect rectangular shape or broad peaks in cyclic voltammetry (CV) profiles. In batteries, on the other hand, *i* is limited by semi-infinite diffusion, thus proportional to $v^{0.5}$, resulting in distinct peaks in CV. Another significant difference between pseudocapacitors and batteries is that electrode materials often experience phase transformation to relax strain caused by dimension change when ion intercalation takes place, while no phase transformation is observed in pseudocapacitive materials.

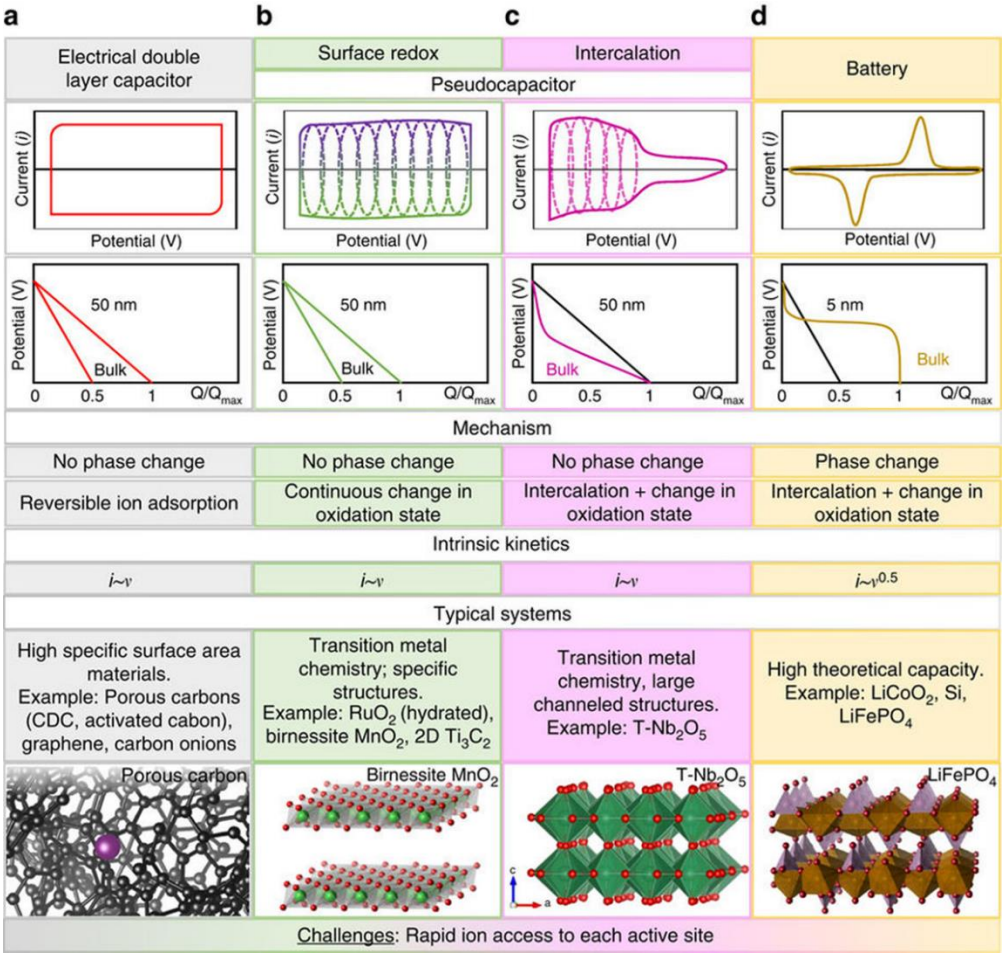

Figure 1.8 Comparison between EDLC, pseudocapacitors, and batteries.[17]

(II) Doping

Introducing heteroatoms into carbon structure is another way to incorporate pseudocapacitance with EDL capacitance and therefore enhance the energy density. Nitrogen doping has been reported as the most effective heteroatom doping for EC applications, because it can (1) creating electrochemically active sites enabling redox reactions, (2) increase the hydrophilicity of carbon materials and the wettability of the electrodes, and (3) act as electron donor groups, and change the electronic structure.

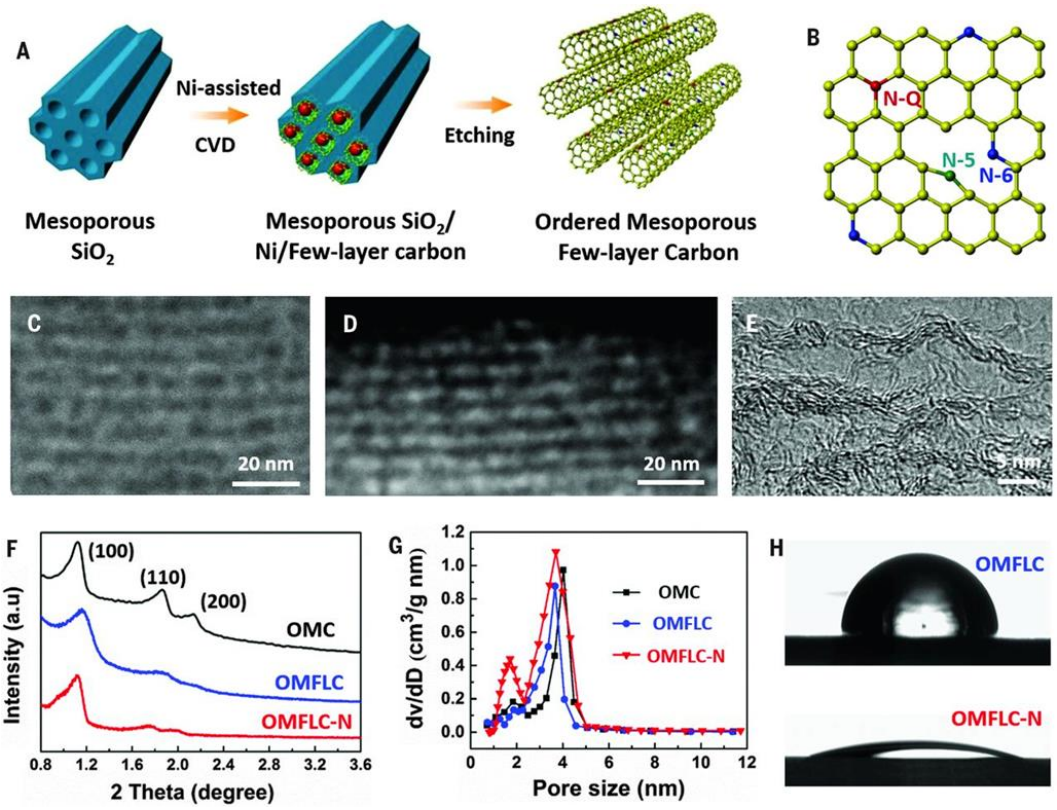

Figure 1.9 Structure of N-doped carbon.[18]

Huang, et al. reported preparation of N-doped mesoporous carbon with a surface area of 1580 m^2/g by chemical vapor deposition (CVD), which exhibited a maximum specific capacitance of 855 F/g, while mesoporous carbon without N-doping only exhibits 325 F/g.[18] As shown in **Figure 1.9**, there are three different nitrogen in the carbon lattice, pyridinic (N-6), pyrrolic (N-5), and graphitic (N-Q). The total nitrogen content ranges from ~8.2 at% to ~11.9 at%. In symmetric cells, when using 2 M Li_2SO_4 aqueous electrolyte, it achieves an energy density of 41 Wh/kg and a power density of 26 kW/kg based active material weight.[18] Other heteroatoms doping include boron doping[19], phosphorous doping[20] and co-doping[20, 21], which all help enhance the electrochemical performance by introducing pseudocapacitance.

(III) Conducting polymers

Conducting polymers (CPs) have been attracting research interest as another type of pseudocapacitive material, due to its high specific capacity, adjustable redox activity, and high operating voltage. Common CPs are polyaniline (PANI), polypyrrol (PPy), polythiophene (PTh) and their derivatives. It was reported that the theoretical specific capacitance of PANI is as high as 2000 F/g, while the measured values from literature are far lower, ranging from 160 to 815 F/g.[22] All CPs must work within a certain voltage window, because they may degrade at a more positive potential, or they may turn into insulating material at a more negative potential. Owing to structural swelling and shrinking of CPs upon ion intercalation/deintercalation, limited cycling stability remains to be a challenge for pure CPs. To maintain the structural integrity and mitigate

mechanical degradation, one effective solution is to fabricate composite electrodes by incorporating CPs with other electrode materials, such as metal oxide, and CNTs, etc.

1.3 Rechargeable Batteries

Different from capacitors, which can deliver superior high power, but low energy, rechargeable batteries are designed to store and deliver much higher energy reversibly, but relatively mild power. There are varieties of batteries with different chemistries going on while operating, such as nickel metal hydride batteries, lead acid batteries, etc., among which the most extensively investigated and developed one is lithium-ion batteries (LIBs).

1.3.1 Li-ion Batteries

Back in 1976, Whittingham reported a fast rechargeable TiS_2/Li cell operating at ~2.2 V[23], when the hope of LIB commercialization was first seen. Unfortunately, due to the uneven plating of Li upon cell charging, sever safety problem caused by Li dendrite block the realization of LIB commercialization. The dendrite caused safety issue was resolved by the discovery of reversible Li insertion in to graphite by Rachid Yazami[24] Meanwhile, Goodenough reported reversible Li extraction from $LiCoO_2$ and $LiNiO_2$ at ~4.0 V. The first full cell was assembled by Yoshino, where $Li_{1-x}CoO_2$ was the cathode and graphite was the anode, (**Figure 1.10**) and it was first commercialized by SONY.

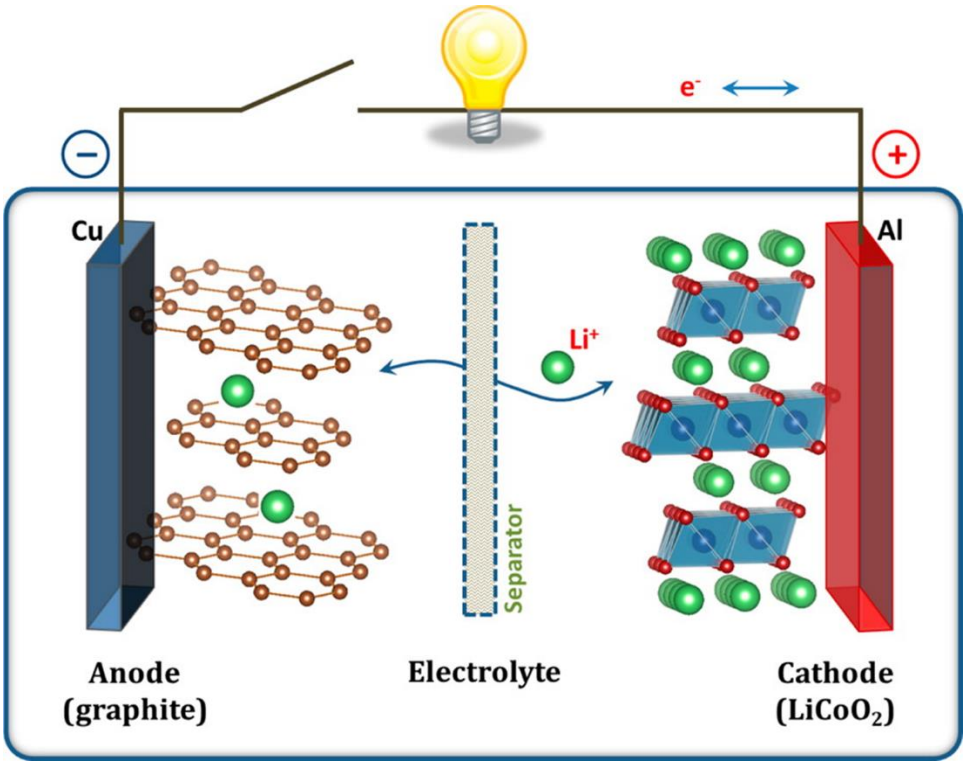

Figure 1.10 Schematic illustration of the first Li-ion battery.[25]

Figure 1.11 describes the energy levels of electrolyte and each electrode. If the electrochemical potential of anode (μ_a) is higher than the lowest unoccupied molecular orbital (LUMO) of electrolyte, electrons from anode would flow into LUMO and consequently reduce electrolyte. Therefore, large electrochemical window of electrolyte and appropriate electrochemical potential of each electrode are critical for high voltage batteries. From **Figure 1.11**, there is an overlapping region between Co^{4+}/Co^{3+}, indicating that before Co^{3+} is completely oxidized to Co^{4+} so that Li^+ is fully extracted, O^{2-} would be oxidized into O_2. That's why x should be kept less than 0.55

for safety purposes.

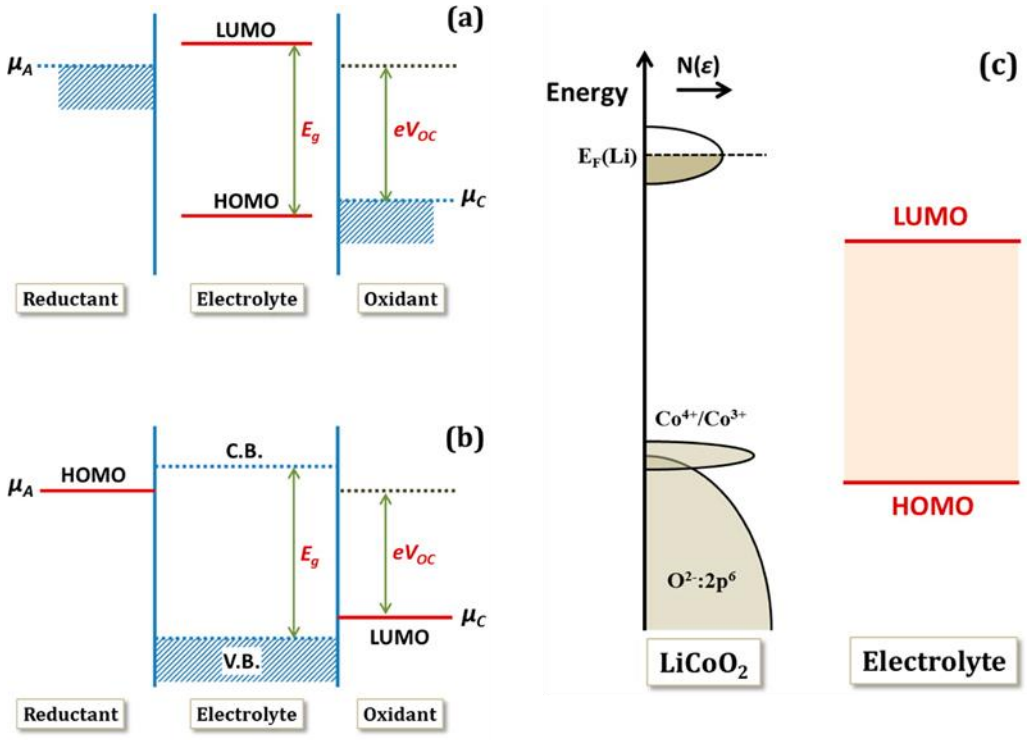

Figure 1.11 Relative energy levels of electrodes and electrolytes in lithium ion batteries.

It can be seen that the Fermi energy of Li is higher than the LUMO of electrolyte, signifying inevitable reduction of organic electrolyte when Li metal is used as the anode. In fact, most anode materials, including graphite, silicon, etc. all have energy levels above electrolyte LUMO, leading to electrolyte reduction a common phenomenon in LIBs. Solid electrolyte interface (SEI) is the product of electrolyte decomposition, which is a Li^+ permeable layer passivating electrodes so that it can prevent electrolyte further decomposition. Ethylene carbonate, and fluoroethylene carbonate are common organic electrolyte additive to form stable SEI. The drawback of SEI formation is the

inevitable consumption of Li^+ from cathode which could result in irreversible loss of cell capacity, and build up the impedance when lithium ions transfer through SEI layer.

SEI forms not only in presence of Li metal, but also when graphite is used as the anode. As lithium ions intercalate into graphite, graphite intercalation compound (GIC) is produced, forming Li_xC, where $0 \leq x \leq 1/6$. The maximum capacity reaches 372 mAh/g when 6 carbon atoms accommodate 1 Li^+. However, this capacity cannot meet the needs of higher energy density, especially for EV applications. Additionally, graphite operates at 0.2 V vs. Li, certain degree of Li plating takes place on graphite at high current, which consequently may form Li dendrite and cause safety concerns. Silicon anodes have been attracting considerable attention due to its high theoretical capacity of 4200 mAh/g, as well as its capability of operating without Li plating even at high current. However, the biggest challenge for Si anodes is its cycling stability is still to be improved, owing to the significant lattice expansion (more than 300%) upon Li insertion. To resolve it, different morphologies of Si nanoparticles, Si composite, surface coating, etc. have been investigated in the past few years.

There are many LIB cathode materials. The conventional cathode is $Li_{1-x}CoO_2$, which is the most-widely-used LIB cathode, where x must be maintained less than 0.55 to ensure no occurrence of oxygen evolution. Moreover, $Li_{1-x}CoO_2$ allows Li^+ 2D conduction due to its layered structure. Differently, Li^+ can transport in 3D direction in spinel structure $[B_2]O_4$, which therefore becomes another interesting type of LIB

cathode materials. $Li_{2x}[Mn_2]O_4$ is one example of spinel LIB cathode, which shows multiple plateaus rather than a single plateau as $Li_{1-x}CoO_2$ does. Multiple plateaus are due to filling Li^+ into different sites, where 2 small plateaus at high potential indicates filling Li^+ into different tetrahedral sites, while the long plateau at lower potential indicates filling Li^+ into octahedral sites.[25] The sharp potential drop when changing from tetrahedral sites to octahedral sites limits one Li^+ per two framework cations in spinel cathodes. Furthermore, when x=0.25 in $Li_{2x}[Mn_2]O_4$, there is enough high concentration of Mn(III) which undergoes disproportionation reaction causing dissolution of Mn(II). When x=0.5, it experiences Jahn-Teller (J-T) distortion, which is an octahedra distortion to reduce electrostatic repulsion. Further development of cathode materials leads to utilization of lithium iron phosphate, $LiFePO_4$, which exhibits improved cycling stability and safety, but lower rate capability, and lithium nickel manganese cobalt oxide (NMC), which delivers higher specific energy and power, and is considered to be the cathode for next generation of LIBs.

To meet the rapidly increasing energy demand in an affordable way, especially for EV evolution and stationary storage, future development of batteries should focus on higher energy density and lower cost. Additionally, chemistry with improved safety is critically important and desirable, as well as replacing environmentally-harmful materials with sustainable and green materials.[26]

As mentioned above, high-cost is one important issue of LIBs to be addressed. As

shown in **Figure 1.12**, the price of Li_2CO_3 have been increasing incredibly in the past three years from ~$6000/t in July 2013 to ~$19000/t in July 2016. The high cost is primarily driven by the limited abundance of Li on Earth, its uneven distribution, as well as rapidly increasing needs. The abundance of Li is 20 ppm in the Earth's crust, and the Li resources concentrate in south America, which are impossible to change. The only solution to lower battery cost is to find alternatives of LIBs. Therefore, batteries with Na^+, K^+, Mg^{2+}, etc. as charge carriers have been attracting more and more attention. Although currently they cannot replace LIBs, they open more directions and provide more opportunities for the next-generation batteries.

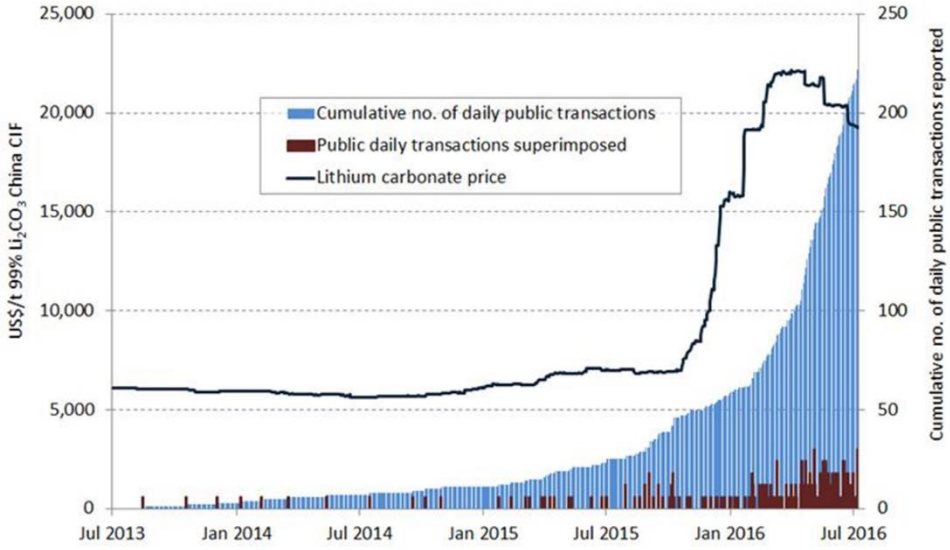

Figure 1.12 Lithium carbonate prices and tenement transactions, July 2013 to July 2016. [27]

1.3.2 Na-ion Batteries

The price of Na_2CO_3 is about $135 to $165/t, significantly lower than Li_2CO_3.[28]. More importantly, sodium is the second-lightest and -smallest alkali metal next to lithium, it shows similar properties as lithium, and thus is a possible alternative of Li. Comparison

of Li^+ and Na^+ is described in **Table 1-1**. Higher atomic mass of Na results in lower specific capacity of the metallic anode. The higher electrochemical potential of Na and its larger ionic radius and therefore different coordination preference undoubtedly have a big influence on the electrode design and performance. Due to the higher atomic mass and higher reduction potential of Na compared to Li, it is less likely to obtain Na-ion batteries (NIBs) with higher energy density and LIBs. However, due to the high abundance and low cost of sodium, NIBs are believed to be promising for large-scale grid storage with further development.

Table 1-1 Comparison between Li^+ and Na^+

	Li^+	**Na^+**
Atomic mass	6.94	23.00
Ionic radius (Å)	0.76	1.02
E° (vs SHE)/V	-3.04	-2.71
Metal capacity (mAh/g)	3862	1165
Coordination preference	Octahedral and tetrahedral	Octahedral and pristamic

Similar to Li, Na also forms dendrite if metallic sodium acts as anode. Moreover, the low melting point of Na (97.7 ℃) is much lower than Li (180.5 ℃), which creates more safety concerns. As a result, other anode materials, rather than metallic Na have been explored. Although graphite has been successfully used as anode for commercial LIBs,

it cannot reversibly host Na^+ and give similar capacity as in LIBs. Bigger ionic radius cannot explain this phenomenon, because larger ions, e.g. reversible intercalation/extraction can take place between K^+ and graphite. Instead of size effect, the relatively higher redox potential Na^+/Na than graphite intercalation may explain it. Sodium plating takes place before Na^+ intercalates into graphite, therefore, it is difficult to see electrochemical intercalation of Na^+ into graphite. Instead of small capacity of only 35 mAh/g with graphite, non-graphitizable carbon, also referred to as hard carbon, exhibits promising Na^+ storage capacity of above 250 mAh/g.[29]

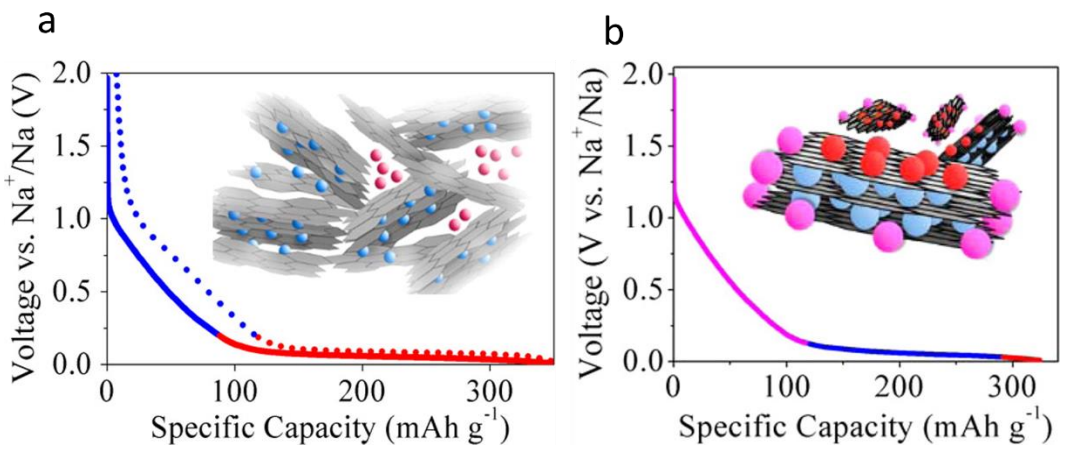

Figure 1.13 (a) Traditional card-house model and (b) recently proposed model of Na-ion storage mechanism. [30]

Figure 1.13 (a) shows the typical profile of Na^+ storage in hard carbon, which is consist of a sloping region below 1 V and a plateau region at lower potential. The mechanism was explained by card-house model, where Na^+ storing in interlayer space of graphitic domains corresponds to the sloping region, while storage in the "pores" between domains corresponds to the low-potential plateau. However, a new mechanism is

proposed recently correlating the Na^+ storage with charge/discharge profiles. As shown in **Figure 1.13** (b), the sloping region indicates Na^+ storage in the defect sites on the turbostratic domain edge, and the main part of plateau region is due to Na^+ intercalation between graphene sheets, and a small portion of plateau is due to Na^+ adsorption onto pore surfaces.

To improve the sodium storage capacity, preparation with different carbon precursors, design various morphologies, and doping heteroatoms have been exploited extensively. A reversible capacity of 355 mAh/g was reported by hard carbon derived from banana peels[31], and 359 mAh/g was reported by doping PO_x clusters in hard carbon.[32] Other NIB anodes that have been reported are $Na_2Ti_3O_7$, which operates at 0.3 V and provides 178 mAh/g[33], and SnSb/C nanocomposites, which exhibits 544 mAh/g.[34]

Cathode materials for NIBs are generally required to operate at high potentials to achieve high energy densities, and experience negligible volume change to ensure cycling stability. Furthermore, since sodium prefer 6-coordination, either octahedral or prismatic, structures available for NIB cathodes are limited at a certain degree, which are primarily consist of polyanionic networks, and layered oxide materials.[28] **Figure 1.14** shows the operating voltage and discharge capacity of various NIB cathodes. Assuming it is coupled with a hard carbon anode with 300 mAh/g, the energy density of NIBs may exceed 300 Wh/kg, comparative to graphite/$LiMn_2O_4$ system.[35]

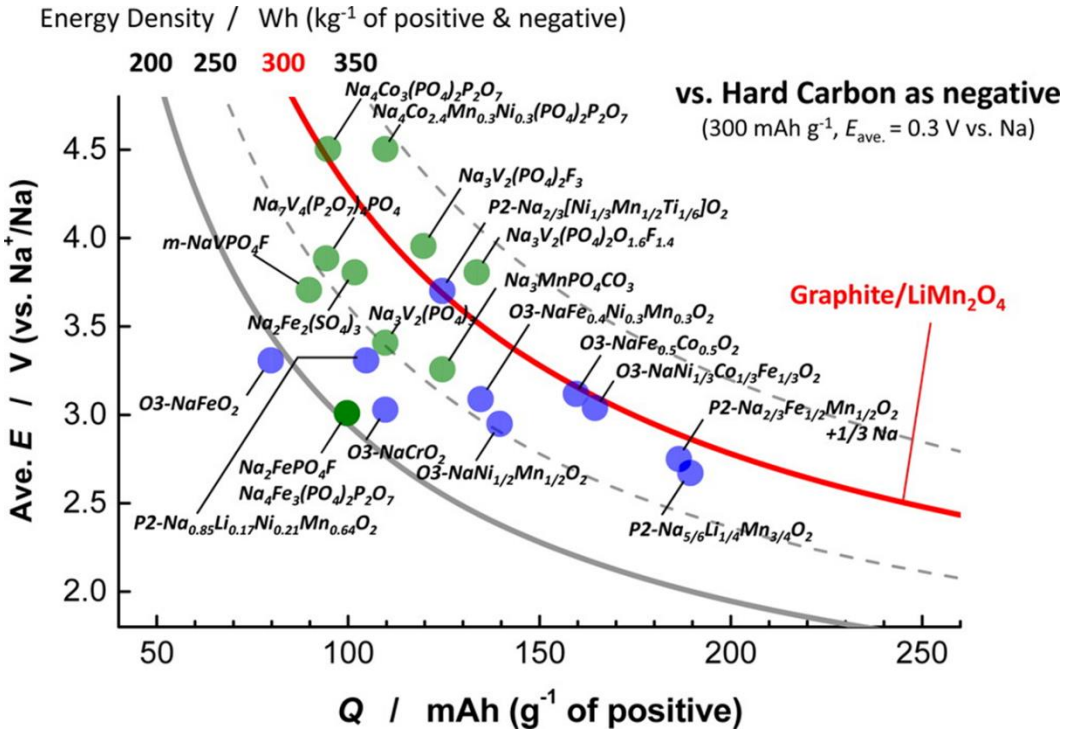

Figure 1.14 Estimated energy density of NIBs based on different cathodes.[35]

In summary, although the energy density, especially volumetric energy of NIBs is less likely to exceed state-of-the-art LIBs, lower cost and potentially higher power of NIBs may give opportunities to NIBs as an alternative of LIBs, especially in electrical grid storage.

1.3.3 K-ion Batteries

K-ion batteries (KIBs), another emerging type of batteries, utilize K^+ as charge carriers rather than Li^+ and Na^+. Potassium ions, although heavier and larger than lithium ions

and sodium ions, have been proved to be promising as charge carriers for battery applications. Because of the larger ionic size, K^+ is a much weaker Lewis acid than Li^+ and Na^+, thus forms smaller solvated ion in solution and require less desolvation energy at the electrode/electrolyte interface. This unique feature facilitates higher ionic conductivity in the electrolyte and fast diffusion kinetics across the electrode/electrolyte interface, which are important criteria for high power batteries. Compared to NIBs, KIBs may provide higher operating voltage and higher energy density, due to the much lower standard electrode potential of K^+/K, -2.936 V vs. SHE, which is 0.222 V lower than that of Na^+/Na. More importantly, the lower potential of K^+/K also lower the possibility of metal plating on the anode, increasing the margin of safety of KIBs.

Carbon materials are of great interest for KIBs. Ji et al. first reported that K^+ could be reversibly stored in graphite, forming potassium GICs in a room-temperature electrochemical cell.[36] *Ex-situ* XRD revealed the formation of GICs at different stages, ranging from KC_{36}, KC_{24}, to KC_8, as shown in **Figure 1.15**. A reversible capacity of over 270 mAh/g was reported, which is pretty close to the theoretical capacity of 279 mAh/g, calculated based on KC_8. However, due to the large size of K^+, a dramatic volume expansion by 61% when graphite is fully potassiated may cause a poor cycle stability. Other carbon materials, e.g. hard carbon and soft carbon, were investigated as anodes for KIBs, which showed improved cycling stability, as well as enhanced rate capability.[36, 37] More than 90% capacity after 200 cycles is maintained in hard carbon,

which most likely originates from the disordered and non-expandable framework of hard carbon. Soft carbon exhibits excellent rate capability, delivering a capacity of 121 mAh/g at 10 C, which may benefit from its higher conductivity and better alignment of graphitic domains. Composite of hard carbon and soft carbon was reported, which exhibits both high rate capability and stable cycle life.[38] Other anode materials for KIBs were studied, including carbon with heteroatom doping,[39, 40] organic compound,[41, 42] and titanium based intercalation materials.[43, 44]

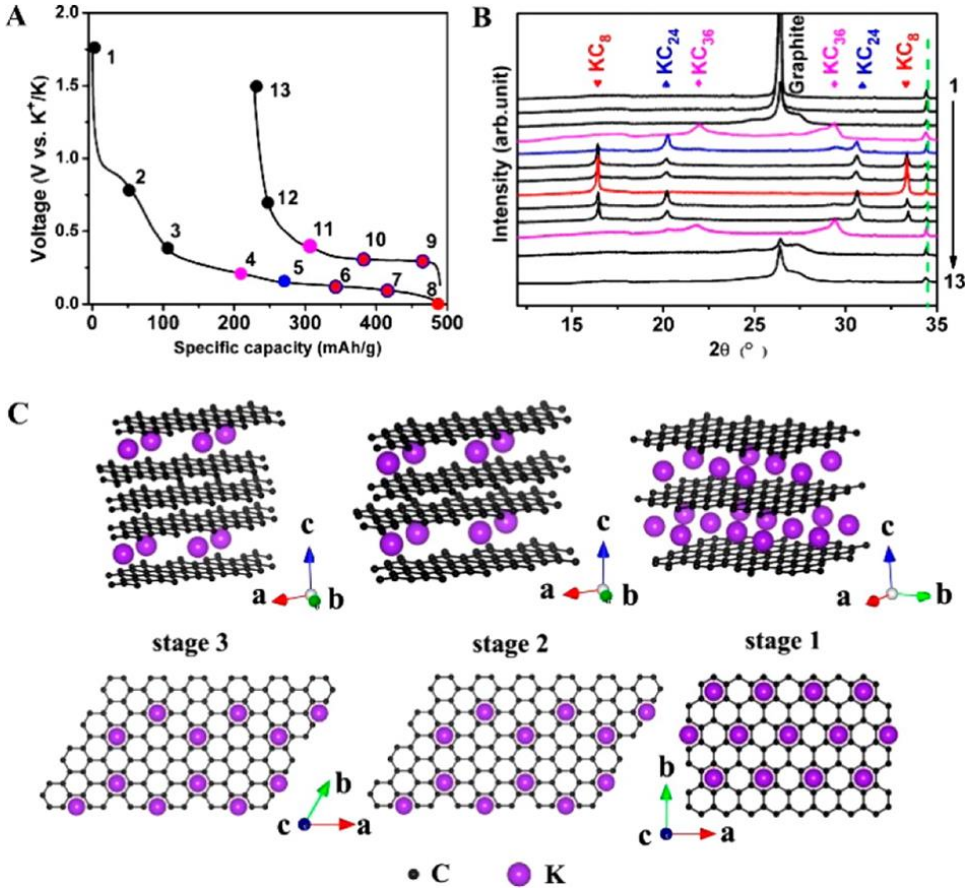

Figure 1.15 GICs at different stages by patassiation/de-patassiation. [36]

Cathode materials for KIBs can be mainly categorized into: Prussian blue analogues, layered metal oxides, polyanionic compounds, and organic crystals. The performances of each cathode are compared in **Figure 1.16**

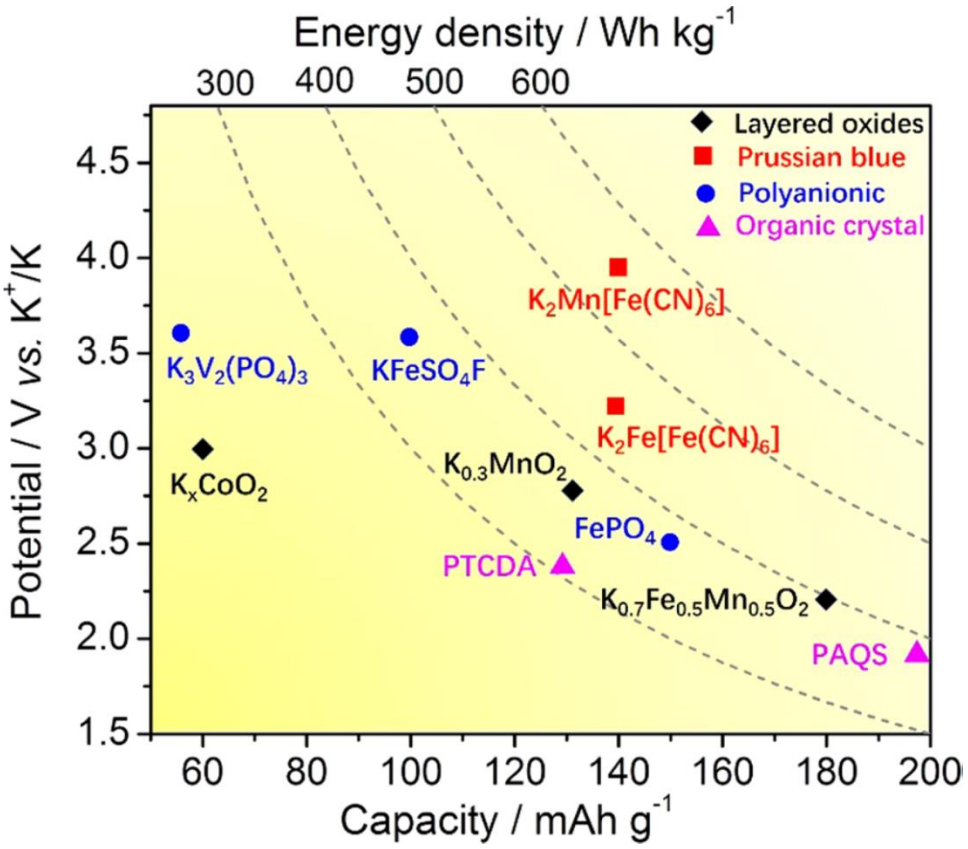

Figure 1.16 KIB cathodes and their operating potential, capacity, and energy density.[45]

Prussian blue analogues, have the chemical formula of $A_xM[Fe(CN)_6]_y \cdot zH_2O$, where A is an alkali metal ion, e.g. Li^+, Na^+, K^+, etc., M is a transition metal ion, e.g. Fe, Mn, Co, Ni, etc., and $0 \leq x \leq 2$. When x=2, 1, and 0, the compound is named as Prussian white, Prussian blue, and Berlin green, respectively. This family of compounds is

typically in face-centered cubic (FCC) lattice and $Fm\bar{3}m$ space group. Benefiting from the open three-dimensional framework and spacious interstitial sites, Prussian blue analogues can accommodate cations with different charges and dimensions, including Li^+, Na^+, K^+, Mg^{2+}, Al^{3+}, etc. Additionally, since both M and Fe are redox-active, Prussian white allows two-electron transfer, as shown in the follow equations.

$$A_2M^{II}[Fe^{II}(CN)_6] \leftrightarrow AM^{III}[Fe^{II}(CN)_6] + A^+ + e^-$$

$$AM^{III}[Fe^{II}(CN)_6] \leftrightarrow M^{III}[Fe^{III}(CN)_6] + A^+ + e^-$$

More importantly, K^+ is highly preferred rather than Li^+ and Na^+ in the Prussian blue structure because of the better fit between the cation size and the Prussian blue cavity. Superior cycling stability of potassium Prussian blue, ~10^6 cycles in cyclic voltammetry[46], and 5000 cycles in galvanostatic charge/discharge[47], have been reported, which are significantly better than lithium Prussian blue. Goodenough et al. first reported the potassium Prussian white of $K_2Mn[Fe(CN)_6]$, which exhibits a capacity of ~140 mAh/g with 90% capacity retention after 100 cycles.[48]. Prussian white $K_xFe[Fe(CN)_6]$ with capacities of 110 to 140 mAh/g were reported as well.[49-51]

Layered oxide materials, such as potassium cobalt oxide, potassium manganese oxide, have been studied as KIB cathodes. However, the large size of K^+ cannot easily fit into these compact layered oxides. Moderate capacity of ~60 mAh/g was reported with K_xCoO_2[52]. K_xMnO_2 was reported to exhibit a high capacity of 136 mAh/g, but suffer

sever fading issue.[53] Improved cycling stability and high capacity were obtained with $K_{0.7}Fe_{0.5}Mn_{0.5}O_2$; however, the discharge potential is much lower than its sodium counterpart.[54] Another type of potassium cathode material is polyanionic compounds, with chemical formula of $AM_x[(XO_4)]_y$, where M is transition metal, e.g. Fe, V, Ti, etc. and X is P, S, etc. It was reported that amorphous $FePO_4$ delivered a high capacity of 156 mAh/g.[55] Advantages of this material are high operating potential, high structural stability and excellent thermal safety. Organic crystals are another attractive KIB cathode candidates, due to their tailorable structure, large interlayer spacing, as well as material sustainability. A reversible capacity of 130 mAh/g was reported with perylene tetracarboxylic dianhydride (PTCDA) for potassium ion storage.[56]

In summary, although KIBs do not show significant promise of higher energy density than LIBs, they may provide practical solutions with lower cost, longer cycle life and higher power, similarly as NIBs. With further improvement in cycling stability and safety, KIBs could be highly competitive in large-scale electric grid storage.

2 Recent Development of ECs

2.1 Redox-active Electrolytes

EDLCs deliver superior power with excellent cycling stability, which batteries cannot provide. However, although high-surface-area carbon serves as the electrode material to enhance specific capacitance and therefore energy density, rapidly increasing demand still calls for higher capacitance. Pseudocapacitors employing redox-active electrode materials, such as MnO_2, V_2O_5, RuO_2, etc. help improve energy density, but all of them either lack electrochemical stability, or cost too much to be widely accepted. Therefore, it would be appealing to introduce redox reactions in a capacitor while maintaining high-surface-area carbon as the electrode material. Redox-active electrolytes may provide a solution.

Lota, et al. reported that iodide (I^-) is redox active in aqueous electrolytes.[57, 58] Note that iodide salts function as both supporting electrolyte providing sufficient ionic conductivities, and redox-active species contributing to higher capacitance. After comparing different counter ions including Li^+, Na^+, K^+, Rb^+, and Cs^+, a maximum cell capacitance of 234 F/g was obtained with KI and CsI in a two-electrode cell configuration.[57] To further study capacitance of iodide at the positive electrode, a three-electrode cell was employed. It was found that at 0.5 A/g, iodide exhibited over 1000 F/g at the positive electrode.[58] **Figure 2.1** shows the cyclic voltammetry and galvanostatic charge-discharge profiles of KI, where strong redox peaks and a flat

plateau are observed from 0 to 0.14 V vs. SCE, respectively. The redox reaction is between iodide and polyiodide. Different performance with different counter cations may result from various interactions of cation-solvent and cation-anion.[57] Stable cycling was also reported, with less than 20% capacitance loss after 10,000 cycles.[58]

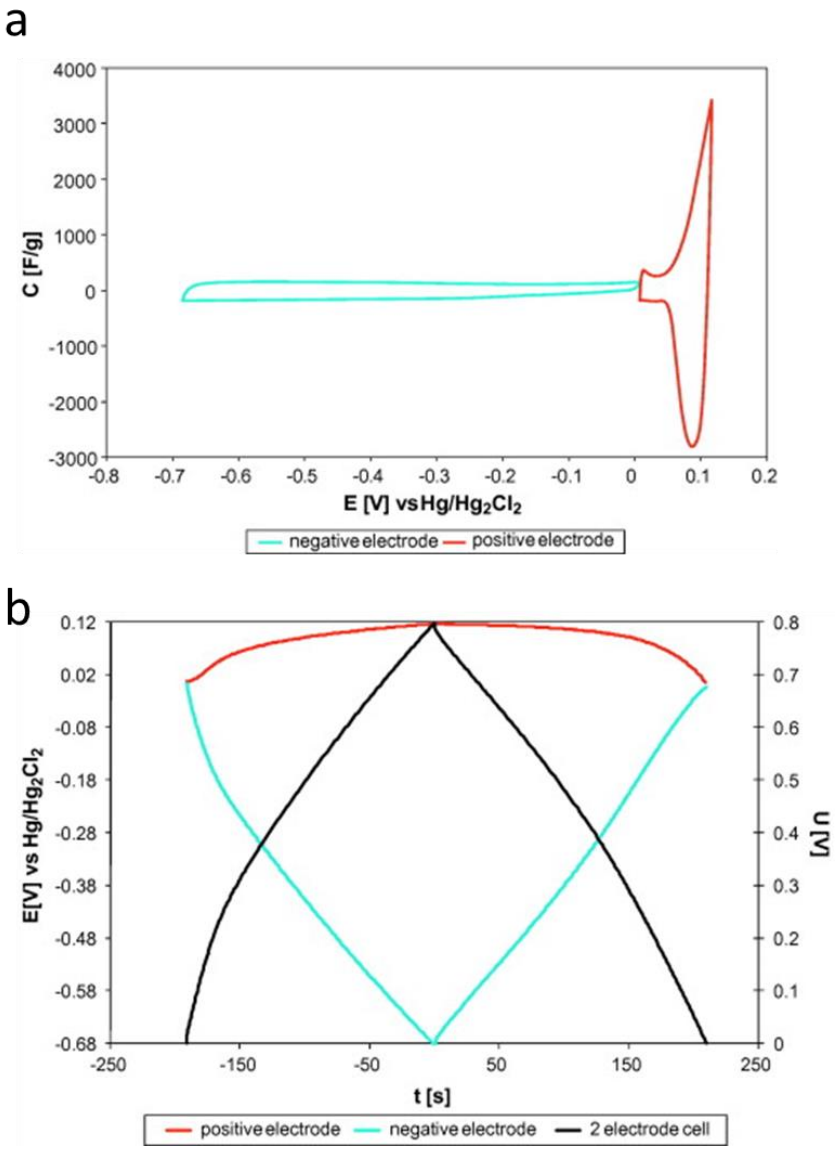

Figure 2.1 (a) CV and (b) GCD profiles of 1 M KI in a three-electrode cell.[58]

It was also reported that addition of KI into H_2SO_4 resulted in a nearly two-fold improved specific capacitance from 472 F/g (1 M H_2SO_4) to 912 F/g (0.08 M KI and 1 M H_2SO_4). However, the discharge profile exhibited low-potential plateau which mainly contributed to the high capacitance but not significantly contributed to high energy. Excellent cycling stability was obtained, and the capacitance surprisingly increased from 576 F/g to 781 F/g after 4000 cycles.[59] Anomalous capacitance increase over cycling was also observed by Lota, et al., from 235 F/g to 300 F/g after 10,000 cycles. [58] Possible explanation of this phenomenon is either carbon oxidation by iodine[58] or improved access of iodide into pores of electrodes[59]. Self-discharge was tested with KI/H_2SO_4 electrolyte, where voltage dropped significantly in the first 0.5 h from 0.8 V to 0.32 V, counting for 60% voltage drop, and after 0.5 h, the OCV stayed pretty stable. KI added to 1 M Na_2SO_4 and KBr added to 1 M H_2SO_4 were also tested, which gave 604 F/g and 572 F/g, respectively.

Inspired by the ionic species in vanadium redox flow batteries, VO^{2+}/VO_2^{+} redox couple was investigated as redox additives in EC electrolytes.[60] It was reported that addition of $VOSO_4$ to 1 M H_2SO_4 lead to a specific capacitance of 630.6 F/g, corresponding to 43% capacitance increase compared to 1 M H_2SO_4 (440.6 F/g). Capacitance retention of 97.57% after 4000 cycles was also reported. The redox reaction is given by the equation below:

$$VO^{2+} + H_2O \leftrightarrow {VO_2}^{+} + 2H^{+} + e^{-}$$

Higher current response as well as redox humps were observed in CV with addition of $VOSO_4$ into 1 M H_2SO_4. Interestingly, pure $VOSO_4$ showed redox peaks in CV, but with significantly lower current than 1 M H_2SO_4, indicating limited ionic conductivity of $VOSO_4$. It was also pointed out that hydroxyl (-OH) and carbonyl (C=O) functional groups play catalytic roles and enhance reaction kinetics of VO^{2+}/VO_2^+.

Wang, et al. reported a hybrid redox-supercapacitor system with different redox species in the electrolyte, naming catholyte and anolyte respectively. [61] **Figure 2.2** depicts the concept of this system. Briefly, positive charged redox couples (anolyte) approach negative electrode, while negative charged redox couples (catholyte) approach positive electrode, enabling redox reactions, respectively. This design is to store charge at both electrodes rather than single electrode as most literature reported. Furthermore, this design attempts to minimize self-discharge caused by soluble redox species cross contamination, by electrostatic attraction. Considering redox potentials, chemical compatibility, and charge natures, KI and $VOSO_4$ were selected in this system. Electrolytes with different concentration combinations were tested. Higher concentration of KI and $VOSO_4$ showed higher energy density, but declined cycling stability, due to more pronounced self-discharge. With 0.3 M KI and 0.2 M $VOSO_4$, the energy density was reported to be comparable to pseudocapacitors using symmetric oxides/oxides, while still maintaining over 95% capacity retention after 10,000 cycles.[61]

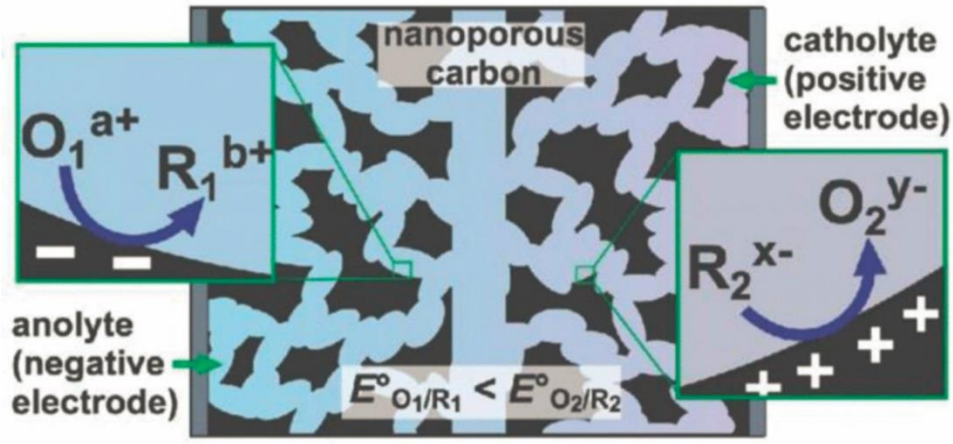

Figure 2.2 Schematic illustration of redox-active catholyte and anolyte in ECs.[61]

In addition to inorganic redox species, organic molecules could be redox active as well. Hydroquinone (HQ) was reported to be an effective redox additive to EC electrolytes.[62] Specific capacitance was compared between using H_2SO_4 and HQ/H_2SO_4 electrolytes with different types of carbon electrodes. The highest capacitance (901 F/g) was obtained with KOH-activated carbon at 2.65 mA/cm^2. With multiwalled carbon nanotubes, the capacitance increased from 21 F/g to 180 F/g when adding HQ to H_2SO_4. The redox reaction is between hydroquinone and quinone, corresponding two-electron transfer per HQ molecule. However, as shown in **Figure 2.3**, the major capacitance increase is from the low-potential plateau, which is of much less practical values. Capacitance loss of 65% after 4000 cycles was also obtained, especially during the first 1000 cycles. It was proposed that the capacitance loss is due to incomplete redox reactions within the operating voltage.

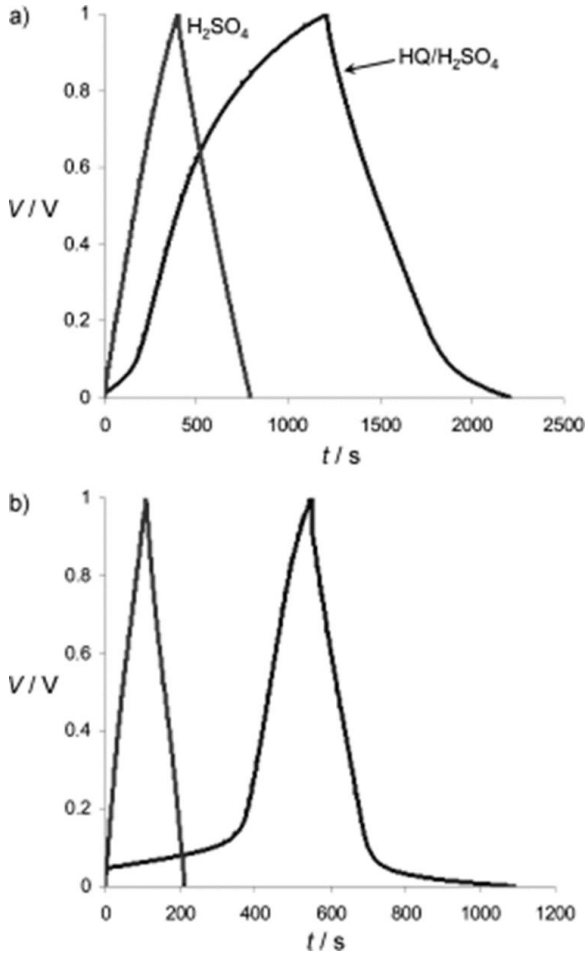

Figure 2.3 GCD profiles of (a) carbon aerogel and (b) MWCNTs in H_2SO_4 (left) and HQ/ H_2SO_4 (right).[62]

Roldán, et al. reported other redox-active organic molecules, such as indigo carmine[63], and methylene blue[64]. Reactions are depicted in **Figure 2.4**. There are two steps of redox reactions with indigo carmine with redox potentials of ~0.4 V and 0.25 V vs. Hg/Hg_2SO_4. When using MWCNT-based electrodes, capacitance values increased from ~20 F/g (H_2SO_4) to 50 F/g (indigo carmine with H_2SO_4). Capacitance retention of this electrolyte is 70% after 10,000 cycles. [63] Methylene blue, with a redox potential of ~0.2 V vs. Hg/Hg_2SO_4, improve the cell capacitance from 5 to 23 F/g when added

to H_2SO_4 electrolyte. [64] After 6000 cycles, about 12% capacitance loss was observed. With both indigo carmine and methylene blue, low-potential plateaus presented in full cell discharge profiles, which largely increased cell capacitance, while increased energy density in a limited degree.

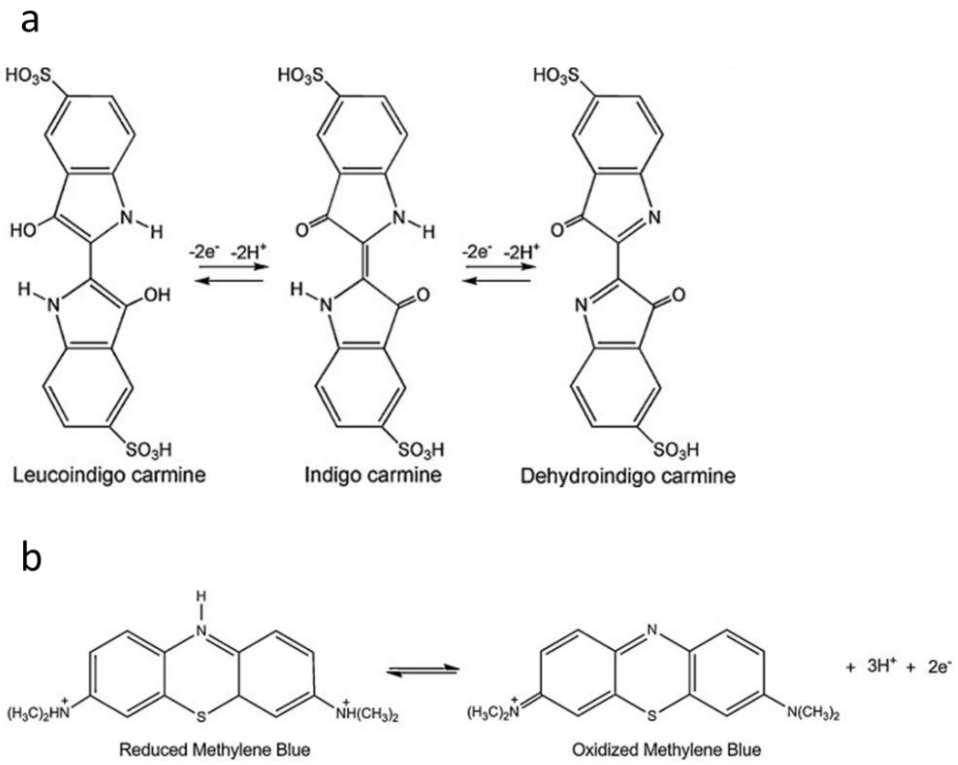

Figure 2.4 Reaction mechanism of (a) indigo carmine[63] and (b) methylene blue[64].

2.2 Increasing Operating Voltage

To enhance the energy density of ECs, in addition to introducing redox reactions, enlarging operating voltage window is another effective approach, due to the fact that energy is proportional to V^2. Aqueous ECs, although offering high power, low cost, and being environmental friendly, attract less attention in the industry because of their low

operating voltage, and consequently limited energy density compared to organic ECs. Water decomposition could be due to either oxygen evolution reaction (OER), or hydrogen evolution reaction (HER). At more positive potentials, water may be oxidized when OER occurs, while at more negative potentials, water may be reduced when HER occurs.

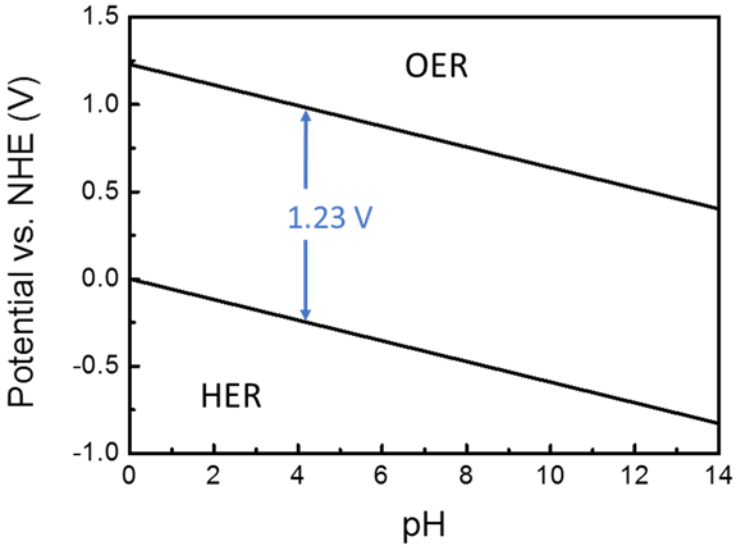

Figure 2.5 Pourbaix diagram of water.

Figure 2.5 is Pourbaix diagram of water, where potentials of OER and HER shifted to the negative direction at the same extent when pH increases. The upper and lower boundaries of electrochemically stable window are therefore two parallel lines with a slope of -0.059, given by Nernst equation. The distance between the two parallel lines is 1.23 V, which is the thermodynamically stable window. Considerable research has been conducted to enlarge the operating potential window of aqueous electrolytes.

Béguin, et al. reported that neutral electrolyte (0.5 M Na_2SO_4) can provide largest operating window of 2.0 V, from the three-electrode cyclic voltammetry test.[65] This significantly larger window was attributed to the high overpotential for di-hydrogen evolution of 0.6 V and nascent hydrogen storage in activated carbon, indicated by the reversible redox humps. The potentials of di-hydrogen production and OER were reported to be -1 V and 0.99 V vs. NHE, respectively. However, in the two-electrode cell configuration, cutoff potentials of each electrodes were -0.61 and 0.99 V vs. NHE, giving the maximum cell voltage of 1.6 V, beyond which OER would be triggered. [65]

Frackowiak, el al. studied different neutral electrolytes with various concentrations, including Li_2SO_4, Na_2SO_4, and K_2SO_4, and found Li_2SO_4 to be a promising aqueous electrolyte operating at high voltages.[66] The maximum operating voltage of 1 M Li_2SO_4 was reported to be 2.2 V in a carbon-based EC, exhibiting 140 F/g and dropped to 120 F/g after 15,000 cycles. This high operating voltage was attributed to the strong solvation of both Li^+ and SO_4^{2-}. The hydration energy of lithium cations and sulfate anions are 160 to 220 kJ/mol, so that number of water molecules surrounding Li^+ and SO_4^{2-} are 27 and 12 to 16, respectively. Since most water molecules were more or less 'bonded' with ions, they were less likely to decompose. However, the maximum voltage was determined by cyclic voltammetry at 10 mV/s, which may not be slow enough to reveal the real value.

Another system to expand the operating voltage window is a hybrid system, consist of a pseudocapacitive electrode and a capacitive electrode. AC/MnO_2 system aroused much research interest in the past, which was reported to operate at 2 V. The reason of the high operating voltage is high overpotentials of HER and OER at AC and MnO_2, respectively. It was reported that the maximum stability window of MnO_2 in 0.65 M K_2SO_4 aqueous electrolyte is between 0 to 1.1 V vs. Ag/AgCl; the onset HER potential is as low as -1.3 V vs. Ag/AgCl.[67]

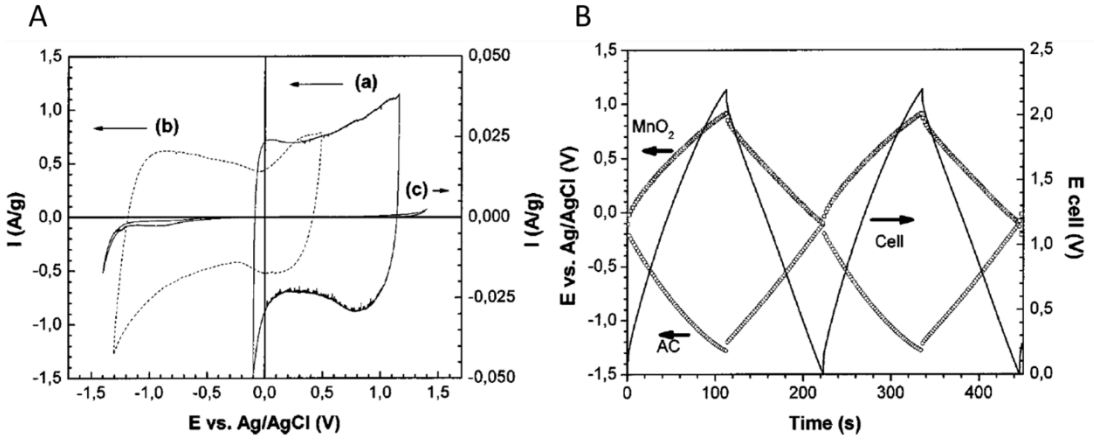

Figure 2.6 (A) CV curves of (a) MnO_2, (b) AC, and (c) Ti grid; (B) GCD profiles in 0.65 M K_2SO_4. [67]

As shown in **Figure 2.6**, both cyclic voltammetry and galvanostatic charge-discharge profiles showed good cell performance at 2.2 V without OER or HER, as well as high coulombic efficiency of nearly 100%. However, Be´langer, et al. realized that 100% coulombic efficiency may not mean completely reversible reactions. It was found that at the cell voltage of 2.2 V, small amount of hydrogen gas was generated at the negative electrode during charge, while dissolution of MnO_2 took place at the positive electrode

during discharge, resulting in “100%” coulombic efficiency. A lower voltage (1.5 V) was proposed to be a safe voltage, where gas evolution is negligible, and the decrease of energy density is only 24% over more than 23,000 cycles. Operating from 0 to 1.5 V, this hybrid capacitor delivered 7.4 Wh/kg with power density of 400 W/kg. The highest energy density and power density were reported to be 8 Wh/kg and 10 kW/kg, respectively.

3 Electrochemical Storage of Proton/Hydrogen

Successful storage of Li^+, Na^+, and K^+ have been demonstrated in batteries, which provides tremendous opportunities for energy storage technologies. Hydrogen, the lightest element, as well as the analog element of Li, Na and K, has been investigated as well in energy storage applications.

3.1 Nickel Metal Hydride Batteries

Nickel metal hydride (NiMH) batteries, operating at ~1.2 V with aqueous electrolytes, stores hydrogen in a solid metal hydride phase. In a NiMH battery, metal alloy and nickel hydroxide act as negative and positive electrode, respectively. Metal hydride electrodes remain metallic before and after hydride formation, exhibiting high electrical conductivity at both charged and discharged states. Since hydrogen atoms are the smallest atoms, they enter the metal lattice without causing much lattice expansion (10%). The reactions during charge are given in the following equations, and the discharge reactions take place in the opposite reactions.

$$M + H_2O + e^- \rightarrow MH + OH^-$$

$$Ni(OH)_2 + OH^- \rightarrow NiOOH + H_2O + e^-$$

Water molecules are reduced at the negative electrode and lose hydrogen to the metal electrode, forming metal hydride (MH); hydroxyl ions take hydrogen from $Ni(OH)_2$, forming water and NiOOH. The metal hydride bond strength is critical, which must be between 6 to 12 kcal/mol.[68] Too strong MH bonds leads to irreversible reactions, where hydrogen cannot be released during discharge, while too weak MH bonds makes it less favorable than hydrogen evolution. One serious problem may come up with cell overcharging, when OER and HER take place at the positive and negative electrodes, respectively. Due to the sealed system, oxygen and hydrogen must recombine at the MH electrode at sufficient rate to avoid internal pressure buildup.[68] Electrode resistance to corrosion and oxidation are also important to ensure stable cell performance. To address the aforementioned issues, other elements are added to MH electrodes. For example, V, Mn, and Zr help to adjust MH bond strength; Al, Mn, Co, Fe, and Ni catalyze both cell reactions and gas recombination reactions; Cr, Mo and W help enhance oxidation and corrosion resistance and electrode conductivities.[68]

3.2 Hydrogen electrochemical storage in carbon materials

One challenge to store hydrogen is the low weight density, which limits the portability of hydrogen utilization. Therefore, research has been conducted to address this issue. The simplest solution is to store hydrogen with light elements, such as carbon.

Carbon nanotubes (CNTs) are likely to accommodate hydrogen atoms, due to their cylindrical and hollow shape. The first publication about hydrogen electrosorption in CNTs was from Schlapbach, et al. in 1999.[69] Both single-wall nanotubes (SWNTs) and multi-wall nanotubes (MWNTs) were studied in 6 M KOH electrolyte in a three-electrode cell. SWNTs exhibited more than 110 mAh/g at a current density less than 10 mA/g. Note that the SWNTs were of low purity, with a considerable amount of amorphous carbon, Fe/Ni alloy, etc.

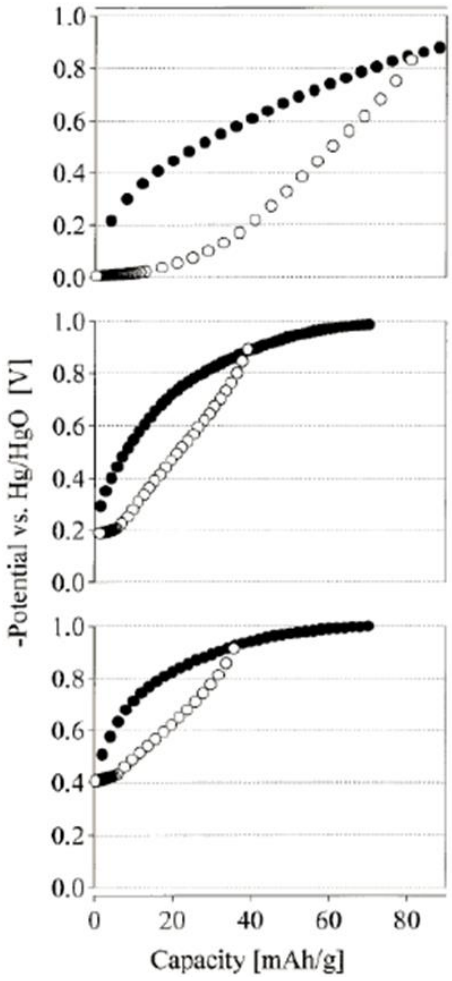

Figure 3.1 GCD profiles of unpurified SWNT/gold electrode in 6 M KOH at different cutoff potentials. [69]

Figure 3.1 shows the equilibrium curves of SWNTs at different cutoff potentials. Different from metal hydride electrodes, hydrogen electrosorption does not show well-defined plateaus because of no phase transitions. The author speculated that higher capacities could be achieved with high-purity SWNTs.

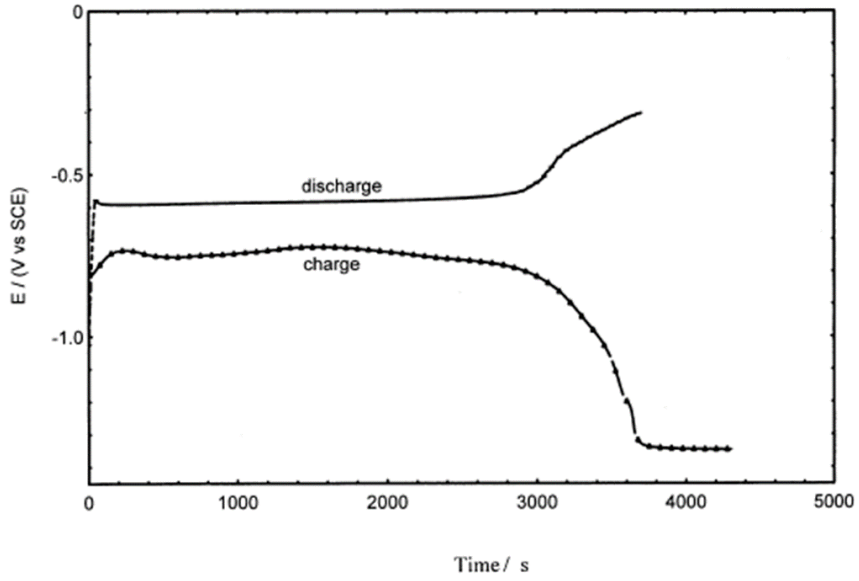

Figure 3.2 GCD profiles of purified SWNT/Cu electrode in 30% KOH.[70]

In 2000, Rajalakshmi, et al. reported a much higher capacity of 800 mAh/g with purified SWNTs, corresponding to 2.9 wt% hydrogen in SWNTs.[70] This significant improvement was explained to be from much higher purity of SWNTs, as much as 80%. Interestingly, as shown in **Figure 3.2**, long plateaus at -0.8 and -0.6 V vs. SCE showed up during charge and discharge, respectively. The coulombic efficiency was calculated to be 85%. Capacity at different current rate was tested as well, which did not vary much from 10 mA to 100 mA. The discharge capacity at beginning three cycles was

found to be around 100 mAh/g, which increased to be more than 800 mAh/g after 20 cycles. It is worth noting that SWNTs-based electrodes reported by both Schlapbach and Rajalakshmi contained 75 to 80 wt% metal powders for stabilization and conductivity purposes. Therefore, the capacity of the SWNTs-based electrodes is limited.

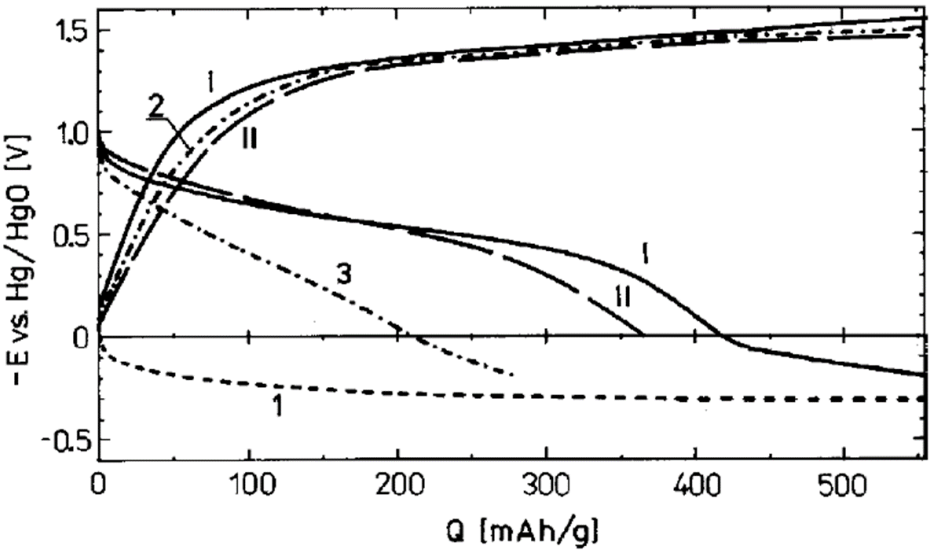

Figure 3.3 Galvanostatic charge (-500 mA/g)/discharge (+100 mA/g) profiles of 1st (I) and 2nd (II) cycle.[71]

In 2001, activated carbon was proposed for hydrogen electrochemical storage by Beguin, et al.[71] When using AC with a specific surface area over 1200 m^2/g in 6 M KOH, the total discharge capacity was measured to be ~400 mAh/g, including contributions from both EDLC and hydrogen sorption. However, no charge capacity values were reported in this paper. The high capacity was attributed to formation of nascent hydrogen which penetrated easily in the carbon nanostructure. In **Figure 3.3**,

well-defined plateaus at -0.5 V vs. Hg/HgO were observed during discharge, indicating hydrogen oxidation and contributing to the high capacity. Capacity loss of about 15% was found during 2nd cycle, which was explained to be from strongly oxidized carbon surface. No further cycling was shown in this article.

In 2004, Beguin reported the study of hydrogen electrosorption with AC in 3 M KOH as well as in 3 M H_2SO_4, where the reaction mechanism was also discussed.[72] After comparing acidic and alkaline electrolytes, it was concluded that reversible hydrogen electrosorption is more favorable to take place in alkaline medium. Possible reactions are given by Equation (1) to Equation (5) when polarizing electrodes to negative potentials. Reaction (1) is known as Volmer reaction, when nascent hydrogen formed by reducing water electrochemically. The nascent hydrogen could adsorb onto carbon surface as shown in reaction (2). Depending on the free energy and activation energy of Heyrovsky reaction (3) and Tafel reaction (4), hydrogen evolution may take place and generate hydrogen gas, interfering reversible hydrogen electrosorption.

$$H_2O + e^- \rightarrow H + OH^- \quad (1)$$

$$C + H \rightarrow CH_{ad} \quad (2)$$

$$CH_{ad} + H_2O + e^- \rightarrow H_2 + OH^- + C \quad (3)$$

$$2H \rightarrow H_2 \quad (4)$$

$$CH_{ad} + CH_{ad} \rightarrow H_2 + 2C \quad (5)$$

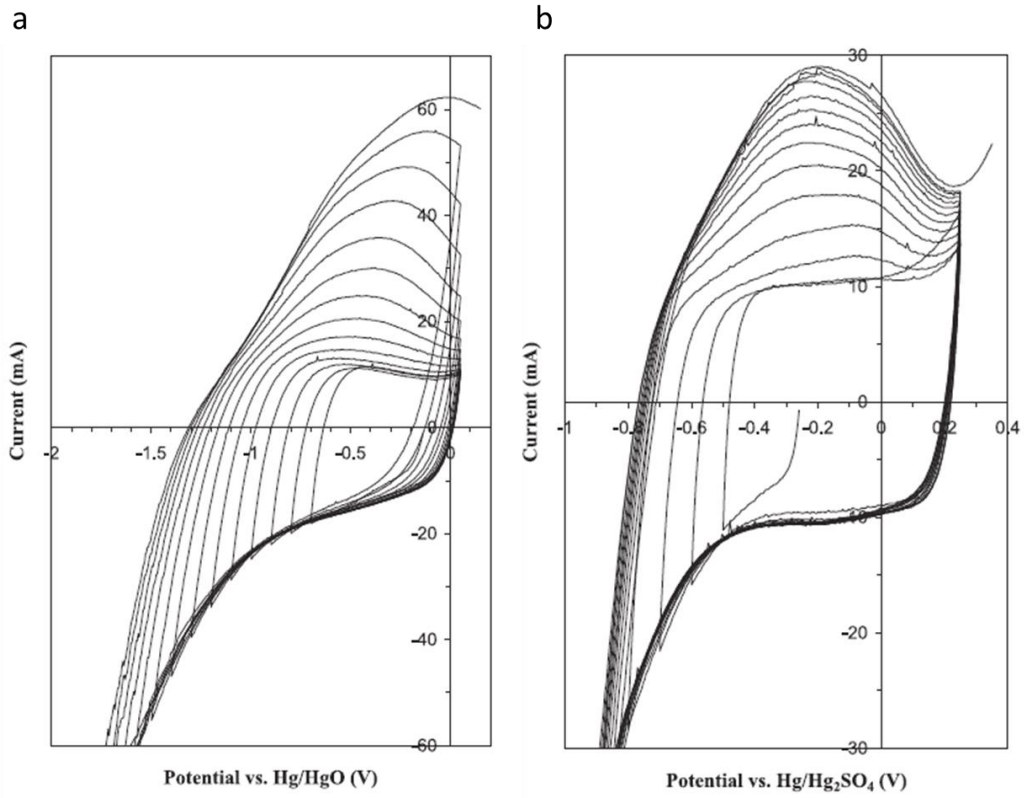

Figure 3.4 CV curves of AC at different cutoff potentials in 3 M KOH (a) and 3 M H_2SO_4.[72]

Figure 3.4 shows cyclic voltammetry results at different cutoff potentials in both alkaline and acidic electrolytes. In 3 M KOH, onset potential of HER is at -0.908 V vs. Hg/HgO (-0.856 V vs. NHE). In **Figure 3.4** (a), with cutoff potentials above -0.8 V vs. Hg/HgO, pure electrical double layers formed at working electrodes. When the cutoff potentials were below -1.5 V vs. Hg/HgO, molecular H_2 was generated. With intermediate cutoff potentials between -0.8 to -1.5 V vs. Hg/HgO was designated where hydrogen electrosorption took place. Humps during anodic scan were attributed to the oxidation of adsorbed hydrogen. In 3 M H_2SO_4, the intermediate region was missing where reversible hydrogen electrosorption occurred. Beyond -0.6 V vs. Hg/Hg_2SO_4,

molecular hydrogen formed. Note that the onset potential for HER in 3 M H_2SO_4 is at -0.566 V vs. Hg/Hg_2SO_4 (0.046 V vs. NHE). It was claimed that the Tafel recombination was quicker than hydrogen diffusion and incorporation into bulk AC. Galvanostatic charge-discharge were tested, with discharge current significantly lower than charge current. The coulombic efficiency was as low as 3%, when charging the cell for sufficiently long time. Cycling stability was not investigated in this system.

A new mechanism was proposed regarding electrochemical hydrogen adsorption in activated carbon by Qu in 2008.[73] By testing different ACs in 30% KOH, no clear correspondence was observed between hydrogen adsorption and surface area, questioning the hydrogen surface adsorption theory. Furthermore, a general trend was found that ACs with higher interlayer spacing exhibited higher hydrogen electrochemical adsorption capacity. This trend lead to the new mechanism proposed, as shown in **Figure 3.5**.

The majority of atomic hydrogen was proposed to stay in the interlayer space of defective graphene layers and the nanopores created by defective single graphene sheets. A minority of atomic hydrogen was proposed to be adsorbed on the edge or basal planes. It was also proposed that the atomic hydrogen intercalation would be the dominant reaction before significant coverage of H at the carbon surface, since the rate of HER was proportional to the degree of H monolayer coverage on the electrode. The discharge capacity from hydrogen adsorption (EDLC contributions excluded) was

measured to be over 70 mAh/g at the coulombic efficiency of more than 80%, when charging at 100 mA/g and discharge at 50 mA/g at the cutoff potential of -1.25 V vs. Hg/HgO. [73] Self-discharge was measured, where half of the initial capacity remained after 48 h at OCV. [73]

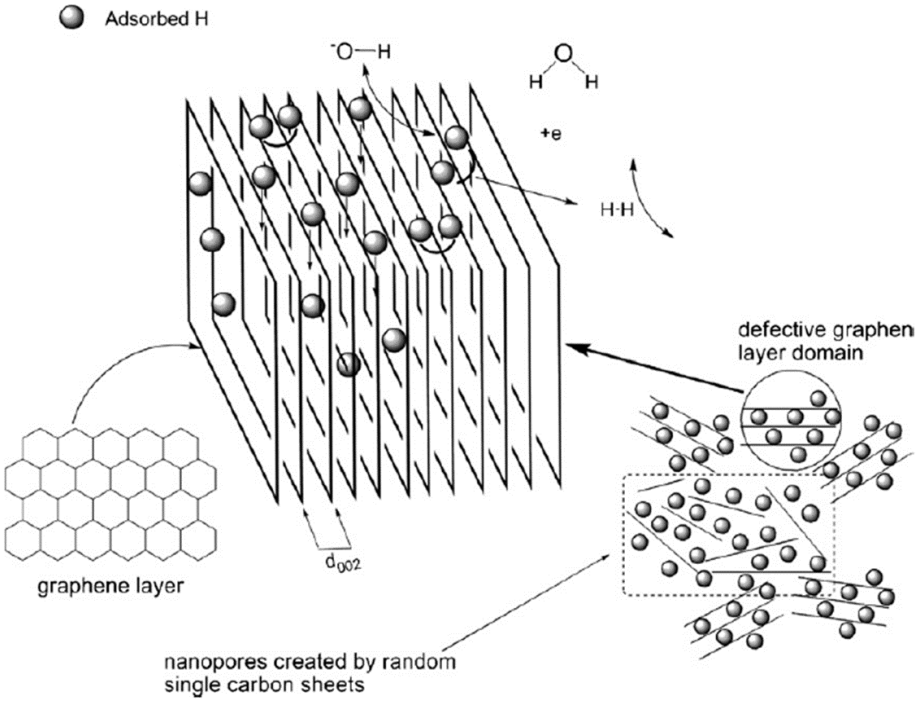

Figure 3.5 Schematic illustration of hydrogen electrochemical insertion mechanism. [73]

3.3 Ruthenium Oxide

Due to the high electronic conductivity, reversible redox activities, and electrocatalytic properties, ruthenium oxide (RuO_2) has been utilized widely, especially as

pseudocapacitor electrode materials, and electrocatalysts. The first report on RuO_2 as an interesting electrode material was back to 1971 by Trasatti and Buzzanca.[74] In 1996, Zheng and Jow reported a capacitance over 600 F/g based on RuO_2, an energy density of 20 Wh/kg at a power density of 10 kW/kg, as well as ~70% capacitance retention after 50,000 cycles.[15] Later studies revealed that Ru could reversibly experience oxidation state from (II) to (IV) within 1.2 V. It was described as a fast and reversible electron-proton transfer process, analogous to Ni^{II}/Ni^{III} in Ni/Cd batteries.[5] It was reported that hydrated RuO_2 exhibited high redox activity rather than non-hydrated RuO_2.[5] The fast redox reactions associated with RuO_2 are attributed to hydrations of RuO_2, facilitating proton transfer via Grotthuss mechanism. The redox reaction of RuO_2 involving proton transfer can be described as follows:

$$RuO_x(OH)_y + \delta H^+ + \delta e^- \leftrightarrow RuO_{x-\delta}(OH)_{y+\delta}$$

However, the reaction mechanism remains controversial. While previous literatures announced the redox process involves only proton exchange presumably between OH^- and O^{2-}, Bulhoes investigated redox reaction of RuO_2 with electrochemical quartz crystal microbalance, and found multiple reaction mechanisms at different potentials.[75]

Characteristic CV curves of RuO_2 in acidic electrolyte is shown in **Figure 3.6** (a), where three pairs of broad redox peaks are observed, dividing the CV curves into three regions, referring to redox reactions between Ru^{2+}/Ru^{3+}, Ru^{3+}/Ru^{4+}, and Ru^{4+}/Ru^{6+}. Reversible

mass change while scanning CV can be seen in **Figure 3.6** (b). However, small mass change is only observed in region II, which is possibly from proton transfer. Region I and Region III both show significant mass variation, which should involve molecules or ions other than protons. Based on the mass change from **Figure 3.6** (b) and the amount of charge from **Figure 3.6** (c), mass per unit charge can be calculated in each region.

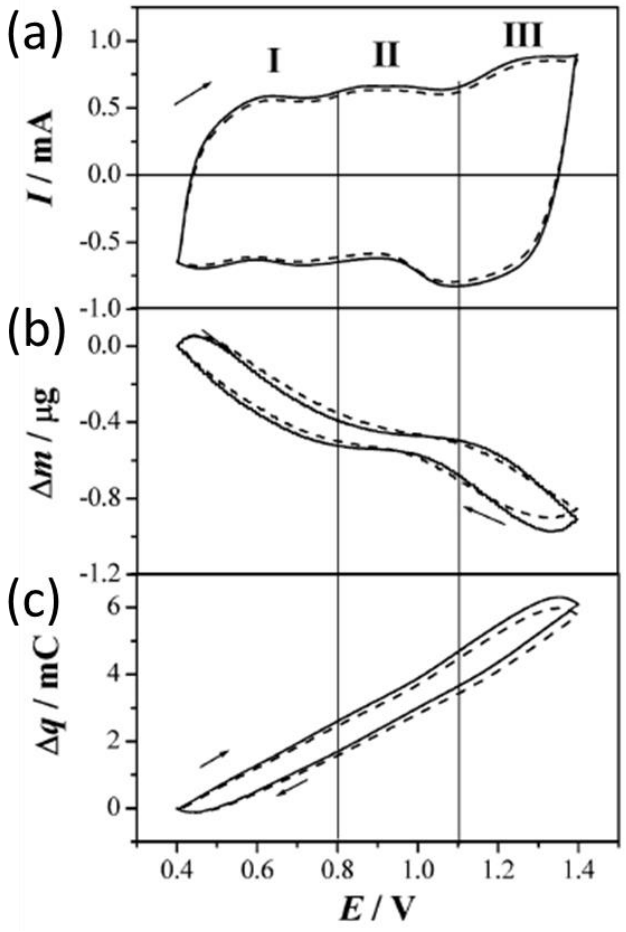

Figure 3.6 (a) CV, (b) mass evolution, (c) capacity vs. potential curves for RuO_2 in 0.1 M $HClO_4$ at 0.1 V/s.[75]

Assuming cations involved in the reaction are monovalent cations, the molar mass of the cation associated in the reaction are calculated to be 32, 1, and 17 in region I, II, and III, respectively. The molar mass indicates possible cations are $H_5O_2^+$, H^+, H_3O^+. The reactions from region I to III proposed are listed below:

$$RuO \cdot xH_2O \rightarrow RuO(OH) \cdot (x-y)H_2O + 2H_2O + H^+ + e^-$$

$$RuO(OH) \cdot (x-3)H_2O \rightarrow RuO_2 \cdot (x-y)H_2O + H^+ + e^-$$

$$RuO_2 \cdot (x-y)H_2O \rightarrow RuO_3 + zH_2O + 2H^+ + 2e^-$$

From this proposed mechanism, pure proton transfer is only involved when reaction takes place between Ru^{3+} and Ru^{4+}. Involvement of $H_5O_2^+$ and H_3O^+ may exist between Ru^{2+}/Ru^{3+} and Ru^{4+}/Ru^{6+}.

4 Characterization techniques

4.1 Powder X-ray Diffraction

Powder X-ray diffraction (PXRD) is a powerful technique to study crystal structures, therefore commonly employed to determine identities of crystalline materials which present atoms in periodic arrays with long range order. X-ray is magnetic radiation generated when high-energy electrons hit the target metal, causing electron transition between inner shell (K) and outer shell (L) of the target metal. The target metal determines the wavelength of characteristic radiation, and most common X-ray is produced from Cu Kα, where wavelength λ= 1.5406 Å. The reason of choosing X-ray to produce diffraction pattern is because the wavelength of X-ray (1 to 100 Å) is the same order of d spacing between crystallographic planes, which is one of the criteria to obtain clear diffraction patterns.

When beams of light are scattered by a periodic array, constructive and destructive interference may occur, depending on the phase difference between beams. Constructive interference takes place if beams are in phase, while destructive interference happens if beams are out of phase. Strong diffraction can be observed in presence of constructive interference. As shown in the following equation and **Figure 4.1**, Bragg's law describes the situation of strong diffraction when the wave path difference matches single or multiple folds of wavelength,

$$2dsin\theta = n\lambda$$

where *d* is the distance between lattice planes, θ is the Bragg angle, λ is the wavelength, and *n* is an integer ≥ 1.[76] Since different lattice planes have different *d* values, it is important to define a specific *d* for each plane. Miller indices (hkl), where h, k, and l are the reciprocals axial intercepts of the plane. Distance between lattice plane (hkl) can be written as d_{hkl}, which could be calculated with a certain θ value, corresponding to a specific peak in the diffraction pattern.

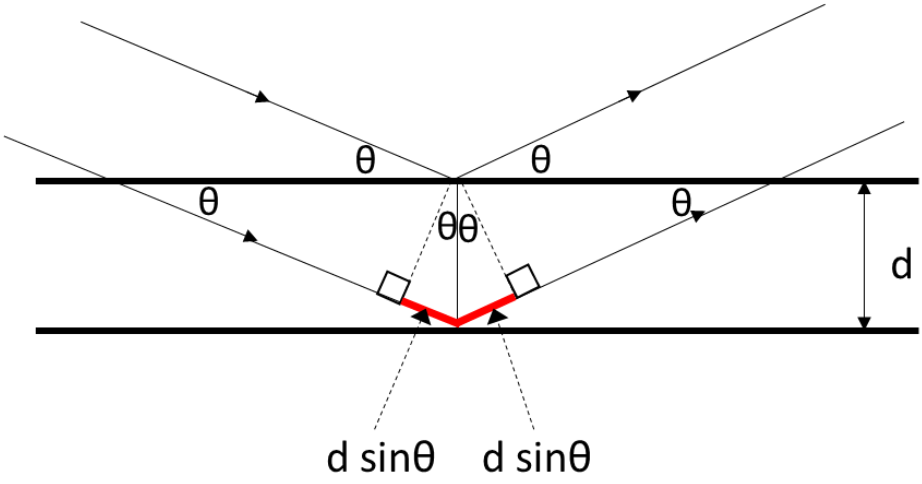

Figure 4.1 Schematic illustration of wave scattering.

From the PXRD pattern, domain size, also referred to as crystallite size, can be calculated from Scherrer equation, as described in equation below:

$$D_{hkl} = K\lambda/(B_{hkl}cos\theta)$$

where D_{hkl} is the crystallite size normal to (hkl), K is the crystallite-shape factor, estimated to be 0.9, λ is the wavelength of X-ray, B_{hkl} is the full-width at half-maximum in radians, and θ is the Bragg angle.[77]

4.2 Gas Adsorption

Gas adsorption is a commonly used technique to characterize the surface area and pore size distribution of porous materials. Based on simplified model of multi-layer adsorption, Brunauer-Emmett-Teller (BET) method has been used as a standard characterization of surface area. To generate isotherms and calculate surface area, nitrogen adsorption/desorption takes place in the porous sample at 77 K in presence of liquid nitrogen. Depending on the pore size, pores have been categorized into micropores, whose pore size is less than 2 nm, mesopores, whose pore size is between 2 nm to 50 nm, and macropores, whose pore size is larger than 50 nm. Generally, surface area derived from BET is considered to be effective unless it is ultramicroporous material.[78] Barrett-Joyner-Halenda (BJH) method, also based on adsorption/desorption isotherms, can calculate the pore size distribution. Note that BJH calculation is valid for materials with mesopores and small macropores, but not micropores.

Based on the shape of isotherms, IUPAC classified six different types of porous

adsorbents as described in **Figure 4.2**. Type I isotherm usually indicates adsorption on microporous adsorbents; type II and III indicate majority presence of macropores, with strong and weak adsorbate-adsorbent interaction, respectively[79]; type IV and V can be attribute to mesoporous adsorbents[80], with strong weak adsorbate-adsorbent interaction, respectively; type VI isotherm appears stepwise when there is a high degree of surface uniformity.

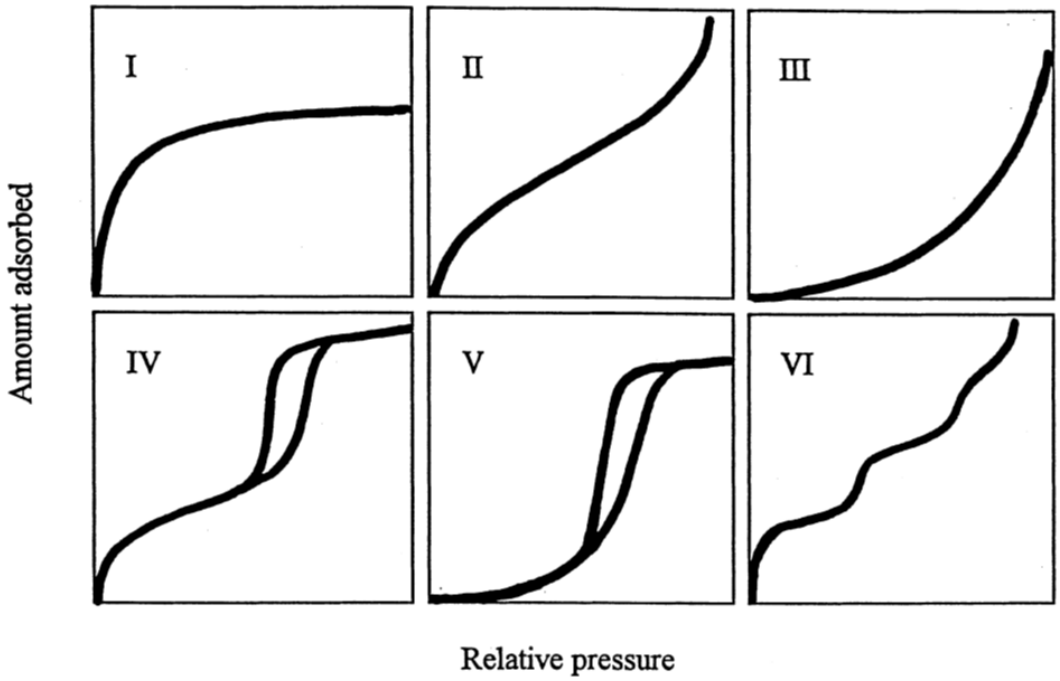

Figure 4.2 The IUPAC Classification of Adsorption Isotherms for Gas]Solid Equilibria.[79]

4.3 Infrared Spectroscopy

Unlike XRD where the wave frequency stays same before and after scattering, Infrared (IR) spectroscopy identifies chemical bonds or functional groups by measuring the

frequency (energy) of light absorption. **Figure 4.3** shows the principle of IR spectroscopy. When IR light with continuous wavelengths passes through the sample, light with certain wavelength matching energy difference between the vibrational ground and excited states is absorbed, and thus cannot be observed in the emission light.[81] One important criteria to see IR response from the molecular vibration is that the vibration causes molecular dipole changes. In the case homonuclear diatomic molecules, e.g. N_2, O_2, etc., their dipole moment remains zero in any vibration mode, so that they are IR-inactive molecules.[82]

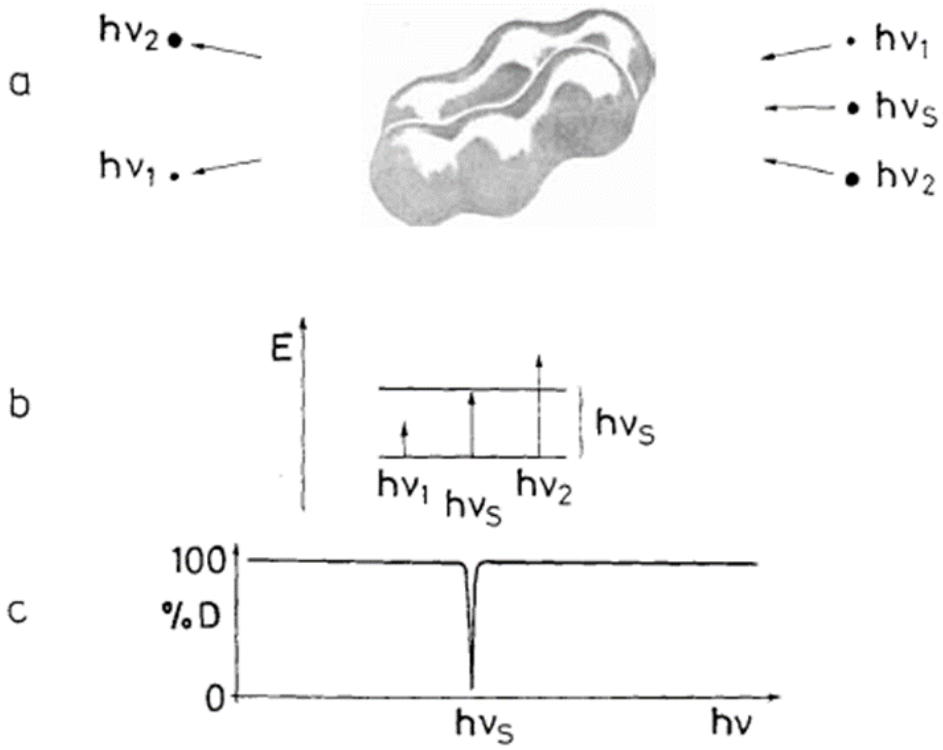

Figure 4.3 Principle of IR absorption.[81]

The IR vibrational modes can be classified into stretching vibration and bending vibration, which occur along with bond length change and bond angle change, respectively. Stretching mode, usually requiring high energy and activated at high wavenumber, includes symmetrical stretching and asymmetrical stretching. Bending mode, on the other hand requiring less energy and activated at low wavenumber, includes in-plane bending (scissoring and rocking) and out-of-plane bending (wagging and twisting) motions.[82]

4.4 Raman Spectroscopy

Raman spectroscopy, as a complementary technique to IR spectroscopy, collects molecular vibration based on light scattering. Different from light with continuous wavelength utilized in IR, a beam of light at a fixed wavelength irradiates the sample in continuous-wave or spontaneous Raman spectroscopy.

As shown in **Figure 4.4**, when light with frequency of ν_0 passes through the sample, a portion of the energy help the molecule change from ground state to excited state, giving output light with frequency of (ν_0-ν_s) which is named as Stokes shift in the Raman spectra; output light with frequency of (ν_0+ν_s) called anti-Stokes shift, is caused by the small portion of molecules at excited state before irradiated.[81] Both Stokes shift and anti-Stokes shift belong to inelastic scattering, because of the energy change after scattering. Intensity of Stokes lines is significantly higher than the anti-Stokes lines, because the majority of molecules are at ground state without irradiation. Rayleigh

scattering, without frequency change, provides no information about the molecular structure in the Raman spectra, which is usually filtered out in the final spectra. Different from IR, which is more sensitive to polar molecules, Raman spectroscopy is sensitive to non-polar molecules, because it is the electric polarizability change that determines the Raman peak intensity. Therefore, some IR-inactive materials could be characterized by Raman, e.g. graphite.

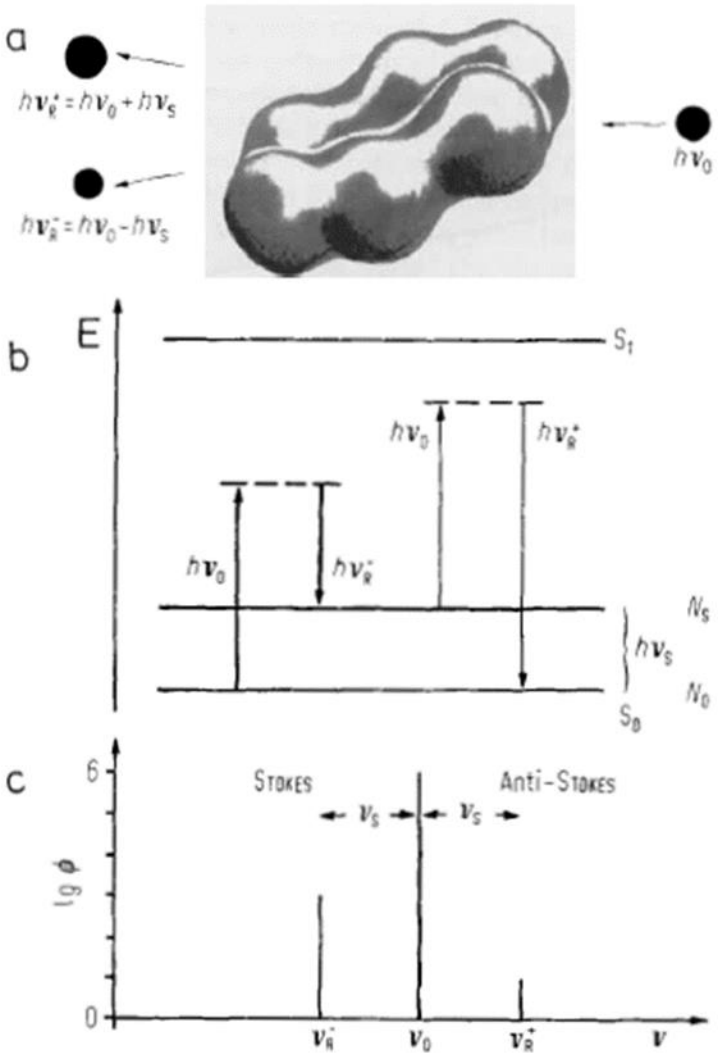

Figure 4.4 Principle of Raman scattering.[81]

4.5 X-ray Photoelectron Spectroscopy

X-ray photoelectron spectroscopy (XPS) is a powerful and popular surface analysis technique. By measuring the kinetic energy and the number of emitted electrons, elemental compositions can be identified at the surface of materials. **Figure 4.5** describes the principle of XPS. If an atom is irradiated by X-ray, whose energy is higher than the binding energy of core electrons around the atom, core electrons may be excited and escape from the nucleus with certain kinetic energy. Since each element has characteristic binding energies of core electrons, element can be identified by capturing the emitted electrons and measuring their kinetic energy.

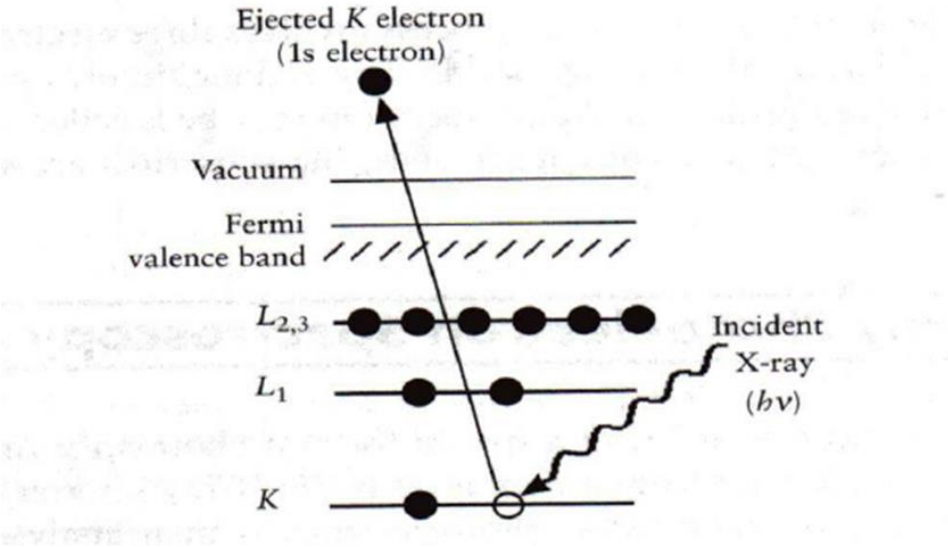

Figure 4.5 Schematic illustration of XPS process.[83]

The following equation describes the calculation of binding energy, where E_B is

electron binding energy in eV, E_K is kinetic energy of emitted electrons in eV, v is the frequency of X-ray in Hz, h is Planck's constant in eV·s, and φ is work function of the instrument in eV.[83]

$$E_B = h\nu - \varphi - E_K$$

Note that XPS is a surface analysis technique, which probes elemental composition of the sample within 10 nm from the surface. Special treatment is needed to characterize deeper layers of the sample, such as ion beam etching. Hydrogen and helium cannot be detected by XPS because the ionization cross sections are extremely low (H is 5000 times lower than C_{1s}), as well as non-existence of core electrons in H and He.[84, 85]

4.6 Electrochemical Measurement

Cell Configuration

All three-electrode cell tests are conducted in a T-shape Swagelok cell, as shown in **Figure 4.6** (a), where high-mass AC electrode serves as the counter electrode, saturated Ag/AgCl is selected as the reference electrode, and Ti rod is used as the current collector. Separator is either composed of glassy fiber or cellulose filter paper. Three-electrode cell tests can monitor and control potentials of both working electrode and counter electrode with respect to the reference electrode. **Figure 4.6** (b) shows the two-electrode cell configuration in a coin cell, which provides better sealing and used for most long-cycling tests.

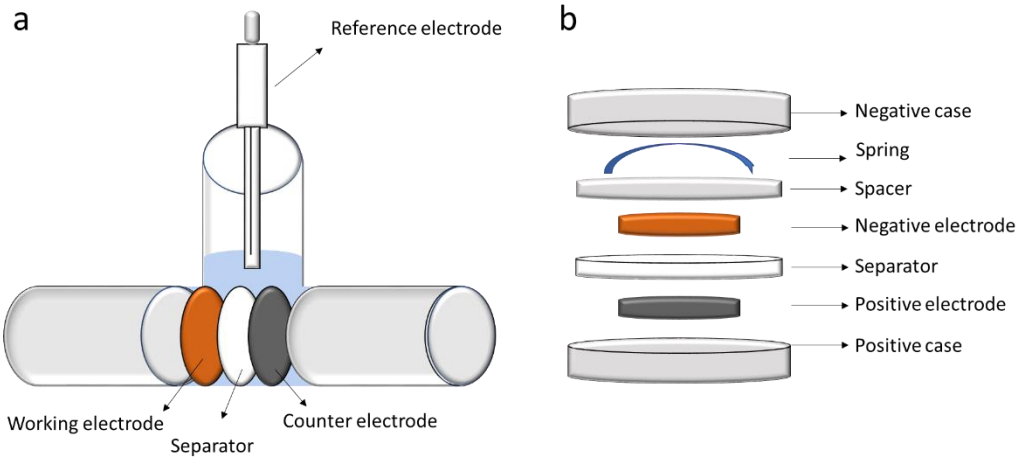

Figure 4.6 (a) Three-electrode cell configuration in a T-shape Swagelok cell, (b) two-electrode cell configuration in a coin cell.

Cyclic voltammetry

Cyclic voltammetry (CV) is a potential sweep method widely used to see current

response at various potentials. Briefly, potential changing at constant rate (dV/dt) is applied to the electrode, and at certain cutoff potential, sweep is reversed. Current peaks are observed if there are redox reactions taking place. Current increases because there is charge transfer at the electrode, indicating redox reactions taking place. However, at certain potentials, current start to decrease, because the current is limited by mass transfer rate due to the lack of reactant species at the electrode surface. When mass transfer is fast enough, e.g. using rotating disk electrode (RDE), such redox peaks would not be observed. Mass transfer includes diffusion, migration, and convection. Diffusion, depending on concentration gradients, is considered as the most predominant mass transfer in most systems. The diffusion limited current is proportional to square root of scan rate ($i_{diffusion} \propto \nu^{0.5}$). This can be used to distinguish contribution from diffusion limited process from capacitive storage. CV curves of an ideal EDLC are typically in rectangular shape, where current is proportional to capacitance and scan rate. Normally people test CV to see redox activity of electrodes or electrolytes, and identify the proper operating voltage window.

Galvanostatic charge/discharge

Galvanostatic charge/discharge (GCD) is an important chronopotentiometric technique, widely used to measure capacity, capacitance, energy, power, efficiency, cycling stability, etc. GCD applies constant current (positive or negative) to the working electrode, and then reverse the current direction at certain cutoff potentials, while monitoring the potential response. Since current is accurately controlled, amount of

charge could be measured quantitively. Diffusion controlled redox process usually shows plateaus at the same potentials where current peaks locate in CV curves. On the contrary, ideal EDLCs show perfect linear profiles in GCD measurement.

Capacity (mAh) is an important parameter describing the amount of charges stored/delivered, especially for battery electrode materials. It can be calculated by multiplying current and charge/discharge time. Capacitance (F) is to evaluate the charge storage capability of capacitive materials, whose GCD profiles are linear, meaning charge is stored independent of electrochemical potential. Capacitance describing materials with GCD non-linear profiles is inappropriate, because more charges are stored at certain potential ranges, whose charge storage capability is not representative at other potential ranges. Capacitance of such materials is uncertain when enlarging, lowering, or selecting different operating potential ranges. Specific capacitance can be calculated by the equation:

$$C = \frac{2It}{mV}$$

where C is specific capacitance of the working electrode (F/g), I is the constant discharge current (mA), t is the discharge time (s), m is the active mass of the working electrode (mg), V is the potential change of working electrode during discharge (V). "2" is in the numerator, because an EDLC is equivalent to two capacitors in series, so that capacitance of a single electrode is twice of the device.

Energy, determined by both capacity and voltage, can be calculated by integrating discharge profiles with the following equation:

$$E = \frac{1000 \times I}{3600 \times m} \int V(t)dt$$

where E is specific energy (Wh/kg), I is the constant discharge current (mA), m is the mass of electrodes or electrodes plus electrolytes (mg), V is the discharge voltage range (V), and t is discharge time (s).

To calculate the energy density of EDLCs, besides the equation above, the following equation is also widely accepted due to its simplicity.

$$E = \frac{1}{2} CV^2$$

In the above equation, E is specific energy of the device (Wh/kg), C is specific capacitance of the capacitor (F/g), and V is discharge voltage range (V). Be aware that this equation is derived by assuming the discharge profile is perfect linear. Therefore, it is only viable for EDLCs, and some pseudocapacitors. Although some literatures reported energy density of faradiac capacitors with non-linear GCD profiles, most of them overestimated the true energy.

Power describes how fast the cell can discharge, in other words, amount of energy delivered in unit time. Power density can be calculated by the equation below.

$$P = \frac{3600 \times E}{t}$$

P is power density (W/kg); *E* is energy density (Wh/kg); *t* is discharge time (s).

Coulombic efficiency (CE) is very important in practical batteries. Higher CE usually indicates higher reversibility, less side reactions, and most likely longer lifetime. CE is described by the ratio between amount of charge output and charge input. It can be calculated with the equation:

$$CE = \frac{Q_{discharge}}{Q_{charge}} \times 100\%$$

$Q_{discharge}$ and Q_{charge} are discharge capacity (mAh) and charge capacity (mAh), respectively.

Electrochemical Impedance Spectroscopy

Electrochemical impedance spectroscopy (EIS) is a technique to monitor the impedance change of a cell by applying alternating voltage at various frequencies. EIS

can tell how fast EDLCs can react, the kinetics of a charge-transfer process of a redox reaction, diffusion process, etc.

To interpret EIS results, people use equivalent circuits with different electric components to simulate cells, where resistors (R) and capacitors (C) are two most important circuit elements. When an alternating voltage is applied, an alternating current at the same frequency is obtained in presence of possible phase difference. The phase difference (ϕ) is named as phase angle. With a pure resistor, phase angle is zero; with a pure capacitor, phase angle is $\pi/2$. The overall impedance is given as the following equation:

$$Z(\omega) = Z_{Re} - jZ_{Im}$$

where Z is impedance dependent on angular frequency ω, Z_{Re} and Z_{Im} are real and imaginary parts, respectively, and $j=\sqrt{-1}$.

Nyquist plot is a common way to interpret EIS, where Z_{Im} is plotted vs. Z_{Re}. In simple circuits, with R and C in series, a vertical line parallel to y axis appears in Nyquist plot; if R and C are in parallel, a semi-circle is observed. A more complicated circuit is called Randles equivalent circuit, as shown in **Figure 4.7** (a).

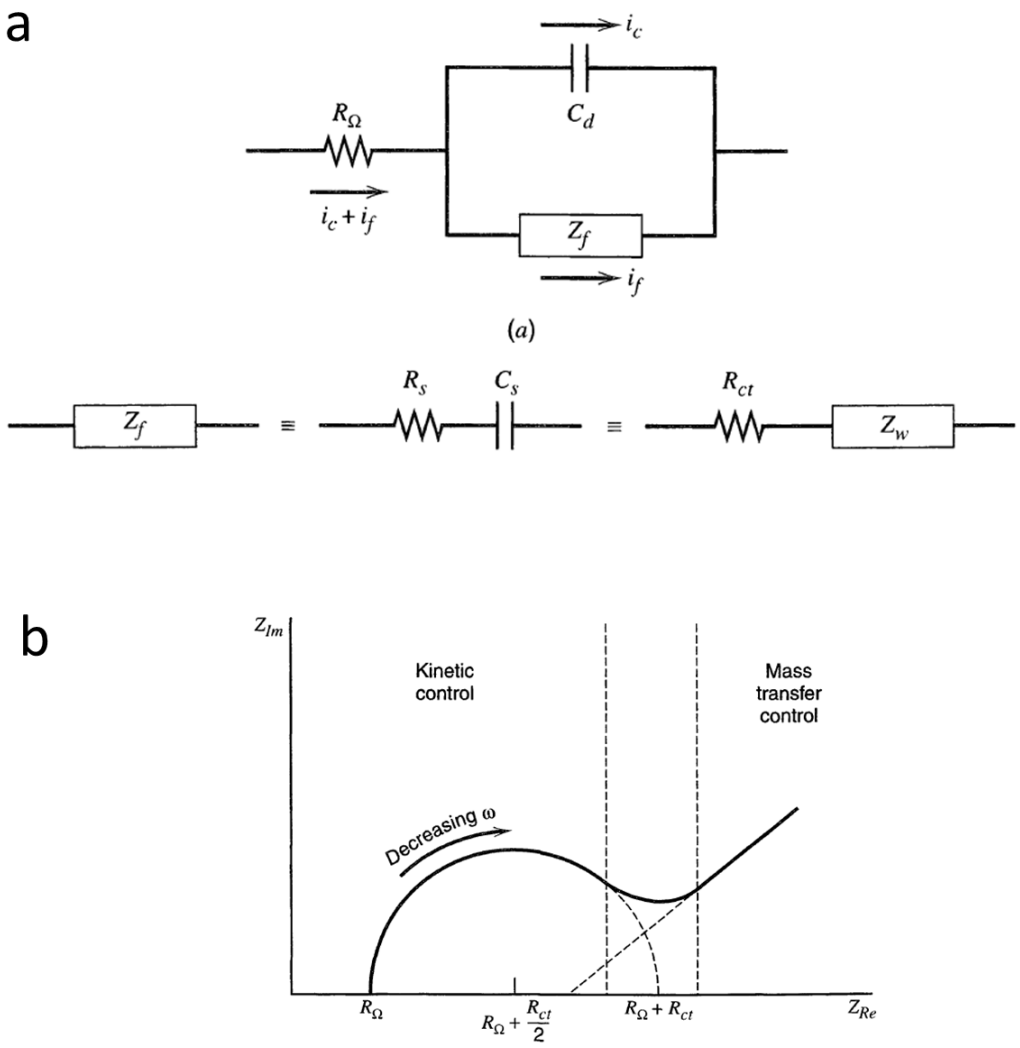

Figure 4.7 (a) Randles circuit and (b) the corresponding Nyquist plot.[86]

R_Ω stands for the solution resistance, C_d is electrical double layer capacitance, and Z_f is faradaic impedance. Z_f is typically described as charge-transfer resistance R_{ct} in series with Warburg impedance Z_w, which is caused by mass transfer. **Figure 4.7** (b) shows the Nyquist plot corresponding to Randles circuit, where the X intercept represents the solution resistance, the diameter of the semicircle refers to charge-

transfer resistance, and the linear line with about $\pi/4$ angle with X axis is due to mass transfer.

5 New Redox Pair in Aqueous Electrolyte for EC Applications

5.1 Abstract

We report a new electrochemical capacitor with an aqueous KI-KOH electrolyte that exhibits a higher specific energy and power than the state-of-the-art nonaqueous electrochemical capacitors. In addition to electrical double layer capacitance, redox reactions in this device contribute to charge storage at both positive and negative electrodes via a catholyte of IO_x^-/I^- couple and a redox couple of H_2O/H_{ad} on the negative electrode, respectively. Here, we, for the first time, report utilizing IO_x^-/I^- redox couple for the positive electrode, which pins the positive electrode potential to be 0.4-0.5 V vs. Ag/AgCl. With the positive electrode potential pinned, we can polarize the cell to 1.6 V without breaking down the aqueous electrolyte so that the negative electrode potential could reach -1.1 V vs. Ag/AgCl in the basic electrolyte – greatly enhancing energy storage. Both mass spectrometry and Raman spectrometry confirm the formation of IO_3^- ions (+5) from I^- (-1) after charging. Based on the total mass of electrodes and electrolyte in a practically relevant cell configuration, the device exhibits a maximum specific energy of 7.1 Wh/kg, operates between -20 to 50 °C, provides a maximum specific power of 6222 W/kg, and has a stable cycling life with 93% retention of the peak specific energy after 14,000 cycles.

5.2 Introduction

Electrochemical capacitors (ECs) have a broad range of applications.[87-89] ECs store energy by two mechanisms: electrical double layer (EDL) capacitance and pseudocapacitance.[90] EDL capacitors (EDLCs) employ electrodes comprising activated carbons (ACs) with high specific surface areas. The capacitance derives from electrostatic interaction between the polarized electrode surface and the attracted solvated ions, thus forming EDLs on each electrode. EDLCs exhibit excellent cycling life and high specific power but limited energy density.[91, 92] To date, much effort has been devoted to the syntheses of nanoporous carbons with tunable properties[93], to understanding the interaction between solvated ions and the electrode surface, and to elucidating the mechanisms of EDL formation.[4, 6, 91, 94-101] Pseudocapacitors, on the other hand, are essentially high-rate batteries employing redox active electrodes that can operate on either of the two mechanisms: (1) surface/near-surface redox reactions and (2) intercalation redox reactions.[102] Great progress has been made in developing pseudocapacitors based on conductive polymers_ENREF_19[103-106] and various transition metal oxides,[107-113]_ENREF_23_ENREF_23 but such chemistries do suffer compromised power and cycle life compared to EDLCs.

_ENREF_17_ENREF_20Recently, integrating solvated redox-active species into electrolytes has emerged as a new strategy to increase the energy density of EDLCs.[114-117] The principle behind this strategy is that the redox species remain solvated during cycling, providing faster diffusion and kinetics than solid-state materials. As Lota *et al.* reported, KI-solvated aqueous electrolyte with I_3^-/I^- redox couple displays an

enhanced capacitance due to the electrochemical behavior of carbon/iodide interface.[57, 58] It was also published that ECs with KI as an additive to an electrolyte of sulfuric acid exhibit enhanced specific energy.[118] In an alkaline polyvinyl alcohol gel electrolyte, KI was also added to increase the ionic conductivity and pseudocapacitance.[119]

Along this line, _ENREF_26we reported a hybrid electrochemical battery-supercapacitor system utilizing an electrolyte containing anionic catholyte and cationic anolyte derived from the mixture of solvated KI and $VOSO_4$, which showed improved energy density and good cyclability.[61] Very recently, a combined electrolyte with two physically separated compartments: pH-neutral KI for the positive electrode side and KOH for the negative electrode side was reported.[120] In this cell, the maximum cell voltage reaches 1.5 V, compared to 1.0 V typically reported by other aqueous-based ECs. The voltage of 1.5 V for the cell is achieved by polarizing the negative electrode to -1.4 V vs. standard hydrogen electrode (SHE) and the positive electrode to 0.1 V vs. SHE. In this cell, the positive electrode operates on the I_3^-/I^- redox couple, which pins the positive electrode at 0.1 V vs. SHE. It appears that the hydrogen evolution reaction is suppressed even down to -1.4 V vs. SHE, which allows, in this paper, an investigation on hydrogen adsorption/desorption redox reactions on the surface of porous carbon.

Herein, for the first time, we report the electrochemical properties of an aqueous electrolyte of mixed KI and KOH. The motivation of mixing KI and KOH is to explore

the possibility of using the redox couple of IO_x^-/I^-, where the IO_x^- can be either IO_3^- or IO_4^-, which is confirmed by mass spectrometry and Raman spectrometry. This is because, according to the Pourbaix diagram of iodine, when the cell is polarized, the I^- ions in a basic electrolyte will be oxidized into IO_x^-, *i.e.*, IO_3^- and/or IO_4^-, instead of I_3^-, pinning the potential on the positive electrode side. Therefore, the full cell voltage can be high as long as the hydrogen evolution reaction is effectively suppressed by the basic electrolyte on the negative electrode as well as a high over-potential. With this KI/KOH electrolyte, here the reported aqueous cell approaches a voltage of 1.6 V.

5.3 Experimental

Preparation of carbon electrodes

Carbon fibers (Donacarbo S-241 from Osaka gas Co., Ltd) were activated to obtain a high specific surface area under CO_2 with a gas flow rate of 229 cc/min at 920 °C for 18 h. Such conditions are optimized to obtain a surface area above 2400 m^2/g. In forming an electrode, the obtained activated carbon was mixed in amyl acetate with polytetrafluoroethylene (PTFE) and carbon black (Super P) by a weight ratio of 8/1/1. After drying in air, the mixture was processed into a self-standing film by a rolling machine, which was later dried inside a vacuum oven at 80 °C overnight. The active mass for the final electrodes is ~ 5.1 mg/cm^2, where the electrode is of a thickness of ~ 90 μm.

Porosity Measurements of porous carbon

Specific surface area was measured by a Micrometrics TriStar II 3020 analyzer. Samples were degassed under N_2 at 250 °C for 4 h before the measurements. BET surface area and pore size distribution were obtained and calculated from N_2 sorption isotherms at -196 °C.

Electrochemical characterization

Three-electrode cells were assembled in custom-made T-Swagelok cells, consisting of two identical carbon electrodes and a saturated Ag/AgCl electrode as the reference electrode (RE). The three-electrode cell in this work is slightly different from the conventional configuration of three-electrode cells where there typically is a working electrode, a counter electrode, *i.e.*, a platinum wire, and a reference electrode. In our system, two identical carbon electrodes serve as both working and counter electrodes. Coin cells were made in a symmetric configuration, using a polycarbonate membrane as the separator with a thickness of 9 μm and porosity of 17.7% (Sterlitech Corporation). Each coin cell contains only 10 μL of electrolyte to test the performance with limited electrolyte, which is sufficient to fill up the porosity of both electrodes and the separator. By calculation, the void volume inside both electrodes and separator is only ~ 8.40 μL (see Supporting Information for detailed calculation). The galvanostatic charge-discharge tests were conducted on a Maccor Series 4000. The cyclic voltammetry (CV) measurements were carried out on an EC-lab VMP3 instrument.

Non-aqueous Maxwell capacitors (BCAP0001-1F and BCAP0010-10F) were tested at different current densities for comparison. We count only the mass of electrodes and electrolyte for commercial cells for comparison purposes.

Calculation of the Usage of Limited Electrolyte in Coin Cells:

We first estimated the total volume of two film electrodes to be 14 μL based on the electrode area of 0.785 cm^2 each, and the average thickness of the film electrode of ~90 μm. We then calculated the solid volume occupied by carbon and binder in the electrode films. The volume occupied by solid carbon in both electrodes is estimated to be 5.6 μL, based on the density of 1.6 g/cc of the carbon before activation, measured by Archimedes' method. We assume that carbon black additive shares the same density as the amorphous carbon precursor. The volume of PTFE binder is calculated to be 0.45 μL based on its density of 2.2 g/cc. Therefore, the pore volume inside the electrodes equals to 7.95 μL (=14 μL - 5.6 μL - 0.45 μL).

We calculated the pore volume contributed from the separator based on its volume and porosity. The polycarbonate separator has a thickness of 9 μm and porosity of 17.7%. The total pore volume inside one separator (diameter: 1.9 cm) is calculated to be 0.454 μL. So, the total pore volume from both electrodes and separator is 8.40 μL (7.95 μL + 0.454 μL). Therefore, 10 μL of electrolyte is expected to be sufficient to fill up the porosity of a non-flooded coin cell.

Mass spectrometry (MS)

The cell was cycled for 3000 cycles at a voltage of 1.5 V before it was taken apart to collect the charged electrolyte. Electrolyte was diluted by 1000 times before tests. A Waters Synapt G1 HDMS mass spectrometer equipped with a Z-spray electrospray ionization source was used to acquire the MS data in the negative-ion mode. The voltages of capillary, sampling cone, and extraction cone are 1300 V, 40 V, and 4.0 V respectively. The source and desolvation temperatures are 80 °C and 450 °C.

Raman spectrometry

Raman spectra were measured in DXR SmartRaman with 780 nm laser as the excitation source. Through the 50 μm slit, data were collected in 8 exposures with 8 seconds each time.

5.4 Results and Discussion

After CO_2 activation of carbon fibers, a high surface area of 2405 m^2/g and a total pore volume of 1.0 cc/g were obtained (**Figure 5.1**). According to **Figure 4.2**, the isotherm can be classified to type I, a typical isotherm from microporous material. Specific BET surface area and pore size distribution were measured by nitrogen sorption at -196 °C. A surface area of 2405 m^2/g and pore volume of 1.0 cc/g were obtained, most of which is from pores with size less than 4 nm, exhibiting high EDL capacitance and providing surface for redox reactions.

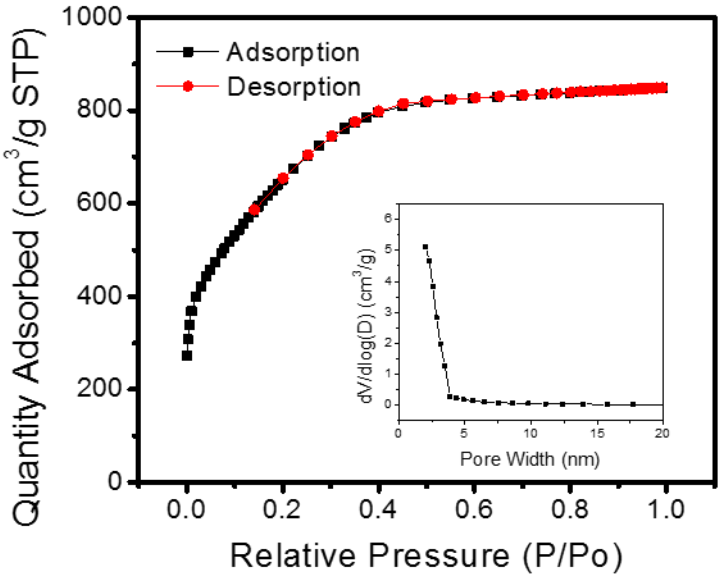

Figure 5.1 N_2 isotherms of activated carbon at -196 °C, inset: Barrett-Joyner-Halenda (BJH) pore size distribution calculated from the adsorption curve.

With the nanoporous activated carbon as the electrodes in a two-electrode cell, we compared the electrochemical performance of pure KI and KI with addition of KOH in various concentrations. The specific capacitance is based on a full cell. Apparently, at each concentration, adding KOH helps increase capacitance. From **Figure 5.2**, the cell capacitance increases with a higher concentration of KI. With the presence of KOH, similar capacitance was found when using 4 M KI and 5 M KI. Considering the cost and electrolyte density, the optimal electrolyte is determined to be 4 M KI with 1 M KOH.

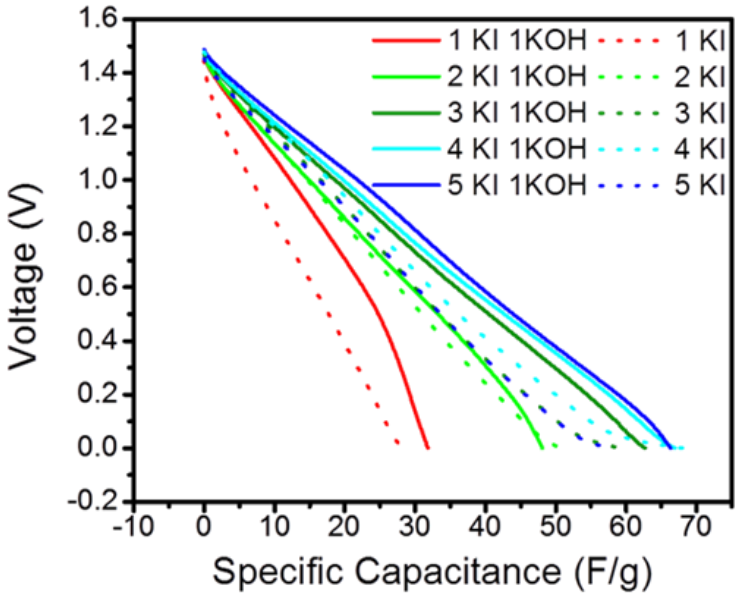

Figure 5.2 Galvanostatic discharge potential profiles for cells containing pure KI electrolytes with concentrations from 1 to 5 M (dashed lines) and the mixed electrolytes of KOH (1 M) plus KI with different concentrations from 1 M to 5 M (solid lines).

Galvanostatic charge-discharge cycles were collected in a three-electrode cell at a current density of 1 A/g, which is normalized to carbon mass in one electrode. **Figure 5.3** (A) shows the potential profiles when the three-electrode cell is charged to 1.5 V. At the 200th cycle, full cell potential profiles exhibit sectioned sloping regions, while a well-defined plateau at 0.4 V vs. Ag/AgCl is observed at the positive electrode, which is from the redox reactions involving iodide. This is consistent with the Pourbaix diagram, which shows the predominant oxidized species in basic aqueous media as iodates, IO_3^-. On the negative electrode, the potential profiles are slightly curved lines, indicating some faradaic reactions in parallel with the capacitive charging on the activated carbon.

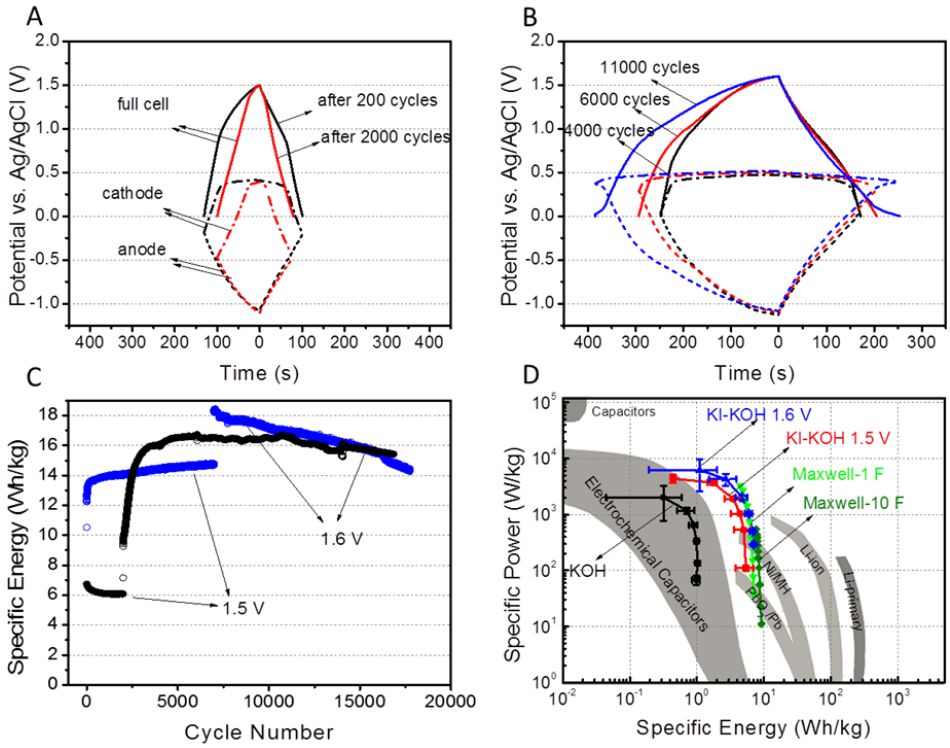

Figure 5.3 (A) Three electrode galvanostatic charge-discharge at 1 A/g when charging to 1.5 V, (B) when charging to 1.6 V, (C) long term cycling at 5 A/g (black in Swagelok cell, blue in coin cell, specific energy calculated based on the mass of both electrodes), (D) Ragone plot calculated based on the total mass of both electrodes and electrolyte.[121]

From the 200th cycle to the 2000th cycle, specific energy faded. At the 2000th cycle, we conducted the three-electrode charge-discharge test (red curves in **Figure 5.3** A). Interestingly, the potential plateau on the positive electrode was diminished compared to the profile at the 200th cycle. We also observed that the potential of short circuit (PSC) of carbon electrodes was significantly lowered from -0.2 V to -0.5 V vs. Ag/AgCl reference electrode after 1800 cycles. The negative shift of PSC caused less capacitive contribution to total charge storage on the negative electrode, and more capacitive contribution on the positive electrode. Because the combination of faradaic and capacitive charge storage on the positive electrode must equal the capacitive charge

storage (this may include hydrogen adsorption) on the negative electrode, when the PSC shifts negatively, less charge-storage from the redox reactions is needed on the positive electrode at the same cell polarization of 1.5 V.

After the 2000th cycle, we increased the cell voltage from 1.5 to 1.6 V in order to better take advantage of the redox reactions on the positive electrode. As shown in **Figure 5.3** ©, the specific energy based on the mass of both electrodes increased from 6 to 16 Wh/kg (the electrolyte mass was not included due to the excess electrolyte in three-electrode cell). We collected three-electrode charge-discharge potential profiles at the 4000th, 6000th and 11000th cycles, as shown in **Figure 5.3** (B). The negative electrode polarization was observed to be -1.1 V vs. Ag/AgCl, consistently. The positive electrode polarization increased from 0.4 to 0.5 V, showing a large plateau, which resulted in a dramatic increase in specific energy. However, upon increasing the cell voltage from 1.5 to 1.6 V, the Coulombic efficiency decreases. In the 1999th cycle, the Coulombic efficiency is 96.8%, which decreases to 86.9% in the 2001st cycle. We attribute the lowered Coulombic efficiency to the irreversible reactions on the negative electrode side. As revealed in **Figure 5.3** (B), it is evident that the potential profiles are highly reversible on the positive electrode in the 4000th, 6000th and 11,000th cycles. However, on the negative electrode side, plateaus are observed near -1 V vs. Ag/AgCl during charging, whereas such plateaus are absent in the following discharge, resulting in the lowered Coulombic efficiency and energy efficiency. For the irreversible reaction on the negative electrode, we attribute it to a certain extent of hydrogen

evolution reaction (HER), where the evolved hydrogen gas may not be oxidized reversibly. From the 4000th cycle to 11000th cycle, the consistency of cell potential profiles is responsible for the stable cycling performance, as shown in **Figure 5.3** (C). From the 3000th cycle to 17,000th cycle, the fading in specific energy was only 7%, indicating excellent reversibility of the KI-KOH system. Coin cells were also tested, which is shown in blue in **Figure 5.3** (C). The specific energy faded from 18 to 14 Wh/kg from the 7000th to the 17000th cycle. Further cell optimization will likely enable these already impressive values to be improved.

The fact that PSC shifts to lower values during the initial cycling at cell polarization of 1.5 V but increases over further cycling at cell polarization of 1.6 V is very interesting. However, a comprehensive investigation of PZC and PSC of the electrodes by itself can be a large project, which is thus beyond the scope of this work. Here, we provide our thoughts on this issue supported by experimental evidence.

The lowered PSC during the initial cycling at a cell polarization of 1.5 V can be related to the hydrogen adsorption on the negative electrode. When some irreversibly adsorbed hydrogen atoms cover the negative electrode, its PZC decreases as documented by prior studies,[86, 122] which may lower the PSC for the cell. Interestingly enough, upon increasing the cell polarization to 1.6 V, the surface of carbon positive electrode was, indeed, oxidized to a certain extent, where, revealed by Energy Dispersive X-ray (EDX) spectroscopy, the mass ratio of oxygen over carbon of the positive electrode increases

from 2.8% to 5.7% after cycling for 2000 cycles (**Figure 5.4**). It is known that oxidized carbon surface causes an increased PZC of porous carbon electrode,[86, 122]_ENREF_41 which overcomes to the impact from the negative electrode and causes the PSC to increase over cycling at 1.6 V.

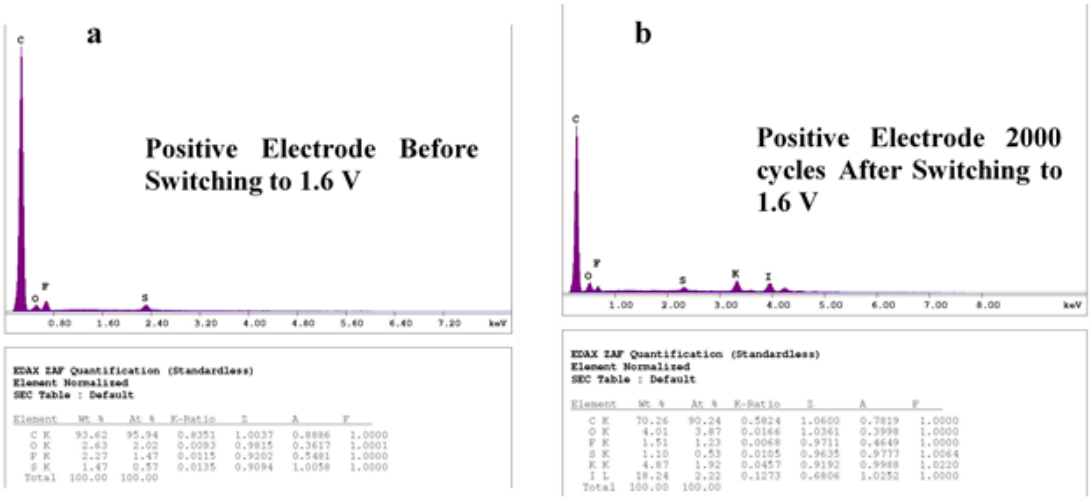

Figure 5.4 EDX results on the positive electrode (a) before switching from 1.5 to 1.6 V and (b) 2000 cycles after switching to 1.6 V.

Another issue is whether applying 1.6 V to the cells causes breaking down of the aqueous electrolyte. We recognize that the thermodynamic potential value of water oxidation is lower than the potential where the positive electrode is finally polarized at the end of charging process. However, such oxidation reaction is normally kinetically inhibited even if catalysts are employed. Oxidizing water, *i.e.*, *via* the oxygen evolution reaction (OER) is no easy task due to the large over-potential. Even with noble metal oxides as catalysts, *e.g.*, rutile-type RuO_2, the state-of-the-art catalyst for OER, the reaction still suffers an over-potential of 0.2 V.[123] As indirect evidence that OER is not severe, the cells with very limited volume of electrolyte, *i.e.*, 10 μL, can be run for well

more than 15,000 cycles. The electrolyte would be soon consumed if OER or hydrogen evolution reaction (HER) occurred to a significant extent, which is clearly not the case.

A Ragone plot is a straightforward way to show specific energy and power, which we calculated based on the combined mass of both carbon electrodes and electrolyte. Cells with an electrolyte of 4 M KI and 1 M KOH, polarized to either 1.5 V or 1.6 V were tested at 3, 5, 10, 20, 50, 100 A/g, respectively (**Figure 5.3** D). To compare our system with aqueous EDLCs, cells with an aqueous electrolyte of 6 M KOH polarized to 1 V were also tested. Cells with the KI/KOH electrolyte exhibit superior performance in both specific energy and power, compared to the KOH-based EDLC. At 3 A/g and charged to 1.6 V, the KI-KOH cell obtained 7.1 Wh/kg and 291 W/kg, while at 100 A/g, the cell exhibits 1.1 Wh/kg and an impressive power of 6221 W/kg, which is comparable with the state-of-the-art EDLCs based on non-aqueous electrolytes (2 types from Maxwell) (**Figure 5.3** D). Additionally, our system uses a cost-effective and safe aqueous electrolyte, which is encouraging for potential practical applications.

We next tried to understand the enhanced performance of the KI/KOH electrolyte. Referring to the iodine Pourbaix diagram (**Figure 5.5**), the possible species that exist at pH 14 are I^-, IO_3^-, and $H_2IO_6^{3-}$. When I^- is oxidized during charging, the final species could be either IO_3^- or $H_2IO_6^{3-}$, corresponding to 6 or 8 total electrons transferred.

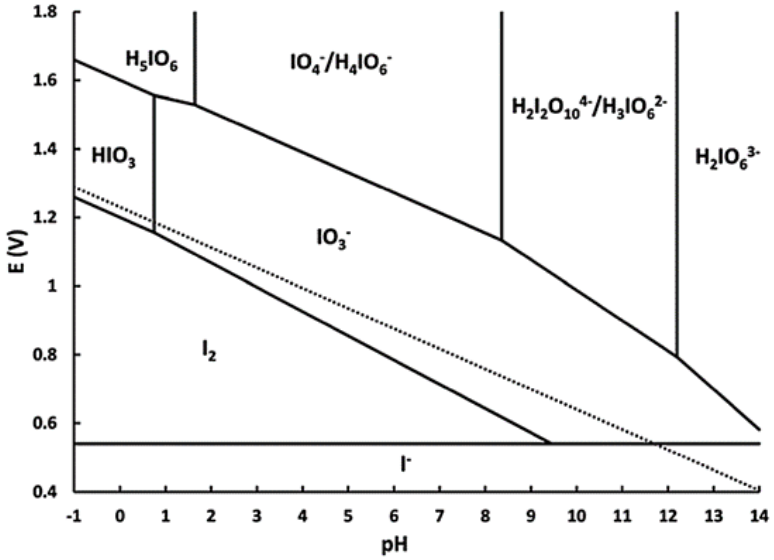

Figure 5.5 Pourbaix diagram of iodine species.[124]

The mechanism of IO_3^- formation from I_2 has been reported and discussed in literature.[125, 126]

$$\mathbf{I_2 + H_2O \rightarrow I^- + HOI + H^+} \qquad \mathbf{(1)}$$

$$\mathbf{3HOI \rightarrow IO_3^- + 2I^- + 3H^+} \qquad \mathbf{(2)}$$

In the KI/KOH electrolyte, I^- is oxidized to I_2 first that disproportionates, in a basic solution, to form hypoiodous acid (HOI). HOI further disproportionates to form iodate. The overall reaction is as follows:

$$\mathbf{I^- + 6OH^- \rightarrow IO_3^- + 3H_2O + 6e^-} \qquad \mathbf{(3)}$$

In order to identify the I-containing species in the electrolyte, we collected MS for the electrolyte (4 M KI and 1 M KOH) from a two-electrode coin cell after 3000 cycles as well as a standard sample of KIO_3 solution (**Figure 5.6**).

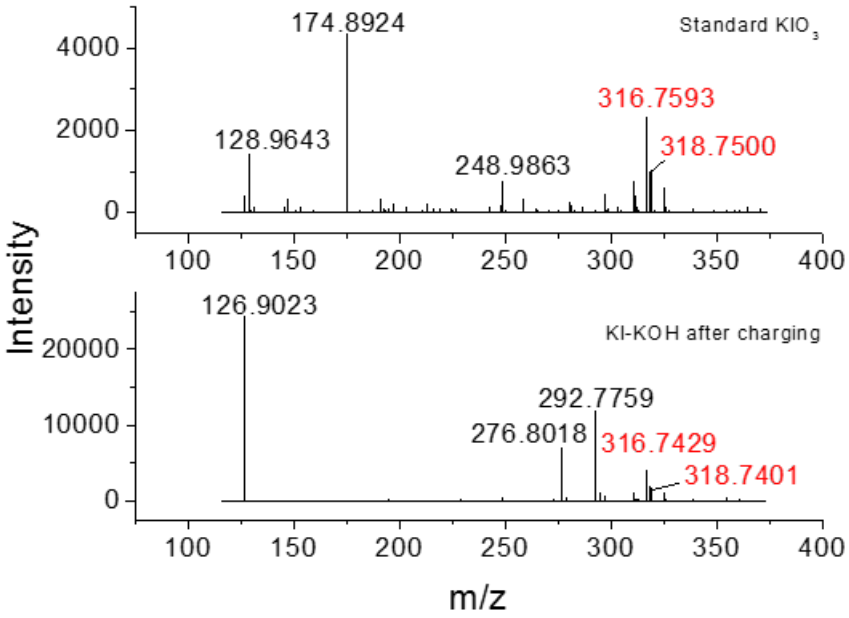

Figure 5.6 Mass spectra of standard KIO_3 and electrolyte of KI-KOH after cycling ending with charge.

For the charged KI+KOH electrolyte, the first three major peaks at 126.9023, 292.7759, and 276.8018 m/z are assigned to be I^- (126.9045 m/z), KI_2^- (292.9074 m/z), and NaI_2^- (276.7987 m/z), respectively. The other two major peaks at 316.7428 and 318.7401 m/z in the charged electrolyte match the peaks at 316.7593 and 318.7500 m/z in the standard KIO_3 solution, which are assigned to $IO_3^- \cdot 8H_2O$ (317.0087 m/z) and $IO_4^- \cdot 7H_2O$ (319.0246 m/z), respectively. This presents strong evidence for the formation of iodate and periodate over cycling of our device. This is a fundamental difference between our system and the device investigated by Frackowiak *et al.*[120]

In order to further confirm the formation of iodate, we conducted Raman spectrometry measurements for the KI+KOH electrolyte before and after charging by using pure KIO_3 and water as control samples (**Figure 5.7**). From the Raman results, the charged electrolyte of KI+KOH shows a much-enhanced signal at 800 cm^{-1} as the standard KIO_3 solution, which can be assigned to the non-polar stretching vibration of IO_3^- (symmetry A_1)[127]. Therefore, both MS and Raman results indicate that IO_3^- (+5) has been formed after charging.

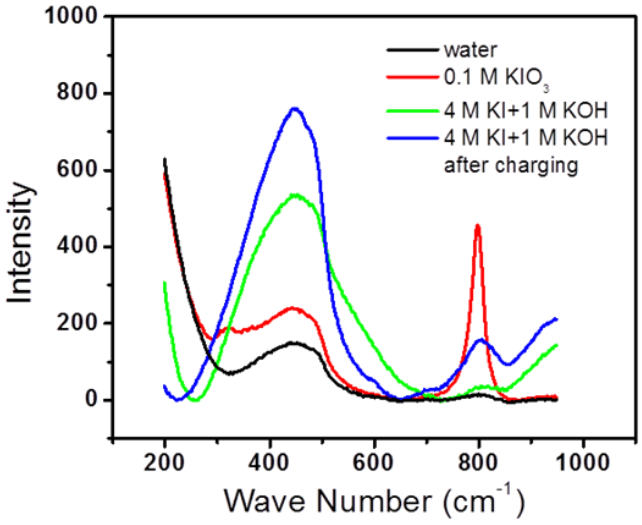

Figure 5.7 Raman spectra of water, 0.1 M KIO_3 and mixed electrolyte: 4 M KI and 1 M KOH before and after charging.

On the negative electrode, the curved charge-discharge potential profiles indicate simultaneous redox reactions and capacitive charging. Hydrogen adsorption/desorption could be responsible for this and the mechanism has been explained and discussed in the literature.[128, 129] In alkaline solution, water can be reduced through Volmer reaction (4) to form adsorbed hydrides:

$$H_2O + e^- \rightarrow H + OH^- \qquad (4)$$

$$C + H \rightarrow CH_{ad} \qquad (5)$$

However, due to Heyrovsky reaction (6) and/or Tafel reaction (7), adsorbed hydrides can be discharged to form H_2, which would result in irreversible capacity loss in our device:

$$CH_{ad} + H_2O + e^- \rightarrow H_2 + OH^- + C \qquad (6)$$

$$2H \rightarrow H_2 \qquad (7)$$

$$CH_{ad} + CH_{ad} \rightarrow H_2 + 2C \qquad (8)$$

For hydride formation to provide significant reversible capacity, the activation barrier for the Heyrovsky and Tafel equations (eqns. 6 and 7) must be larger than for the Volmer reaction (eqn. 4). These conditions are typical in basic media.[120]

Because the charge storage on both positive and negative electrode sides may rely on redox reactions, it is of fundamental interest to evaluate the charge storage mechanisms and compare the contribution from capacitive storage to that from diffusion controlled storage. Thus, CVs were tested in three-electrode cells for both positive and negative electrode at various scanning rates from 1 mV/s to 50 mV/s. From **Figure 5.8**, the PSC is about -0.37 V vs. Ag/AgCl, and the negative and positive electrode are polarized to

-1.06 V and 0.44 V, respectively, when the cell is charged to 1.5 V. From -0.7 V to 0.3 V, the rectangular shape of CVs indicates the ideal capacitive behavior of the capacitor, while the peaks at -1 V and 0.4 V correspond to redox reactions. We attribute the redox peak at -1 V to the hydrogen adsorption and desorption on the porous carbon, which provides a fraction of redox capacitance on the negative electrode, especially at low potential. On the positive electrode, the redox peak at 0.4 V correlates to the redox reaction of iodine-containing species. Inside each CV, the shaded area is the capacitive contribution, *i.e.*, current is proportional to scan rate v, which is described as $k_1 v$.[102, 130]

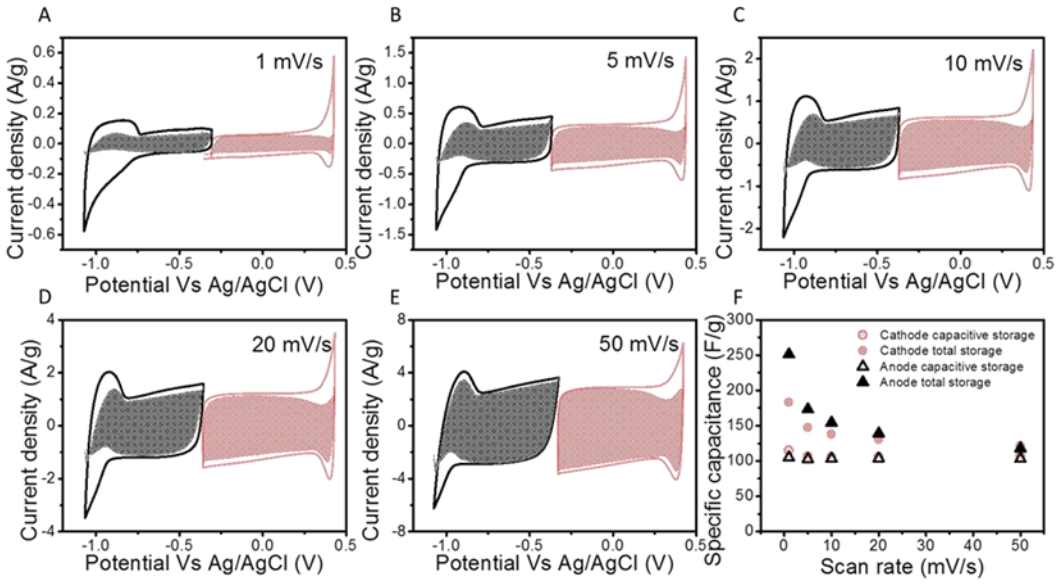

Figure 5.8 Cyclic voltammetry of three-electrode cell using 4 M KI and 1 M KOH at (A) 1 mV/s, (B) 5 mV/s, (C) 10 mV/s, (D) 20 mV/s, (E) 50 mV/s, (F) specific capacitance at different scanning rates, positive electrode in red, negative electrode in black.

The redox reactions are typically diffusion-controlled processes that are proportional to $v^{1/2}$, thus the corresponding current contribution is $k_2 v^{1/2}$. By testing CV at

different scanning rates, the coefficients k_1 and k_2 can be calculated for different potentials, and the total current can be deconvoluted into diffusion-controlled and capacitive contributions. As shown in **Figure 5.8**, the mid-potential region is dominated by capacitive current, and the gap between total current and capacitive current (shaded area) at low potential and high potential is from the diffusion-controlled redox processes, which decreases as the scanning rate increases. We note that kinetic limitations driving the redox reactions likely play a major role in the decrease of current at faster scan rates. In **Figure 5.8** (F), when the scan rate is increased to 50 mV/s, the total capacitance from negative electrode and positive electrode drops from 251 F/g (1 mV/s) to 118 F/g, and from 183 F/g (1 mV/s) to 122 F/g, respectively. However, little difference is observed in the capacitance from the double layer charging process when increasing scanning rates.

To further investigate hydrogen adsorption/desorption, GCD profiles at the negative electrode are compared between KI and KI/KOH. In **Figure 5.9** (A), negative electrode specific capacity (normalized to single electrode mass) is plotted versus negative electrode potential. At higher cell voltage (from 0.8 V to 1.5 V), the negative electrode is polarized to more negative values (from -0.5 V to -1.1 V). In the presence of KOH, the slope of the discharge profile is steeper, indicating a stronger capability to store charge. In **Figure 5.9** (B), higher capacitance is observed using KI/KOH electrolyte, which is attributed to the enhanced hydrogen adsorption/desorption in porous carbon.

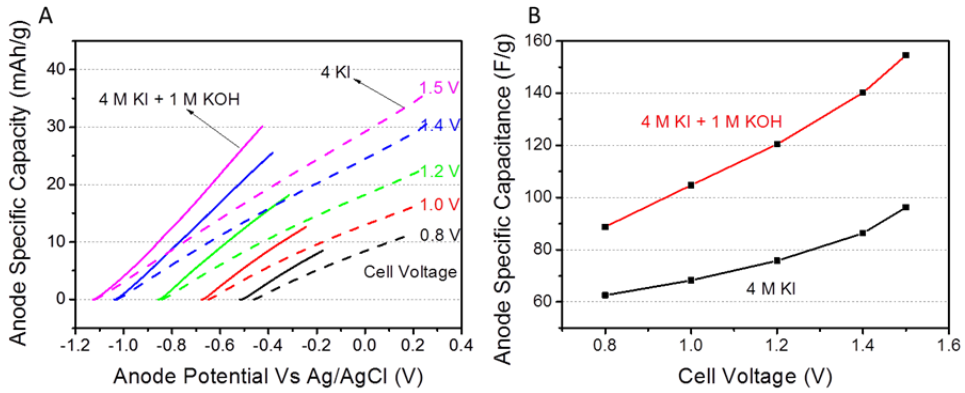

Figure 5.9 (A) Discharge capacity and (B) capacitance on the negative electrode: A comparison between with and without the presence of KOH.

Self-discharge is another important factor affecting the capacitor applications. To study the self-discharge, the capacitor was charged to 1.5 V at 1 A/g, and relaxed for 24 h with the open circuit voltage (OCV) recorded. In **Figure 5.10** (green line), for the KI+KOH system, OCV remains at 0.93 V out of 1.5 V (62%) after 24 h. Interestingly, after 24 h, the OCV of the pure EDLC with KOH as the electrolyte was only 0.52 V out of 1 V. We further discovered that the thickness of separator has a significant impact on the rate of self-discharge. When switching the separator with a thickness of 180 μm to the one 9 μm thick, the self-discharge rate turns faster for the KI+KOH system. Yet, with such a thin separator, the rate of KI+KOH is still comparable to the pure KOH system with the separator 180 μm thick. Ongoing studies are focused on understanding the relatively slow self-discharge of the KI/KOH system.

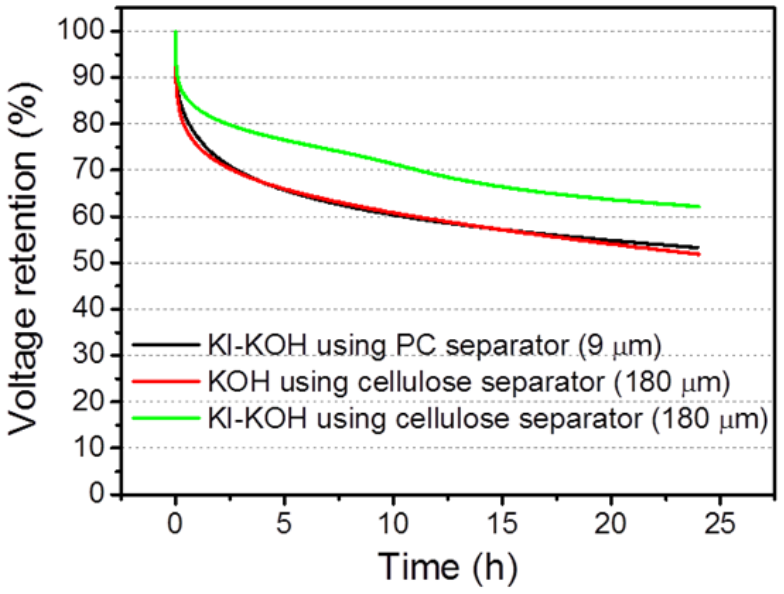

Figure 5.10 Self-discharge for 24 h with and without of KOH and with separators with different thickness.

Temperature response is another concern for aqueous capacitors. Therefore, we measured the specific energy based on the combined mass of electrodes and electrolyte and self-discharge from -20 to 50 °C in a constant temperature chamber (**Figure 5.11**). Without any additives, the KI+KOH cells can operate at -20 °C due to the freezing point depression. According to Blagden's Law, the theoretical freezing point is calculated to be -23.7 °C, which explains the performance**.**

Although we use a high concentration of KI, because of its high solubility in water, no effects due to precipitation are found even at -20 °C, so a high capacity is maintained. We observed increasing specific energy and decreasing round-trip energy efficiency as we increased the working temperature, as shown in **Figure 5.11** (A), which can be

explained by faster kinetics and diffusion rates at higher temperatures, along with an increased number of side reactions. We also found increasing internal resistance caused by slower ion movement at lower temperatures, but even at -20 °C, the IR drop is still below 0.03 V.

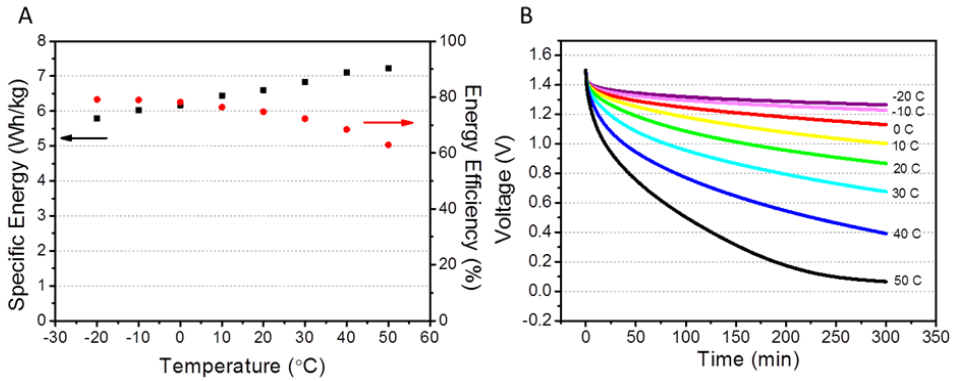

Figure 5.11 (A) Specific energy and round-trip energy efficiency at different temperatures, (B) Self-discharge for 300 min at different temperatures.

Self-discharge could be a problem when we use the cell at temperatures higher than 30 °C, due to increased diffusivity and the resulting self-discharge *via* a possible redox shuttle mechanism.[131, 132] As shown in **Figure 5.11** (B), after 5 h at open circuit voltage, the OCV dropped to 0.4 V (or lower) at working temperatures above 40 °C. However, when tested at low temperature, self-discharge was slowed down dramatically. Below -10 °C, the cell voltage only dropped to 1.2 V after 5 h.

5.5 Conclusions

The advanced redox electrolyte of KI-KOH combines two redox energy-storage processes in aqueous electrochemical capacitors: hydrogen adsorption/desorption and IO_3^-/I^- redox reactions. With the presence of KOH, we are able to charge the cell to 1.6 V and achieve a specific energy above 7 Wh/kg (accounting for the mass of both electrodes and electrolyte) and an average specific power above 6200 W/kg. Excellent cyclability is obtained with only 7% loss in device specific energy after 14000 cycles. For self-discharge, over 62% of the voltage remains after 24 h, slower than traditional EDLC (6 M KOH). The large operating temperature window is practically important. This electrolyte thus constitutes important progress in the development of "redox-enhanced" electrochemical capacitors, as it promises an efficient mechanism to increase the storage of electrical energy with long cycle life and the potential for low cost and safe operation.

6 Maintaining pH Difference at Each Electrodes to Expand the Operating Window of Aqueous ECs

6.1 Abstract

We introduce a novel bipolar assembly of ion-exchange membranes as the separator for aqueous supercapacitors. The new bipolar separator enables the positive electrode and the negative electrode to operate in acidic electrolyte and alkaline electrolyte, separately. The bipolar separator increases the theoretically stable voltage window from 1.23 to 1.76 V for the device when pH 1 and pH 10 are selected for the positive and negative electrode, respectively, based on the pH tolerance of commercial ion exchange membranes. By considering the results from comprehensive electrolyte stability investigation, we charge the cells to 1.8 V, which increases the maximum cell discharge voltage to 1.77 V. A specific energy of 12.7 Wh/kg is achieved based on the electrodes' mass, which is twice the value of the comparative best performing single electrolyte. The new cell configuration with the three-compartment bipolar separator effectively prevents the acid/base electrolyte cross diffusion, where after 10,000 cycles, the capacitance retention is 97% with coulombic efficiency maintained above 99.6% all through cycling. The design here may open up a new avenue toward high-energy aqueous energy storage devices.

6.2 Introduction

Supercapacitors, also known as ultracapacitors or electrochemical capacitors (ECs), are highly complementary to batteries by providing high power density and ultra-long cycling life that the state-of-the-art batteries have yet to achieve.[5] These devices are indispensable in applications, including power cranking for transportation, energy recovery in heavy-duty systems[133] and potentially laser generation. In order to develop more powerful ECs, prior works have studied the impacts of carbon electrodes' properties on ECs' performance, including surface area,[98, 121, 134-137] pore size,[7-9, 100, 101, 138] heteroatom doping,[139-143] and pseudocapacitance.[102, 144-150] Recently, attention has also been paid to redox-active electrolytes.[58, 117, 151-153]

As well known, most commercial ECs employ non-aqueous electrolyte rather than aqueous electrolyte despite the facts that aqueous electrolytes are typically more conductive, safer and cheaper. The overwhelming advantage of non-aqueous electrolyte is its much wider stable electrochemical potential window than its aqueous counterpart, where the latter is limited to 1.23 V, the potential gap between the hydrogen evolution reaction (HER) and oxygen evolution reaction (OER).[5] Therefore, the operating voltage for aqueous ECs is normally below 1.2 V, whereas it is as high as 3.0 V for non-aqueous devices. The energy density of capacitors obeys the following equation: $E = \frac{1}{8}CV^2$, where C is the specific capacitance of one electrode and V is the maximum discharge voltage of a device. Although the electrode capacitance in aqueous ECs is often higher than that in non-aqueous ECs, the overall energy density of the former still falls far below what the latter could offer.

In order to cultivate the advantages of aqueous supercapacitors, it is highly desirable to increase its operating voltage without decomposing its electrolyte. One example is lead-acid batteries that operate at a voltage above 2.0 V, which is facilitated by the high HER and OER overpotentials on Pb and PbO_2 electrodes, respectively.[154] However, porous carbon electrodes do not afford the same levels of HER and OER overpotentials in supercapacitors. It is well known that the theoretical potentials of OER and HER shift along pH values according to the Nernst equation and water Pourbaix diagram. However, varying pH values does not affect the electrochemical window of water, which is constant as 1.23 V. Heteroatom doping in carbon structures may affect the overpotentials of HER and OER. Bichat et al. reported that seaweed-derived activated carbon doped with 11.5 at% oxygen and 2.6 at% N can be cycled in cyclic voltammetry (CV) at a scan rate of 2 mV/s to a maximum cell voltage of 2.4 V in an aqueous electrolyte of 0.5 M Na_2SO_4 without obvious water decomposition.[140] However, at a current density of 1 A/g in galvanostatic charge/discharge, the doped carbon electrodes can only be charged to 1.6 V as the maximum cell voltage. The electrolyte salts mater as well, where due to the strong solvation effect of Li^+ and SO_4^{2-} ions, ECs using a Li_2SO_4 electrolyte can be cycled to 2.2 V in CV tests.[66] Very recently, Suo et al. reported a "water-in-salt" aqueous electrolyte with 21 m LiTFSI in lithium-ion batteries, which can be polarized to 3.0 V. The high voltage is attributed to the reduced water activity due to the water coordination around Li^+ and the passivation effect from the reduced $TFSI^-$ ions.[155]

Hydrogen electrosorption on nanoporous carbon electrodes is another approach to increase the effective charge storage. While our paper is under revision, Fic et al. reported that, in 6 M KOH electrolyte, the negative electrode could be polarized to -1.7 V vs Standard Hydrogen Electrode (SHE) under CV at a scan rate of 5 mV/s without substantial HER occurance, whereas the thermodynamic HER potential at this pH is -0.83 V vs SHE.[156] In this work, the authors designed a three compartment-cell, where the negative electrode side contains 6 M KOH electrolyte for hydrogen electrosorption, the positive electrode side employs either 1 M H_2SO_4 or 5 M $LiNO_3$ electrolyte for OER overpotentials, and the two electrodes are separated by a glass-fiber membrane. Most importantly, the glass fiber membrane as a seperated electrolyte compartment contains a pH 7 phosphate buffer solution mixed with 5 M $LiNO_3$, where the main objective of the setup is to maintain different pH values at each electrode. Impressively, the voltage of the reported aqueous supercapacitor could be extended to 2.1 V in the CV tests without obvious electrolyte decomposition. However, the authors also pointed out that in addition to reversible electrosorption, hydrogen evolution may occur and aggravate the efficiency and cycling stability. In addition, the electrolyte mixing could occur due to the diffusion driven by the concentration gradient, which may partially contribute to the moderate fading with 86% capacitance retention in the first 5000 cycles.

Theoretically, the voltage window of aqueous electrolytes can be dramatically increased by having the positive and negative electrodes operate in decoupled acidic and alkaline electrolytes, respectively, even without hydrogen electrosorption. **Figure 6.1** shows that if the pH value near the positive electrode is 0, whereas it is 14 for the negative electrode, the thermodynamically stable voltage window for the aqueous device can be increased from 1.23 to 2.06 V. The challenge is to separate the acidic/alkaline electrolytes completely and prevent the concentration-driven diffusion between them.

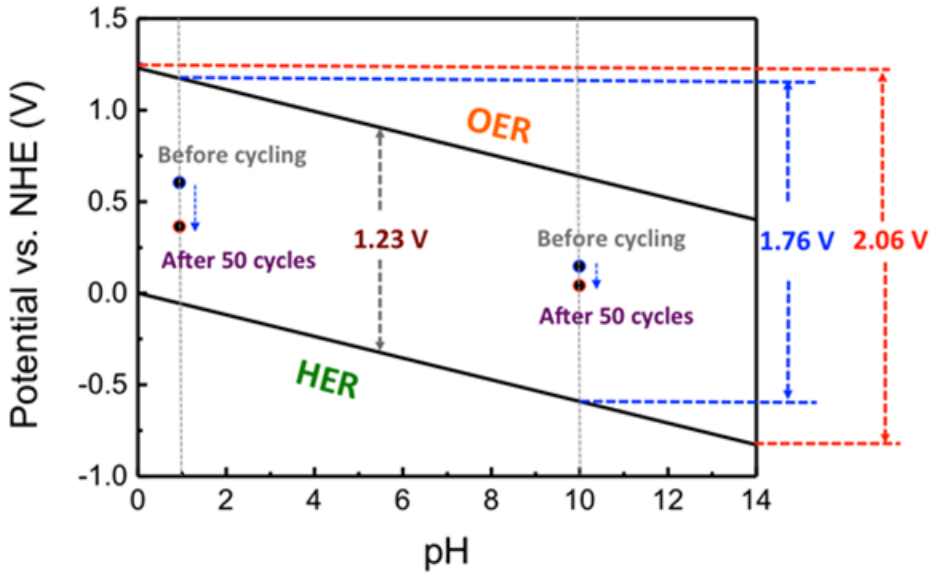

Figure 6.1 Pourbaix diagram of water, where the potential is plotted as a function of pH values.

Herein, we introduce a bipolar assembly of ion-exchange membranes (IEMs) as the separator for aqueous supercapacitors, which enables positive and negative electrode to operate in acidic and alkaline electrolyte, separately, thus increasing device-

operating voltage. The new device is referred to as Bipolar-EC. The bipolar assembly is formed by laminating an anion-exchange membrane (AEM), a glass fiber membrane and a cation-exchange membrane (CEM). It is well known that IEMs are composed of polymeric backbones, which are surface tethered with either positively or negatively charged functional groups. Through the IEMs, ions with the same nature as the functional charged groups are blocked while counter ions are allowed to diffuse to compensate for charge neutrality.[36, 37] With such unique properties, IEMs play important roles in electrodialysis,[157] fuel cells,[158] chemical separation,[159] and environmental conservation.[160] Nevertheless, integrating such membranes into capacitive devices for a higher specific energy has yet to be explored.

6.3 Experimental

As-purchased carbon fibers (Donacarbo S-241 from Osaka gas Co., Ltd.) are activated under CO_2 at 920 °C for 18 hours in a double-zone tube furnace (OTF-1200X-II-UL from MTI) with a flow rate of 229 cc/min. Activated carbon, carbon black (Super P), and polytetrafluoroethylene (PTFE) with the mass ratio of 8:1:1 are dispersed into amyl acetate and sonicated for 2 hours. The slurry is ground and dried in a mortar at room temperature and then rolled with a rolling machine to prepare freestanding films (active mass loading: ~3 mg/cm^2), which is better dried afterwards at 80 °C in a vacuum oven overnight to remove solvent residue.

The anion exchange membrane (AMI-7001 from Membranes International Inc.) is composed of gel polystyrene cross-linked with divinylbenzene with quaternary ammonium functional groups on the surface, and Cl^- as the initial mobile counter ions. The cation exchange membrane (CMI-7000 from Membranes International Inc.) comprises gel polystyrene cross-linked with divinylbenzene with sulfonic acid functional groups on the surface, and Na^+ as the initial mobile counter ions. The IEMs are immersed into 1 M Na_2SO_4 for 12 hours to allow hydration and expansion before assembling the cells.

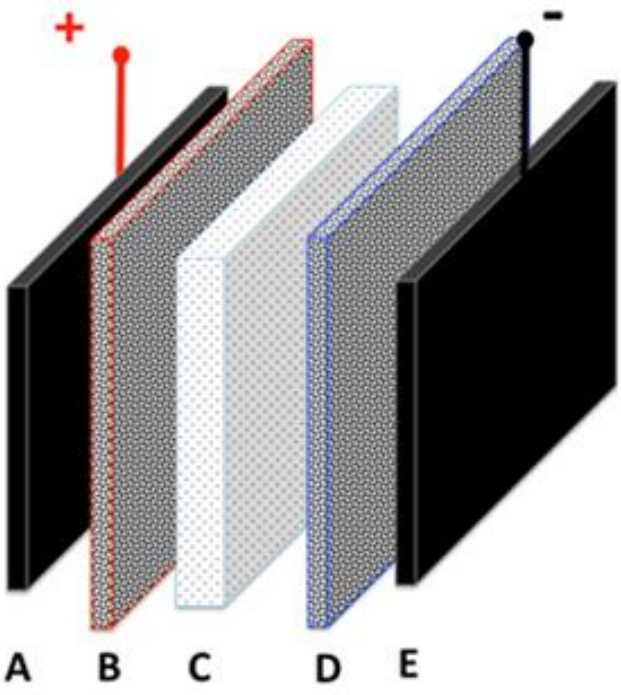

Figure 6.2 Schematic of the new design of supercapacitors. A, Positive electrode of activated carbon. B, Anion-exchange membrane. C, Glass fiber membrane. D, Cation-exchange membrane. E, Negative electrode of activated carbon.

Figure 6.2 shows the setup of the Bipolar-EC, where the membranes divide the cell electrolyte into three compartments. On the positive side reside 0.1 M H_2SO_4 and 1 M Na_2SO_4, where the AEM blocks cationic diffusion, including hydroniums (H_3O^+). On the negative side, the electrolyte comprises 0.1 mM NaOH and 1 M Na_2SO_4, where the CEM inhibits the diffusion of anions, including hydroxides (OH^-). Here, we choose the pH values of the acidic and alkaline electrolytes according to the pH-tolerance window of IEMs—from pH 1 to 10. Importantly, in between the IEMs exists a glass fiber membrane that contains neutral electrolyte of 1 M Na_2SO_4, which acts as a salt bridge to provide charge compensation during device operation. Na_2SO_4 is selected based on the counter ions in the acidic and alkaline electrolyte compartments. The acidic side uses H_2SO_4, which requires the middle electrolyte to be a sulfate salt, thus minimizing the variables. For sulfate-based salts, relevant candidates are K_2SO_4 and Na_2SO_4. Yet, K_2SO_4 has a low solubility of 0.69 M at room temperature, whereas the solubility of Na_2SO_4 can reach 1.3 M. Therefore, Na_2SO_4 is chosen to be the supporting middle electrolyte. Briefly, during charging, the positive and negative electrodes will electrostatically attract anions and cations, respectively, to form electrical double layers (EDLs), where SO_4^{2-} and Na^+ from the central neutral electrolyte can diffuse through AEM and CEM, respectively, for charge compensation. During discharging, the ion migration reverses their directions through IEMs.

Activated carbon is degassed under N_2 at 250 °C for 4 hours to remove absorbed gas inside the pores. N_2 sorption is conducted with the degassed sample at -196 °C by Micromeritics TriStar II 3020 analyzer to calculate the Brunauer-Emmett-Teller (BET) surface area and pore size distribution.

The morphology of carbon fibers, activated carbon, and IEMs is characterized through scanning electron microscope (SEM) with FEI QUANTA 600F environmental SEM instrument.

All electrochemical tests, including cyclic voltammetry (CV) galvanostatic charge/discharge, and electrochemical impedance spectroscopy (EIS) are carried out on Bio-logic VMP3 instrument. Long-term cycling is tested on Maccor Series 4000. In the half-cell S value tests, CV is conducted in 0.1 M H_2SO_4/1 M Na_2SO_4, and 0.1 mM NaOH/1 M Na_2SO_4, respectively, at 1 mV/s in a three-electrode cell configuration, with Ag/AgCl as the reference electrode. In Bipolar-EC, CV is conducted at 1 mV/s at polarizing voltages of 1, 1.2, 1.5, 1.8, 1.9, 2.0, 2.1, and 2.2 V. Galvanostatic charge/discharge is conducted at 1 A/g for cycling tests, and at 0.1, 0.2, 0.5, 1.0, 2.0 A/g for the rate capability tests. EIS is carried out in the frequency range from 10 mHz to 200 kHz with an amplitude of 10 mV. Leakage current tests are conducted by applying a constant voltage to the cell, where the current is recorded for 10 minutes. Potential of zero charge (PZC) is measured by examining the instantaneous open circuit

voltage (OCV) between the working electrode and the Ag/AgCl reference electrode when placing the carbon film working electrodes into different electrolytes.

S values are calculated by the following equation:[161, 162]

$$S_{pos} = \frac{Q_{pos}}{Q_{neg}} - 1$$

$$S_{neg} = \frac{Q_{neg}}{Q_{pos}} - 1$$

where Q_{pos} and Q_{neg} are integrated areas for anodic current over time and cathodic current over time, respectively, in CV curves. It is used to show whether irreversible reactions occur on either positive or negative electrodes.

6.4 Results and Discussion

We conduct CV tests at a low scan rate of 1 mV/s in a three-electrode cell to determine the onset positive and negative potentials, where water decomposition occurs in individual acidic or alkaline electrolytes. These individual electrolytes are of the same concentrations as the corresponding counterparts in the Bipolar-EC, and the single-electrolyte cells only employ a glass fiber membrane as the separator.

The onset potentials can be evaluated by S values.[161, 162] By defining S = 0.1 as the limit value for water decomposition, the highest potential for the positive electrode in H_2SO_4 electrolyte and the lowest potential for the negative electrode in the alkaline electrolyte are determined to be 0.7 V and -1.0 V vs Ag/AgCl, respectively.

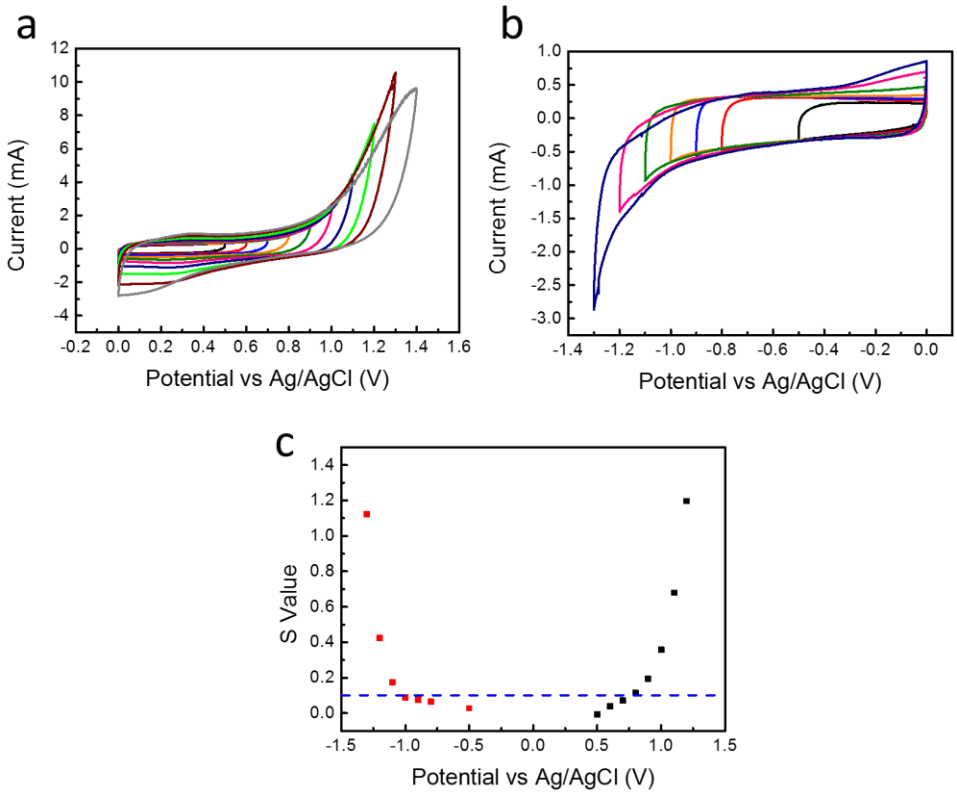

Figure 6.3 Cyclic voltammetry at 1 mV/s with different cutoff potentials for cells using (a) 0.1 M H2SO4 and 1 M Na2SO4, (b) 0.1 mM NaOH and 1 M Na2SO4. (c) S value determined at various potentials in acidic electrolyte (right) and alkaline electrolyte (left).

At mild cutoff voltages, rectangular CV curves are obtained, revealing ideal capacitive charge storage mechanism. As the cutoff potential goes more positive in the acidic electrolyte (**Figure 6.3** a) and more negative in the alkaline electrolyte (**Figure 6.3** b),

irreversible currents start to be more pronounced with higher S values (**Figure 6.3** c), most likely caused by OER and HER. Therefore, the largest allowed electrochemical window of Bipolar-EC is determined to be 1.7 V, consistent with the thermodynamic value of 1.76 V from Pourbaix diagram.

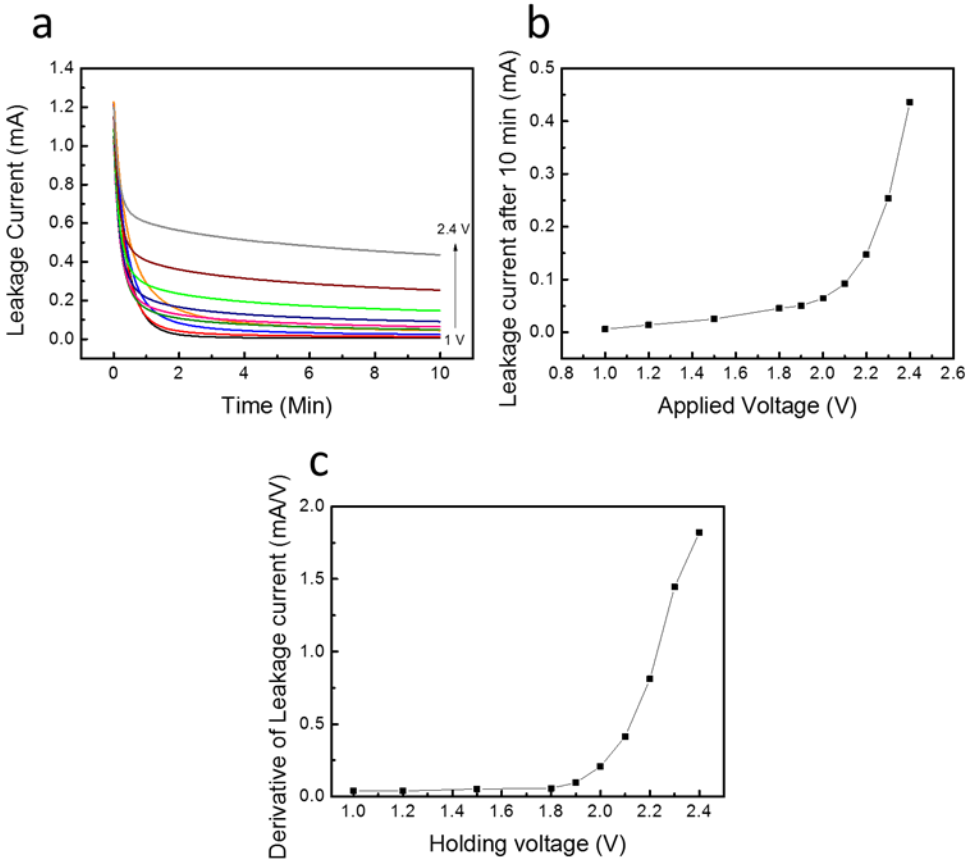

Figure 6.4 (a) Leakage current as a function of time while applying voltages of 1, 1.2, 1.5, 1.8, 1.9, 2.0, 2.1, 2.2, 2.3, and 2.4 V, (b) leakage current after 10 hours as a function of applied voltages, (c) derivative of leakage current as a function of held voltages.

We also carry out leakage current tests by applying different constant voltage on Bipolar-EC, as shown in **Figure 6.4** a. In an ideal RC circuit, the current response is

linearly proportional to the applied voltage. A significant current increase upon a certain bias, known as leakage current, indicates non-capacitive behavior, which is most likely due to the electrolyte decomposition. To gain more straightforward presentation, we take the derivative of the leakage current, where the first sharp increase in current derivative is observed at 1.9 V (**Figure 6.4** c).

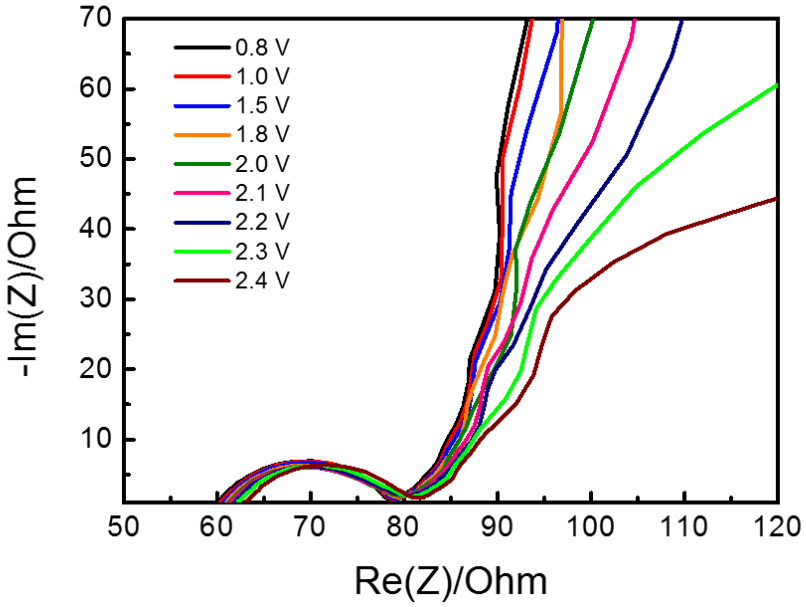

Figure 6.5 Nyquist plot when charging Bipolar-EC to various voltages.

We further collect electrochemical impedance spectra (EIS) at different charging voltages to pursue the largest allowed voltage (

Figure 6.5). No significant change is observed at the high frequency region with semicircles of similar diameters. Upon cell voltage increasing, in the intermediate and low frequency regions, the slope values of the lines decrease, indicating increasing

values of Warburg resistance as well as slower ion diffusion in the bulk electrolyte. Particularly, above 2.2 V, the slope of the low-frequency lines drops dramatically. We attribute the higher resistance observed at higher cell voltages to the possible gas evolution and the consequent interruption to the ion diffusion.

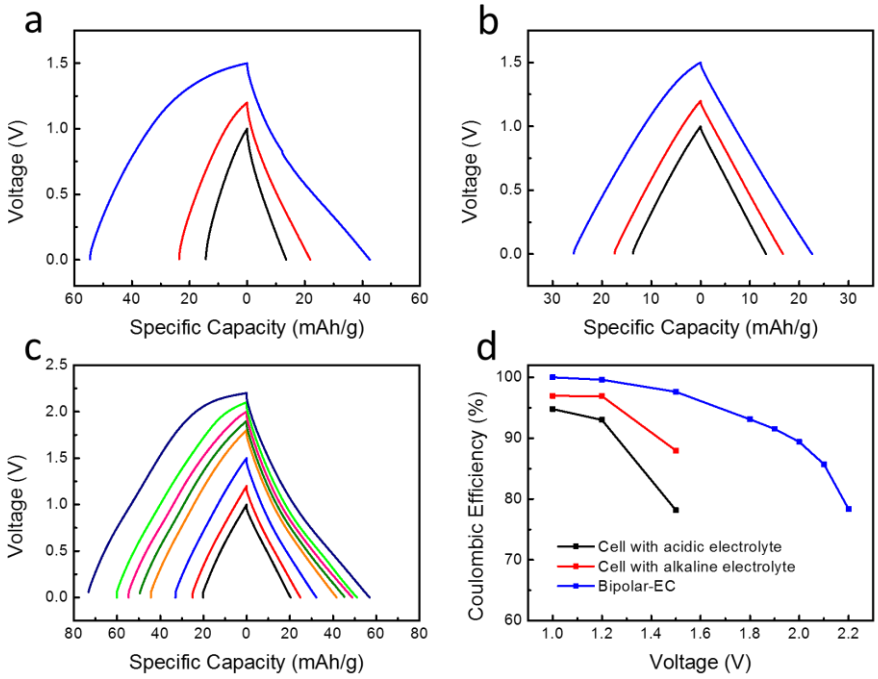

Figure 6.6 Galvanostatic charge/discharge profiles from the cells with (a) 0.1 M H_2SO_4/1 M Na_2SO_4, (b) 0.1 mM NaOH/1M Na_2SO_4, (c) Bipolar-EC, and (d) the coulombic efficiency of each cell at various cutoff voltages.

In order to further determine whether the bipolar assembly as a separator helps enlarge the stable electrochemical window of aqueous electrolytes, we collect and compare two-electrode GCD results upon ramping up maximum charging voltages between cells with individual acidic electrolyte or alkaline electrolyte, and Bipolar-EC, as shown in **Figure 6.6**. To clarify unambiguously if there is electrolyte decomposition, a constant

current rate of 0.1 A is employed. At 1.5 V, the coulombic efficiency (CE) drops to 78% with the acidic electrolyte and 88% with the alkaline electrolyte (**Figure 6.6** a, b). For the alkaline electrolyte, charging cannot reach a potential above 1.75 V. In sharp contrast, even at 2.0 V, the CE of Bipolar-EC remains above 89% (**Figure 6.6** c, d). Above 2.0 V, a charging plateau starts to appear for Bipolar-EC, which is most likely due to water decomposition.

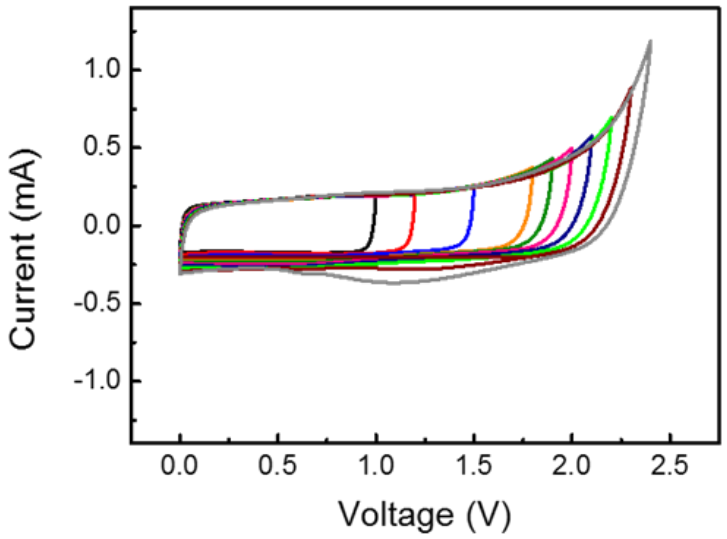

Figure 6.7 Cyclic voltammetry at 1 mV/s with Bipolar-EC at various cutoff voltage

Figure 6.7 shows CV curves of Bipolar-EC at increasing cutoff voltages. At low cutoff voltages (less than 1.8 V), rectangular CV curves show symmetric cathodic and anodic current responses, indicating ideal capacitive behavior. Based on the S value tests (**Figure 6.3**), leakage current tests (**Figure 6.4**), cyclic voltammetry at 1 mV/s (**Figure 6.7**) and the charge/discharge tests at 0.1 A/g (**Figure 6.6** c), 1.8 V is chosen to be highest charging voltage of Bipolar-EC. As further confirmation, we conduct

galvanostatic charge/discharge with three electrode cell configuration. When the cell voltage is charge up to 1.8 V, the negative electrode is polarized to -0.91 V vs Ag/AgCl, which is only 0.12 V lower than HER potential at pH of 10. Considering that this low overpotential may be overestimated due to the Ohmic resistance, hydrogen electrosorption must be a minor event, supported by absence of redox peaks upon scanning to 1.8 V at 1 mV/s (**Figure 6.7)**.

If 1.0 V and 1.2 V are considered as the highest operating voltage for acidic electrolyte and alkaline electrolyte, respectively, at 0.1 A/g, Bipolar-EC is able to deliver a specific energy of 12.7 Wh/kg, more than 4 times that of acidic electrolyte (2.7 Wh/kg), and more than twice that from alkaline electrolyte (4.9 Wh/kg). Moreover, compared to aqueous EDLCs in the literature,[44] at a low current rate when IR drop is not an issue, Bipolar-EC shows three-fold improvement on energy density.

We notice from **Figure 6.6** b that the alkaline electrolyte at pH 10 exhibits better tolerance on high cell voltages than the acidic electrolyte. We are also aware that most reported high-potential aqueous ECs used pH-neutral electrolytes.[16, 34] To understand this phenomenon, we measure the potential of zero charge (PZC) for the carbon film electrodes in acidic or alkaline electrolytes before cycling. At pH 10, the measured PZC is -0.051 V vs Ag/AgCl (0.15 V vs NHE), while at pH 1, the PZC is 0.39 V vs Ag/AgCl (0.59 V vs NHE). At pH 1, the PZC is almost right in the middle of the voltage gap between HER and OER potentials, allowing similar extents of polarization

on both positive and negative electrodes, thus fully taking advantage of the water voltage window (**Figure 6.1**). Therefore, a higher cell operating voltage is expected in an acidic electrolyte. However, the opposite is observed for the cells that have been through initial cycling (50 cycles) as aforementioned. In fact, after initial cycling, the shared electrode potential upon cell short circuit (PSC) at pH 10 drops to -0.14 V vs Ag/AgCl (0.057 V vs NHE), moving toward the center of the HER/OER gap, while the PSC at pH 1 decreases to 0.11 V vs Ag/AgCl (0.31 V vs NHE), moving away from the center of the HER/OER gap, being much closer to HER. In fact, the PZC of the negative electrodes should be even lower than the PSC values. Thus, in a symmetric cell, HER would be more likely to take place in the acidic electrolyte before the positive electrode is fully polarized. The evolving PSC and PZC of electrodes explain why a higher operating voltage is observed in the basic electrolyte rather than in the acidic electrolyte.

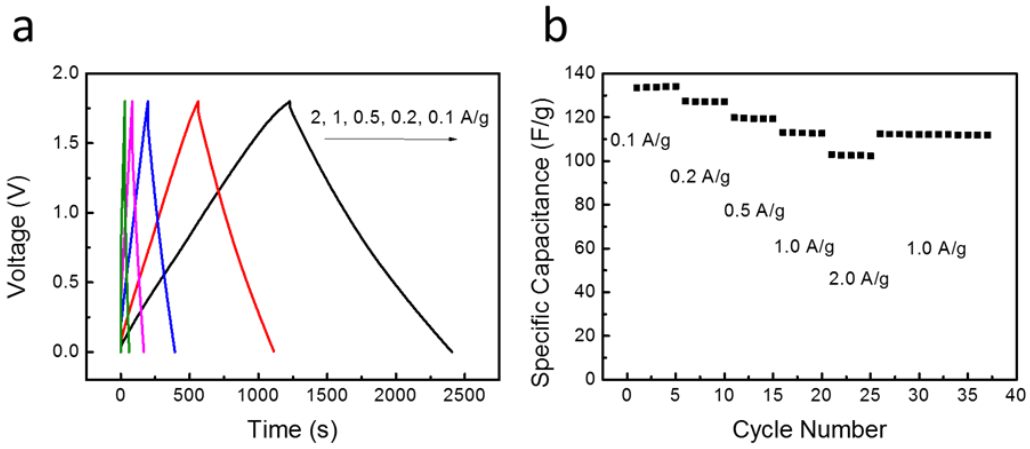

Figure 6.8 (a) Charge/discharge profiles of Bipolar-EC cells at various current rates and (b) rate-cycling at various current rates of 0.1, 0.2, 0.5, 1.0, and 2.0 A/g.

To investigate the rate capability, Bipolar-EC is tested at various current rates, ranging from 0.1 A/g to 2 A/g, where the capacity only decreased from 134 F/g to 103 F/g, as shown in **Figure 6.8**. However, one issue with the current Bipolar-EC is its relatively high resistance, compared to traditional EDLC, which can be seen from the IR drop in the charge/discharge profiles, causing low energy efficiencies.[163] At 0.1 A/g, the IR drop is 31.8 mV, leading to an energy efficiency of 75%, while the IR drop increases to 314 mV at 1 A/g, lowering the energy efficiency to 62%. The high resistance of the device is attributed to longer ion diffusion length and limited ion conductivity in IEMs. However, we are optimistic that with further development of bipolar membranes, the power performance of the Bipolar-EC would be greatly improved.

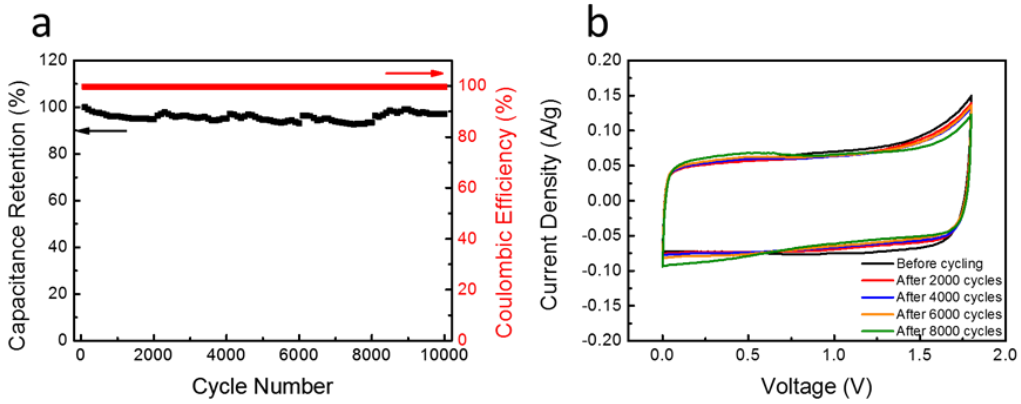

Figure 6.9 (a) Long-term cycling of Bipolar-EC at 1 A/g for 10,000 cycles, (b) cyclic voltammetry curves after 2000, 4000, 6000, 8000 cycles at 1 mV/s.

Figure 6.9 (a) shows the long-term cycling performance of Bipolar-EC at 1 A/g for 10,000 cycles. Superior cycling stability is obtained, with an initial capacitance of 113 F/g and a final capacitance of 110 F/g after 10,000 cycles, counting capacitance

retention of more than 97%. Moreover, the coulombic efficiency for the whole cycling maintains above 99.6%, indicating that the acidic and alkaline electrolytes are well separated. In order to further verify whether there is no H^+ or OH^- diffusion across the bipolar assembly, CV at 1 mV/s is conducted after every 2000 cycles. As shown in **Figure 6.9** b, at different stages of long-term cycling, the obtained CV curves are almost identical, demonstrating a lack of cross diffusion between acid and alkaline electrolyte.

6.5 Conclusions

In summary, we for the first time employ a bipolar assembly of IEMs as the separator for aqueous supercapacitors to increase specific energy. The bipolar membrane assembly decouples the reaction environment for OER and HER by blocking migration of hydronium and hydroxide ions confined in the acidic and alkaline electrolyte chambers, respectively, which effectively increases the voltage tolerance of the aqueous device. The new Bipolar-EC can be charged to 1.8 V galvanostatically, where it discharges from 1.77 V, achieving a capacitance of 113 F/g. The new cell configuration improves the energy density by three folds compared to traditional aqueous EDLCs. The capacitance retention is impressive of more than 97% after 10,000 cycles. With further optimization of the cell configuration and custom-designed IEMs, we are optimistic that our new design may cause a paradigm shift for the future development of the aqueous supercapacitors.

7 Hydronium Ions as Novel Charge Carriers in Batteries

7.1 Abstract

We first demonstrate that hydronium ion can be reversibly stored in an electrode of crystalline 3,4,9,10-perylenetetracarboxylic dianhydride (PTCDA). PTCDA exhibits a capacity of 85 mAh/g at 1 A/g after an initial conditioning process. *Ex situ* x-ray diffraction reveals reversible and significant structure dilation upon reduction of PTCDA in an acidic electrolyte, which can only be ascribed to hydronium-ion intercalation. The lattice expansion upon hydronium storage is theoretically explored by the first principles Density Functional Theory calculations, which confirm the hydronium storage in PTCDA. Our results point to a new paradigm of batteries—hydronium-ion batteries.

7.2 Introduction

Energy storage as the currently missing enabler for wide utilization of renewable energy has remained as the focus of knowledge production for the 21st century. The forefront of battery innovations has migrated from lithium-ion batteries (LIBs) to a variety of new solutions, such as Li-S batteries[164-166], Li-O_2 batteries[167, 168], sodium-ion batteries (NIBs)[28, 169, 170], and potassium-ion batteries (KIBs)[47, 171]. To date, rechargeable batteries with metal ions as charge carriers occupy the primary attention.

However, proton and hydronium, analogues of Li^+, Na^+, and K^+, have remained rarely explored as charge carriers for rechargeable batteries. Among batteries that rely on proton as charge carriers, one area is the metal alloy anode of nickel-metal hydride batteries (NiMH), which incorporates hydrogen in forming metal-hydrides during battery charging[68, 172]. Another field is the adsorption of proton/hydrogen by high-surface-area electrode materials, such as carbon nanotubes[69], and activated carbon[128, 152, 173, 174]. Qu *et al.* investigated an important mechanism of proton-intercalation in graphite electrodes, where hydrogen is predominantly stored in the galleries of graphitic domains, with small amounts stored *via* surface adsorption.[73] To date, most electrochemical hydrogen storage exhibits fairly low coulombic efficiency caused by the hydrogen evolution reaction (HER). Interestingly, all prior studies employed alkaline electrolyte, which relies on the dissociation of water molecules to provide proton/hydrogen for incorporation by the electrodes. Note that the dehydration energy of H_3O^+ is 11.66 eV[175], which is so high that in aqueous BrØnsted-Lowry acids as the electrolyte, the intercalant ions into electrode host structures will be hydronium ion, *i.e.*, H_3O^+ or its hydrated forms: $H_{2x+1}O_x^+$ instead of protons. When we consider H_3O^+ as the charge carrier for batteries, H_3O^+ exhibits an effective ionic radius of 100 ± 10 pm[176], which is very close to that of Na^+, 102 pm[177], thus not being too large to be considered. Surprisingly, to date, batteries based on electrochemical storage of hydronium ion has never been reported.

To store hydronium ion, the interstitial sites in the electrode host structures should be relatively spacious, and the ion-insertion potential needs to be high enough to avoid HER. To this end, electrodes of organic solids may be suitable, where their unique capability of storing large metal ions has been demonstrated[41, 56, 178-180]. Plus, the reduction potential of organic materials is essentially determined by their Lowest Unoccupied Molecular Orbital (LUMO), which is tunable. As an advantage over graphite electrodes, one can tether the edges of fused aromatic rings of organic molecules with electron withdrawing groups to lower the energy levels of LUMO, thus increasing the cation-insertion potentials. Thus, by this way, the cation intercalation potential can be generally higher than graphite. Among organic solid electrodes, 3,4,9,10-perylenetetracarboxylic dianhydride (PTCDA), a well-known pigment, which has been investigated to store Li^+, Na^+, and K^+[181 56, 178, 182] again catches our attention for this proof-of-concept study of hydronium-ion battery electrodes.

Herein, we, for the first time, report the evidence of hydronium intercalation into a highly crystalline organic electrode of PTCDA, which exhibits a specific capacity of 85 mAh/g, reversible structural changes over cycling, and relatively stable cycling life. We characterized the structural change upon hydronium intercalation, where *ex situ* x-ray diffraction reveals significant but reversible lattice expansion. This confirms that the intercalant ions are hydroniums instead of naked protons.

In order to test the hydronium storage properties of PTCDA, we investigate the PTCDA electrode in a three-electrode cell setup with 1 M H_2SO_4 as the electrolyte. In this cell setup, the counter electrode is composed of excessive mass of activated carbon, which also serves as the positive electrode by operating in an electrical double layer manner *via* electrostatically absorbing/desorbing anions from/into the electrolyte, *i.e.*, SO_4^{2-}. Ag/AgCl electrode in saturated aqueous KCl solution, with a potential: 0.197 V *vs.* standard hydrogen electrode, acts as the reference electrode, where all the potentials in this study are reported *vs.* Ag/AgCl reference electrode. The PTCDA electrode is tested as the working electrode and negative electrode, where during cell charging, PTCDA is reduced while incorporating cations, *i.e.*, hydroniums.

7.3 Experimental

Cell Preparation and Electrochemical Tests

PTCDA (from Sigma-Aldrich) was mixed with C-45 and Polyvinylidene fluoride (PVdF) with a mass ratio of (7:2:1) in N-Methyl-2-pyrrolidone (NMP). The slurry was pasted onto titanium foil with an active mass loading of 2.0 mg/cm^2, which was dried at 80 °C overnight. Activated carbon (AC) and AC electrodes were prepared in the same way, as published before[152], with an active mass loading of 18 mg/cm^2. Three-electrode cell was composed of PTCDA as the working electrode, AC electrode as the counter electrode, saturated Ag/AgCl as the reference electrode and 1 M H_2SO_4 as electrolyte. Glass fiber membrane was used as the separator. Cyclic voltammetry (CV)

and galvanostatic charge-discharge (GCD) were carried out on an EC-Lab VMP3 instrument, at 1 mV/s and 1 A/g, respectively.

Ex Situ Characterization

X-ray diffraction (XRD) measurement was conducted on a Rigaku Ultima IV Diffractometer with Cu Kα irradiation (λ= 1.5406 Å). Fourier transform infrared spectroscopy (FTIR) spectra were obtained in a Nicolet™ iS™ 10 spectrometer.

Simulation

Theoretical calculations were performed using the Vienna ab initio simulation package (VASP)[183-185] with projector augmented wave (PAW) pseudopotentials[186, 187] with general gradient approximation (GGA) and the Perdew–Burke–Ernzerhof (PBE) exchange-correlation functional[188]. Additionally the DFT-D3 method[189, 190] was used to account for the long-range van der waals forces present within the system. For the computational simulation, an energy cutoff of 800 eV and a 6x2x2 Monkhorst-Pack[191] KPOINT scheme were used for the Brillouin zone integration.

The PTCDA unit cell was obtained from a *.cif file[192], while the H_3O^+ molecules were inserted into various locations in the structure. The simulations performed were solely to obtain a sampling of the most favorable energy configuration, and see the evolution of the unit cell.

7.4 Results and Discussion

We collected the cyclic voltammograms (CV) of the PTCDA electrode in the three-electrode cell. In the 1st cycle, the cathodic scan reveals two minor peaks sequentially around -0.22 V (R_1) and -0.39 V (R_2), and a major peak beyond -0.49 V (R_3) (**Figure 7.1** (a). During the following anodic scan, two peaks at -0.31 V and -0.27 V show up, which we assign as O_3 and O_2, respectively, corresponding to R_3 and R_2 reduction reactions, thus exhibiting a polarization of ~0.2 V, and R_1 appears irreversible. Interestingly, after 50 galvanostatic charge-discharge (GCD) cycles at 1 A/g, CV curve in **Figure 7.1** (b) displays three pairs of redox peaks, at -0.41/-0.31 V (R_3'/O_3'), -0.33/-0.17 V (R_2'/O_2'), and -0.17/-0.05 V (R_1'/O_1'), which are quite reversible.

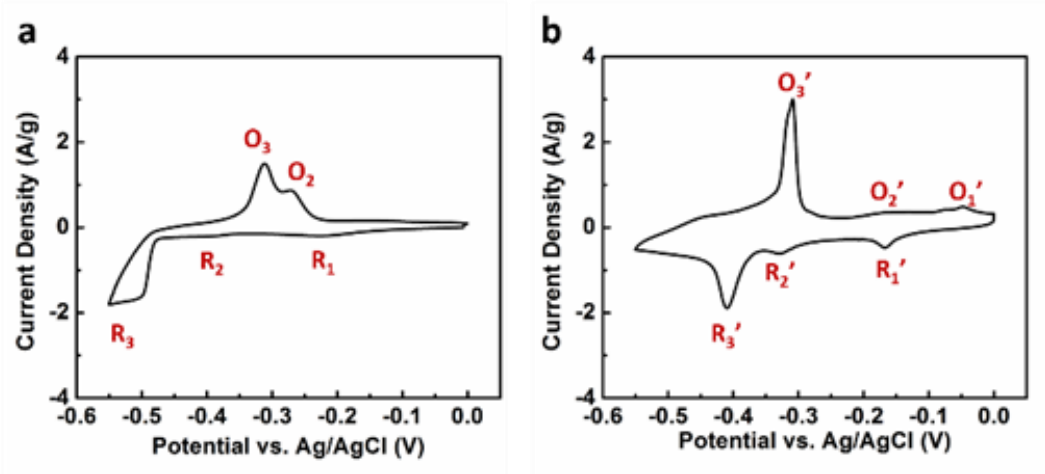

Figure 7.1 CVs at the scan rate of 1 mV/s. (a) The 1st cycle, (b) The cycle after 50 GCD cycles.

The comparison of the above two CV curves suggests that PTCDA's redox behavior in the acidic electrolyte evolves significantly simply due to the initial GCD cycling. The R_1'/O_1' pair appears only after GCD cycling; R_3'/O_3' pair exhibits much smaller polarization compared with R_3/O_3, where, interestingly, O_3' at -0.31 V does not shift at all. Overall, the extent of polarization decreases from ~0.2 V to ~0.1 V after GCD cycling, and the peak intensity of R_3'/O_3' increases slightly. The change of CV behavior features a conditioning process that occurs over initial GCD cycling, which makes redox reactions of PTCDA more amenable. The existence of multiple redox reactions, and the addition of the new R_1'/O_1' redox pair is suggestive of an interesting phenomenon that hydrated hydronium and hydronium may serve as the intercalants sequentially. The R_1'/O_1' occurs at a fairly high potential, where we postulate that hydrated hydronium, such as $H_5O_2^+$, may manage to intercalate the structures reversibly only after the initial conditioning process due to its large size. The difference of proton hydration free energy between one hydration (H_3O^+) and two hydration ($H_5O_2^+$) is calculated to be ~0.25 eV[193], corresponding to ~0.25 V of the potential penalty for dehydration from $H_5O_2^+$ to H_3O^+, which is pretty close to the potential difference of ~0.24 V between R_1' and R_3'. We tentatively attribute the R_3'/O_3' and R_1'/O_1' redox reactions to the insertion/extraction of H_3O^+ and $H_5O_2^+$ ions, respectively.

In the first GCD cycle at 1 A/g, PTCDA electrode exhibits a large polarization (**Figure 7.2** a), which is consistent with the gaps between the redox peaks in initial CV curves (**Figure 7.1** a). Interestingly, the capacity of 70 mAh/g obtained in the first reduction

sweep is close to the theoretical capacity of 68 mAh/g when every PTCDA molecule stores one electron/monovalent cation. In the fifth cycle, the polarization is much lowered, where the reduction of PTCDA occurs at higher potentials, and the capacity increases to 85 mAh/g (**Figure 7.2** b), corresponding to incorporation of 1.3 monovalent cations per PTCDA molecule. Similar to the CV results, the potentials for the oxidation sweep remain nearly the same.

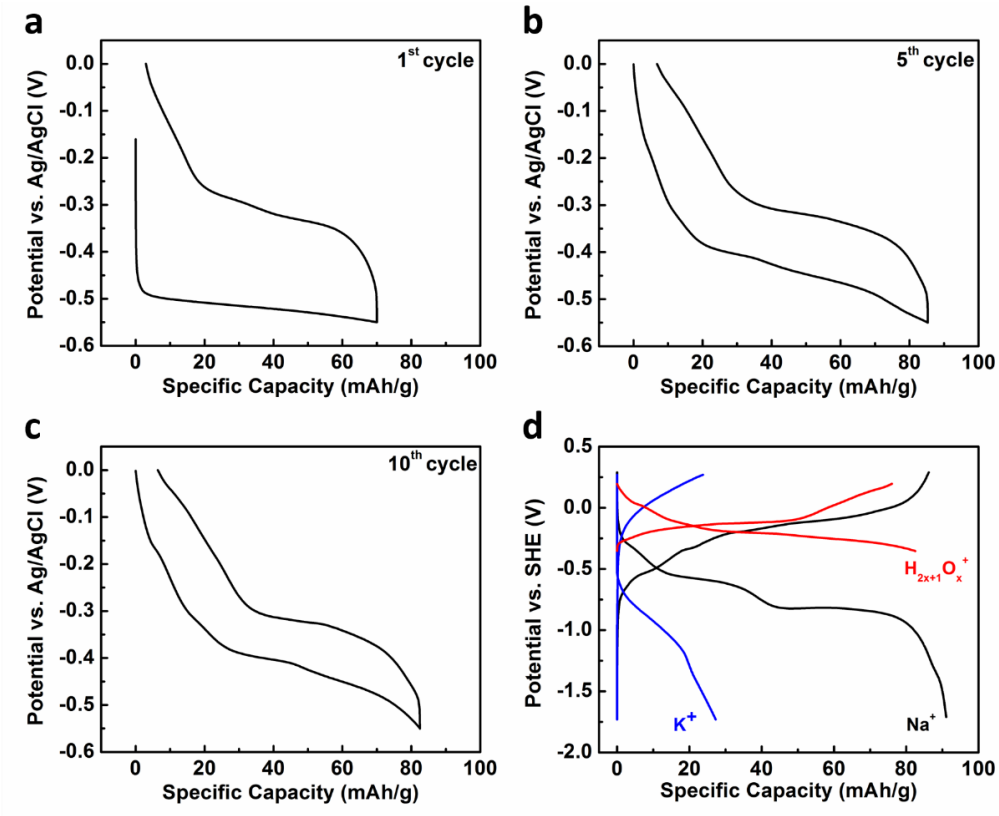

Figure 7.2 GCD profiles of (a) The 1st cycle, (b) The 5th cycle, (c) The 10th cycle, and (d) A comparison between GCD profiles of the storage of Na-ion at 1 A/g[14], K-ion at 0.5 A/g and hydronium (the 10th cycle) at 1 A/g in PTCDA.

Clearly, the initial polarization of the PTCDA electrode mainly comes from the conditioning "effort" of the cation incorporation during PTCDA's reduction. Moreover, in the 10th cycle, the potential of the charging (reduction) process eventually transforms to be two sequential plateaus at -0.17 V and -0.41 V besides some sloping regions, and correspondingly, there exist two plateaus at -0.34 V, and -0.05 V (minor) during the discharging (oxidation) process, which is generally consistent with the CV results in **Figure 7.1** (b).

PTCDA has demonstrated its unique storage capability toward large metal ions, *i.e.*, Na^+ and K^+, where its structure can reversible dilate and contract when hosting/extracting Na^+ ions[182], while its structure turns amorphous upon initial cycling by incorporating large K^+ ions[178]. It is quite intriguing that the operation potential for the hydronium intercalation is significantly higher than that of Na-ion by ~0.5 V and K-ion by ~ 1.0 V on average. The polarization for hydronium storage is also smaller by a large extent comparing to both Na-ion and K-ion. The much higher insertion potential indicates that it is thermodynamically more facile for the PTCDA framework to host hydronium ions. The favorable energetics may have to do with the smaller desolvation energy of hydroniums compared to Na^+ or K^+ ions in their non-aqueous electrolyte based on ethylene carbonate (EC) and diethyl carbonate (DEC). The minimal polarization may be related to the fast migration of hydronium ions through the PTCDA's structure. Of course, the higher conductivity of the aqueous acidic electrolyte may play a role as well.

It is critical to learn the structural response of PTCDA toward hosting hydronium ions. If the structure does dilate upon PTCDA's reduction, the possibility of proton intercalation in the structure would be trivial. Thus, we investigate the evolution of PTCDA's crystal structure during cycling by *ex situ* x-ray diffraction (XRD) measurements conducted at different state of charge (SOC) in the 50th cycle.

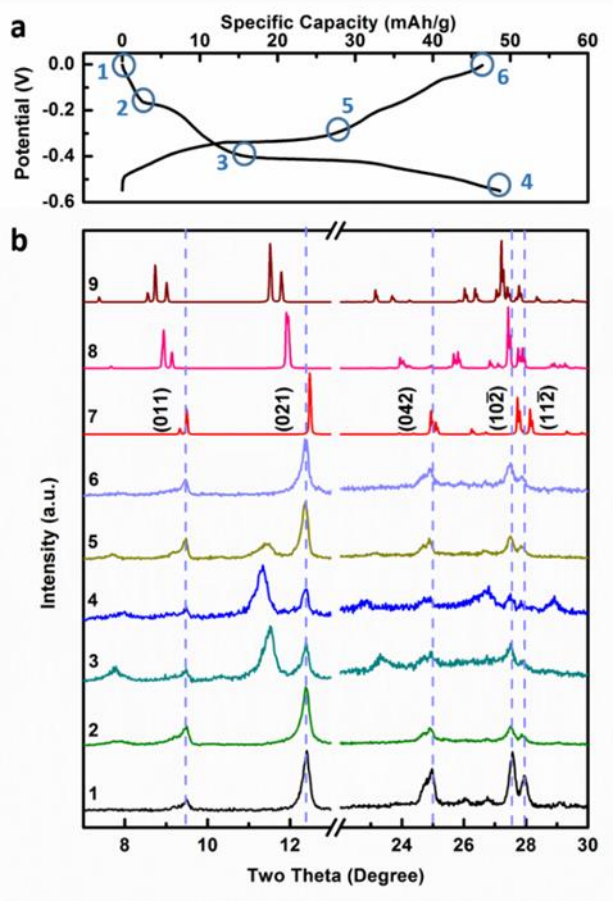

Figure 7.3 Charge/discharge (Reduction/Oxidation) profiles of the PTCDA electrode in the 50th cycle, (b) XRD patterns (No.1 to 6) of the PTCDA electrode corresponding to 1 to 6 point of SOC in The patterns of No. 7, 8, 9 are simulated XRD patterns from pristine PTCDA, PTCDA with one H_3O^+ inserted per unit cell, and PTCDA with two H_3O^+ ions intercalated per unit cell.

Figure 7.3 b depicts specific angle regions where primary peak shifts and new peak generation are observed. Upon charging (reduction) to -0.17 V (Pattern No.2), a minor peak appears at 7.8°, which will be assigned as (001) peak by simulation, and the (011) peak turns asymmetric, being slightly left-shifted. When further charging to -0.40 V (Pattern No.3), the new (001) peak at ~ 7.7° is intensified. Furthermore, there appear a strong peak at 11.6° on the left of the weakened (021) peak and a relatively weak peak at 23.4° on the left of the weakened (042) peak. We attribute the above two peak-shifts to the diffraction of the dilated (021) and (042) planes, respectively, where the d-spacings increase from 0.72 to 0.77 nm, and from 0.36 to 0.38 nm, respectively. Such a large-scale structural expansion could not possibly originate from the intercalation of naked protons, and so we are left to conclude that the reduction of the PTCDA electrode in an acidic electrolyte corresponds to intercalation of hydronium ions. As the PTCDA electrode is further charged to -0.55 V (Pattern No.4), it is observed that the new peaks derived from (021) and (042) peaks continue to shift to lower angles, and their intensity is further strengthened. Moreover, at -0.55 V, the $(10\bar{2})$ peak also shifts from 27.6° to a lower angle of 26.7° in response to the intercalation of hydronium ions. Furthermore, there appears a new peak at 28.9°, which is assigned as (130) from the simulation results.

We should note that besides appearance of new peaks, the shifts of peaks are incomplete with the presence of both the original peaks and shifted peaks at the charged states, which indicates that portions of the pristine PTCDA domains, most likely the cores of

large particles, remain intact. During the following discharge (oxidation), all the peaks gradually shift back to their original positions. Upon discharging to -0.3 V (Pattern No.5), the intensity of the new (001) peak, and the shifted (021) and (042) peaks all decreases. When discharging to 0 V (Pattern No. 6), all new peaks disappear, and the intensity of the original peaks recovers, which is almost identical to Pattern No.1, demonstrating PTCDA's excellent structural reversibility upon intercalation/deintercalation of hydronium ions.

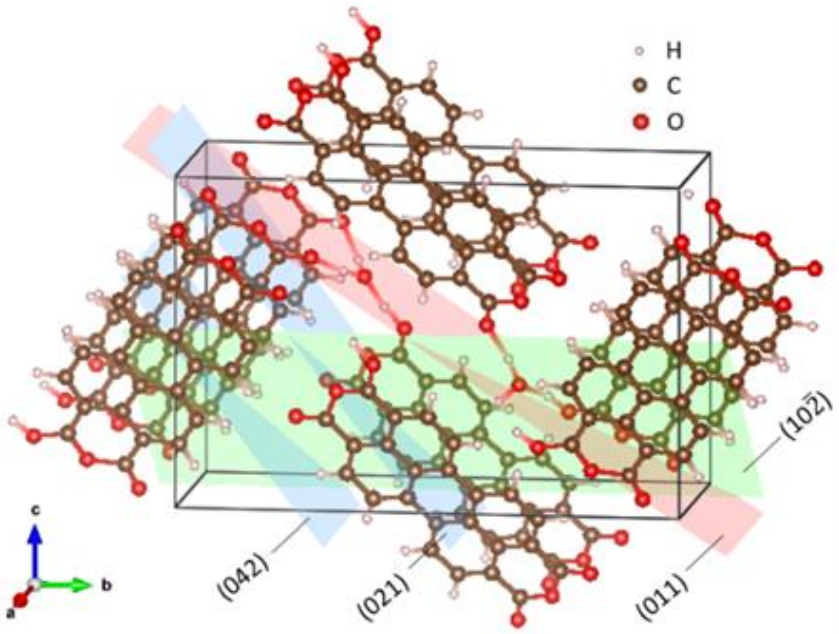

Figure 7.4 Simulated PTCDA unit cell incorporating two H_3O^+.

We also explore the mechanism of hydronium insertion in PTCDA via theoretical *ab initio* structural calculations using density functional theory (DFT) with the Vienna-Ab *initio* simulation package (VASP). Note that hydronium ions could have higher

hydration numbers; however, detailed theoretical investigation of hydration numbers is beyond the scope of this paper. Therefore, H_3O^+, the smallest hydrated proton with the least steric hindrance is chosen as the intercalation species in the simulation experiment. In **Figure 7.4**, we computed the situations with two hydronium ions incorporated in one PTCDA unit cell that comprises two equivalent PTCDA molecules, where the theoretical capacity is 68 mAh/g.

As shown in **Figure 7.4**, when two hydronium ions (H_3O^+) are intercalated into the unit cell, they stay in the interstitial space between stacked PTCDA molecules along (011) and (021) planes, and are stabilized by adjacent carbonyl groups. Simulated diffraction patterns are shown as Patterns No. 7, 8, and 9 for the pristine, the unit cell with one hydronium, and the unit cell with two hydronium ions, respectively (**Figure 7.3** b). When hydronium ions are intercalated into the PTCDA lattice, new diffraction peaks (001) and (130) around ~ 7.7° and 28.9°, respectively, appear, which generally matches the experimental results. The (021), (042) and $(10\bar{2})$ are all increasingly shifted to the left from one hydronium inserted per unit cell to two hydronium ions accommodated per unit cell, which is in agreement with experimental XRD results.

The well-matched experimental and simulation patterns provide a solid ground to look at the simulation-derived parameters. From **Figure 7.4**, it is straightforward to know the specific positions of hydronium ions in the host lattice, which are along one body diagonal on (011) plane, resulting in interlayer expansion of (021), (042), $(10\bar{2})$, and

$(11\bar{2})$. **Table 7-1** summarizes the cell parameters of pristine and hydronium-intercalated PTCDA unit cells. Apparently, the unit cell expands along ***b*** and ***c*** direction after hydronium-ion intercalation, which is consistent with peaks shift of (021) and (042) planes, leading to an expansion of unit cell volume from 757.71 to 813.01 $Å^3$ (expansion by 7.3%) when two hydronium ions intercalate into unit cell. Surprisingly, the unit cell slightly contracts along ***a*** direction, even though two hydronium ions are stored close to the body diagonal on (011) plane. This result can be explained by considering **Figure 7.4**, where the hydronium ion interacts with three carbonyl groups, two of which stacking in parallel along ***a*** direction are pulled closer by H_3O^+. Another unit cell parameter showing a prominent change after intercalation is β, expanding from original value of 96.00° to 103.56° when accommodating two H_3O^+, which is in a good agreement with $(10\bar{2})$ peak shift from XRD in **Figure 7.3** (b).

Table 7-1 Simulated PTCDA unit cell parameters.

	a (Å)	b(Å)	c (Å)	α (°)	β (°)	γ (°)	V (Å³)
Pristine	3.74	18.95	10.75	90.00	96.00	90.00	757.71
One H_3O^+	3.54	19.35	11.71	89.61	100.20	90.84	790.46
Two H_3O^+	3.46	19.64	12.33	88.22	103.56	92.01	813.01

We used Fourier Transform Infrared spectroscopy (FTIR) to investigate the possible bonding variation, particularly for the carbonyl groups in anhydrides upon hydronium intercalation. To understand the impact of ion intercalation on the chemical bonding,

we have compared spectra between the hydroniated PTCDA and potassiated PTCDA (**Figure 7.5)**.

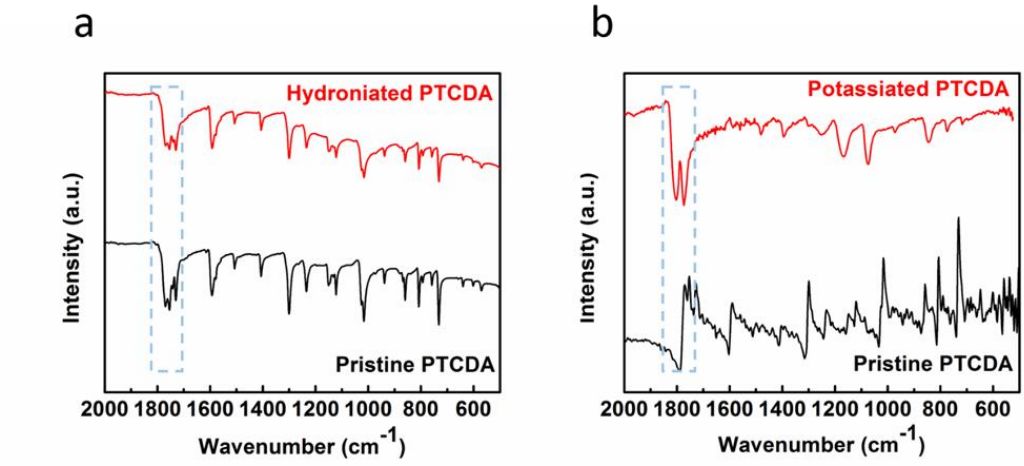

Figure 7.5 FTIR spectra of (a) hydroniated PTCDA electrode, and (b) potassiated PTCDA electrode.

In **Figure 7.5** (b), after potassiation, the peak at 1788 cm^{-1} assigned to carbonyl stretching shifts to 1773 cm^{-1}, indicating a weakened C=O double bond; a new peak at 1824 cm^{-1} is observed, which is attributed to the formation of potassium enolate groups. However, for hydronium intercalation, the peaks from 1730 to 1769 cm^{-1} only slightly diminish, suggesting that there are no new chemical bonds formed. The disparity between the hydroniation and potassiation in terms of the changes of chemical bonds in PTCDA is quite intriguing, and we postulate that proton is screened by the hydration, which weakens the enolation process, thus being different from the case with the "naked" K^+. Other than the slightly diminished anhydride peaks, all other peaks remain as the pristine PTCDA, indicating that the structure is perfectly preserved after cycling.

Peaks corresponding to C-O stretching (1300 cm^{-1}), vibrational bending mode of the ring (from 731 cm^{-1} to 938 cm^{-1})[56], ring stretching (at 1405.81, 1506.62 and 1592.53 cm^{-1})[56], and C-O+C-C stretching (at 1015.60 and 1121.16 cm^{-1})[56], all remain as the pristine PTCDA, indicating that the structure is perfectly preserved after hydronium intercalation.

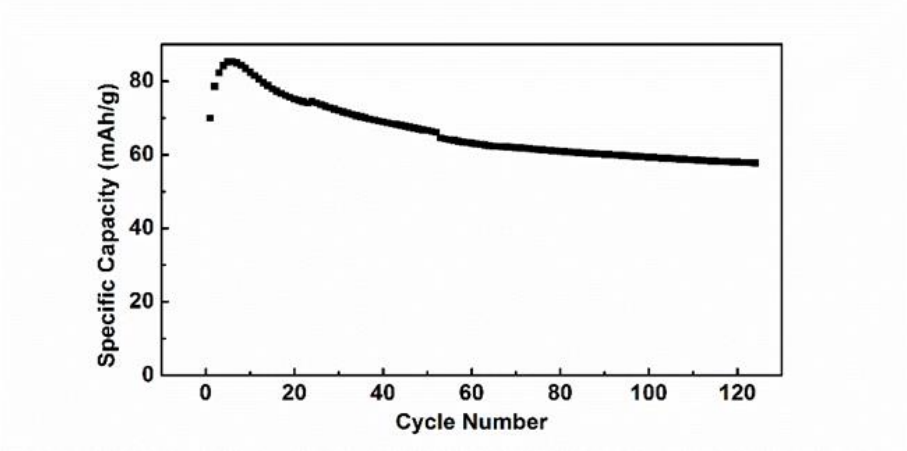

Figure 7.6 Galvanostatic cycling of PTCDA electrodes in 1 M H_2SO_4 at 1 A/g.

We tested the cycling stability of PTCDA, as shown in **Figure 7.6**, which is relatively stable. Indeed, PTCDA as an anhydride may encounter the challenge of hydration, thus forming the perylenetetracarboxylic acid. To investigate this matter, we soaked the pristine PTCDA electrode in the electrolyte of 1 M H_2SO_4 for 5 days, where the electrolyte did not change its color neither it fluoresces (**Figure 7.7** a). Note that if molecules with the pyrelene ring dissolve, the solution would fluoresce. However, the fact that the pristine PTCDA electrode does not dissolve cannot warrant that the reduced PTCDA would not dissolve. To further investigate this, we collected the

electrolyte from the cells after 120 cycles, where the electrolyte exhibits a brown color, as shown in the new **Figure 7.7** a, which indicates a certain level of solubility of the reduced PTCDA. Interestingly, the color of the electrolyte turned light green after the cycled electrolyte being left in air for 4 hours (**Figure 7.7** b). To further confirm that the light green color is from PTCDA, ultraviolet-visible (UV-Vis) spectrum was collected. As shown in **Figure 7.8**, the cycled electrolyte shows a broad absorption peak around 460 nm, being consistent with the two peaks at 438 and 467 nm from the standard PTCDA/KOH solution, confirming the presence of PTCDA in the electrolyte. Apparently, the reduced PTCDA could be more soluble.

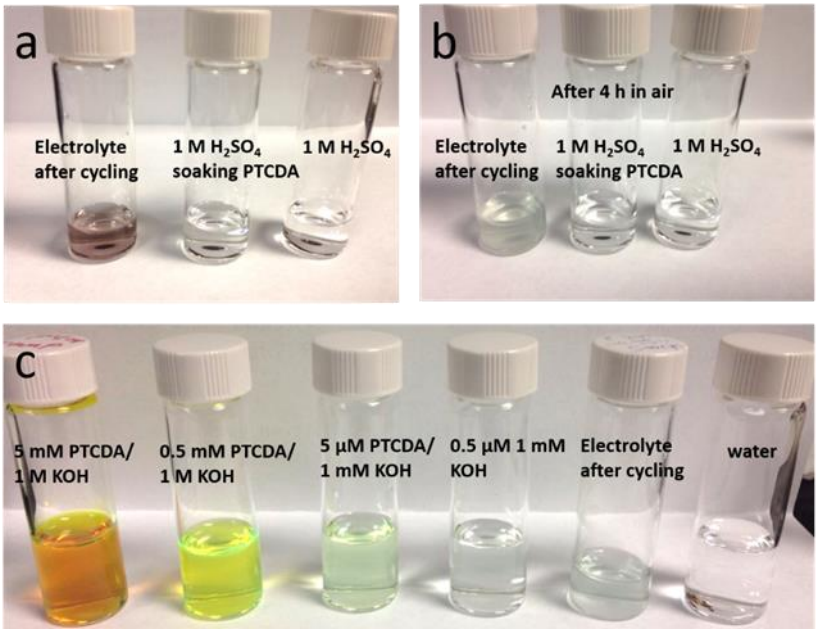

Figure 7.7 From left to right: (a), electrolyte after 120 cycles, electrolyte soaking PTCDA electrode for 5 days, fresh electrolyte (1 M H_2SO_4); (b), above three solutions stay in air for another 4 h; (c) electrolyte compared with various PTCDA stock solutions.

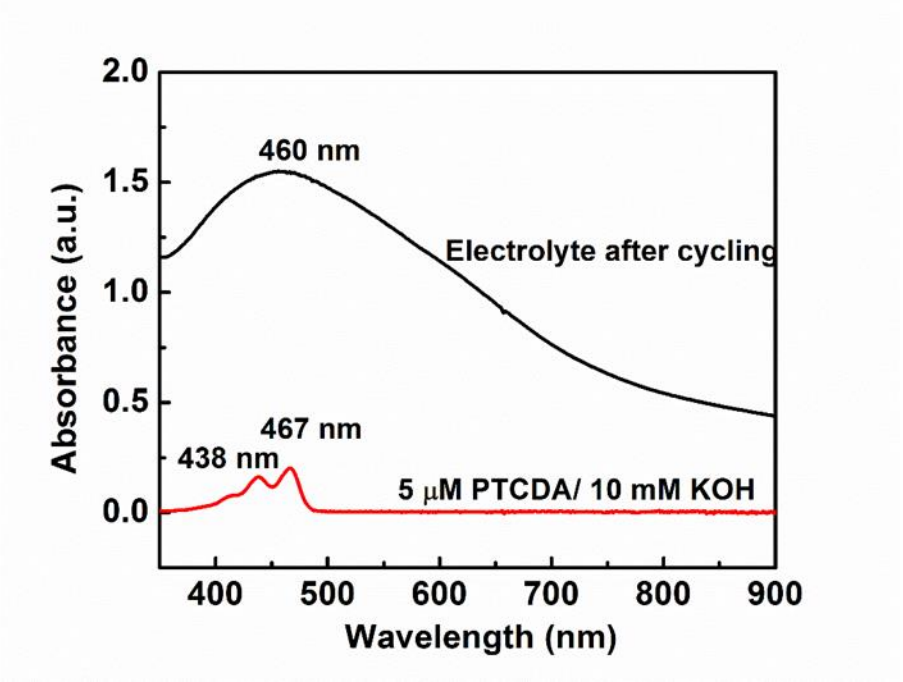

Figure 7.8 UV-Vis spectra of electrolyte after cycling (black) and 5 μM PTCDA with 10 mM KOH (red).

7.5 Conclusions

In summary, we report that hydronium ion can be electrochemically stored in PTCDA reversibly with a capacity of 85 mAh/g. The amenable redox reactivity of PTCDA in 1 M H_2SO_4 requires an initial conditioning process, as demonstrated by CV and galvanostatic charge/discharge cycles, where this process increases its specific capacity and lowers the polarization. *Ex situ* XRD reveals the reversible dilation of the PTCDA structure upon hydronium intercalation, which is supported by the first-principles DFT calculation. The calculation reveals the structural change of PTCDA upon hydronium

incorporation and the specific sites of the inserted hydronium ions in the PTCDA structure. We have demonstrated a proof-of-concept insertion electrode material for hydronium-ion batteries, which may potentially provide new solutions for energy storage.

8 Ambient Hydrolysis Deposition Enabling Nanoparticles Coated in Porous Substrate

8.1 Abstract

Despite the considerable advances of deposition technologies, it remains a significant challenge to form conformal deposition on surface of nanoporous carbons. Here, we introduce a new ambient hydrolysis deposition method that employs and controls pre-adsorbed water vapor on nanoporous carbons to define the deposition of TiO_2. We converted the deposited TiO_2 into TiN via a nitridation process. The metallic-TiN-coated porous carbon exhibits superior kinetic performance as an electrode in electrical double layer capacitors. The novel deposition method provides a general solution for surface engineering on nanostructured carbons, which may result in a strong impact on the fields of energy storage and other disciplines.

8.2 Introduction

Nanoporous materials are at the heart of important applications, such as energy storage, catalysis, sensing, drug delivery, and separation.[194-197] However, these materials often fall short on providing needed functionalities due to a lack of desirable surface properties. Despite the advances in deposition methods, it remains a significant challenge to form controllable conformal deposition inside nanoporous materials at ambient conditions. Vapor deposition methods, such as chemical vapor deposition (CVD), thermal deposition, or e-beam deposition, do not meet the requirements due to

their line-of-sight nature. Most conformal methods, such as electrodeposition,[198, 199] electroless deposition,[200, 201] and dip/spin coating,[202] provide no control at the scale of a few nanometers. As the state-of-the-art conformal deposition methods, atomic layer deposition (ALD)[203-205] and under potential deposition (UPD)[206, 207] have yet to demonstrate general applicability inside nanoporous materials.

Herein, we introduce a new ambient hydrolysis deposition (AHD) methodology for coating metal oxides on nanoporous carbons. The AHD involves water adsorption in porous substrates and a subsequent hydrolysis inside "wet" substrates via a dry non-aqueous solution of precursors. As schematically depicted in **Figure 8.1** A, the water adsorption step differentiates the AHD from the conventional sol-gel methods where water and hydrolysis precursors encounter porous substrates at the same time.[208-210] Water adsorption on activated carbons has been experimentally and theoretically studied although the related mechanism is still not well understood.[211-213] Unfortunately, this phenomenon has never been utilized for ambient deposition purposes. We, for the first time, demonstrate that the scale of ambient deposition of TiO_2 can be controlled by manipulating the water adsorption in nanoporous carbons. We also converted the TiO_2-deposited nanoporous carbon to TiN/carbon nanocomposite as an electrode for electrical double layer capacitors (EDLCs).

8.3 Experimental

CMK-3 was prepared by a nanocasting method following the well-established procedure in the literature by employing SBA-15 as a hard template.[214]

The AHD Process:

Step I: Surface functionalization

Typically, CMK-3, 0.3 g, was added to a freshly-prepared aqueous solution of $(NH_4)_2S_2O_8$, (1.0 M) and H_2SO_4, (2.0 M) (30 ml). The mixture was stirred at 60 °C for 6 hrs. Then, the oxidized CMK-3 (C-APS) was filtered, rinsed with deionized water and dried overnight in an oven at 80 ºC.

Step II: Water loading

Degassed C-APS, 50 mg, was loaded into a plastic syringe in a glovebox. The carbon-containing syringe was warmed up in an oven at 80 ºC before water loading to prevent water condensation on the syringe side wall and the external surface of C-APS particles. A narrow-mouth bottle of 500 ml volume that contains water 100 ml was heated in an oven at 80 ºC. We used the warmed-up carbon-containing syringe to take in a certain volume of water-vapor/air mixture for a desired amount of water loading. The needle of the syringe was sealed after water loading. Then, the syringe was shaken by a vortex mixer for 5 mins at 80°C in order to enable good contact of water vapor with C-APS before the syringe was kept in an oven at 60 ºC for half an hour. For the reference level of water loading, a vial containing C-APS was ‘soaked’ in water-vapor/air mixture in a larger narrow-mouth bottle that contained water in an oven at 80 ºC.

Step III: Hydrolysis deposition of TiO_2

Water-loaded C-APS samples were soaked for an hour in a dilute solution of titanium tetraisopropoxide (TTIP) in 1, 3-dioxolane (DOXL) (5 vol%). The product was collected by filtration in a glovebox. Samples were heated at 250 ºC under nitrogen before N_2 sorption measurements and nitridation.

Nitridation of C-TiO_2-100

Samples were heated in a tube furnace at 850 ºC for 6 hrs under NH_3 with a flow rate of 54 cc/min.

Formation of activated carbon

Carbon microfiber of 2 g (Osaka Gas Co., Ltd) was heated in quartz tube furnace at 910 ºC under CO_2 with a flow rate of 100 ml/min for 18 hrs.

Boehm titration procedure

The amount of surface functional groups was determined using Boehm titration. In Boehm titration, the following assumptions were made to distinguish between the carbon–oxygen functionalities based on their acidity: NaOH is the strongest base and it neutralizes all Brønsted acids, including phenols, lactonic and carboxylic groups, while $NaCO_3$ neutralizes carboxylic and lactonic groups and $NaHCO_3$ neutralizes only carboxylic acid groups. Briefly, C-APS, 0.2 g, was dispersed in 20 ml of 0.05 M

$NaHCO_3$ solution and the mixture was stirred for 48 hrs. The solution was then allowed to remain quiescent for 24 hrs. The aliquot (neutralized with 0.05 M conc. HCl) of 5 ml was back titrated against standardized NaOH solution using phenolphthalein as indicator.

Characterization methods:

X-Ray diffraction (XRD) patterns were collected using a Rigaku Ultima IV Diffractometer with Cu Kα irradiation (λ= 1.5406 Å). Nitrogen sorption measurements were performed on a Micromeritics TriStar II 3020 analyzer at 77.4 K. The samples were outgassed at 250 ºC under N_2 for 12 hrs prior to the N_2 sorption measurements. X-ray Photoelectron Spectroscopy (XPS) measurements were performed in a Physical Electrons Quantera Scanning ESCA Microprobe with a focused monochromatic Al Kα X-ray (1486.6 eV) source for excitation. The X-ray beam used was a 25 W, 100 μm X-ray beam spot at the sample. The binding energy (BE) scale was calibrated using the Cu $2p_{3/2}$ feature at 932.62 ± 0.05 eV and Au 4f at 83.96 ± 0.05 eV. The ion gun used in this system was a standard Quantera ion gun, and the sputter depth profiles were acquired using a 1 KeV argon-ion beam rastered over a 3 mm x 3 mm area. To minimize charging artifacts, the XPS data were collected with 1 eV, 20 μA electrons and low-energy Ar^+ ions. The morphology was examined by field emission scanning electron microscopy (FESEM) using an FEI NOVA 230 high resolution SEM with an energy-dispersive X-ray (EDX) attachment. Transmission electron microscopy (TEM) and high-resolution transmission electron microscopy (HRTEM) images were recorded by

an FEI Titan 80-300 TEM. High angle annular dark field scanning TEM (HAADF-STEM) measurements were carried out on an FEI Titan 80-200 microscope coupled with a HAADF detector and an EDX spectrometer.

Electrochemical Measurements:

A two-electrode cell configuration was used to measure the electrochemical performance of samples. Electrodes were composed of 90 wt% active mass and 10 wt% poly(vinylidene fluoride) binder. The materials were slurry-cast from a cyclopentanone suspension onto a carbon-fiber paper current collector (Model: 2050A). The electrodes were dried at 120 ºC under vacuum for 12 hrs and then cut into 10 mm disks. The active mass loadings are ~1 mg/cm^2. Then, two identical (by weight and size) electrodes were assembled in coin-type cells that use polypropylene films as the separator and a CH_3CN solution of 1.0 M ammonium tetrafluoroborate (NH_4BF_4) as the electrolyte. Cyclic voltammetry (CV), galvanostatic charge/discharge, and EIS were carried out on a VMP-3 multi-channel workstation at room temperature. CV and charge/discharge profiles were collected in a voltage window from 0 to 2.5 V. EIS was carried out with the potential amplitude of 10 mV at the frequency range of 200 kHz to 10 mHz. The voltage drop at the beginning of discharge (V_{drop}) is used to estimate the equivalent series resistance, R_{ESR}, at a constant current of I with the formula of $R_{ESR} = V_{drop}/(2I)$.

We chose CMK-3, a mesoporous carbon with a long-range ordered nanostructure (symmetry: *P6mm*), as the model nanoporous carbon.[215] For the deposition

composition, we selected TiO_2 in this proof-of-concept study. In the first step of AHD, in order to increase the surface hydrophilicity for facile water vapor adsorption, CMK-3 is functionalized with carboxylic groups in a warm acidic ammonium persulfate (APS) solution. The obtained carbon is designated as C-APS. The number of carboxylic groups on C-APS was measured by Boehm titration to be 1.96 mmol/g. For water loading, we first exposed degassed C-APS to excessive saturation water vapor (80 ºC) for one hour, and the adsorbed water was determined by thermogravimetric analysis (TGA) to be 16 wt%, as a reference. Then, a certain volume of saturation water vapor (80 ºC) was measured by a syringe and exposed to the degassed C-APS contained in the same syringe.

8.4 Results and Discussion

By exposing C-APS to the water vapor volumes corresponding to molar ratios of 133%, 100%, 67%, and 33% of the reference water loading (16 wt%), 7.5 wt%, 7 wt%, 6 wt%, and 4 wt% of water were adsorbed, as revealed by the TGA results (**Figure 8.1** B**)**. These water-loaded carbons are referred to as C-133, C-100, C-67, and C-33, correspondingly. The results demonstrate that water loading in nanoporous carbon can be controlled, which constitutes the foundation for the controllable AHD method. In the following step, water-loaded C-APS samples were soaked in the 1,3 dioxolane (DOXL) solution of titanium tetraisopropoxide (TTIP) (5 vol%) in an Argon-filled glovebox. The composites were collected by filtration and dried in an oven.

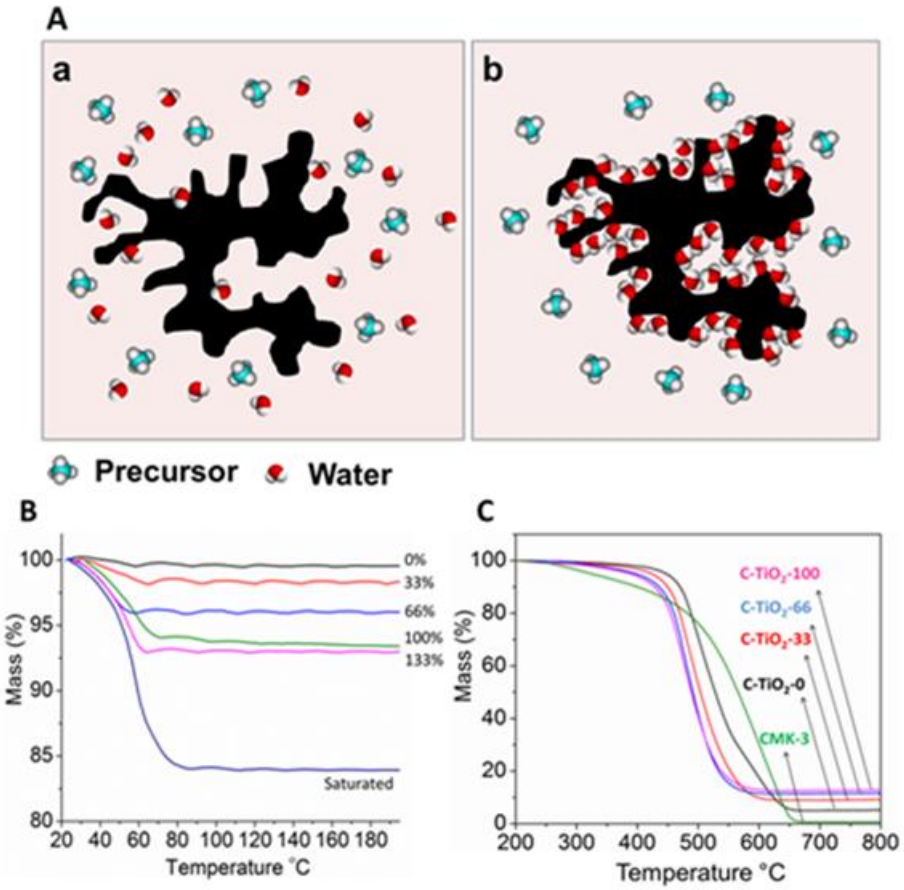

Figure 8.1 Schematic showing the different water distribution between a) conventional sol-gel method and b) AHD method. B) TGA curves of C-APS with different levels of water loading. C) TGA curves of C-TiO2 samples showing different levels of TiO2 loading corresponding to water adsorption.

It is necessary to mark the minimum scale of deposition that is determined by the water from the DOXL solution of TTIP. Degassed C-APS was soaked in the precursor solution, and 5.2 wt% of TiO_2 was loaded. Note that CMK-3 is nearly ash free. The obtained TiO_2/C nanocomposite is referred to as C-TiO_2-0, where "0" indicates that no water is pre-adsorbed (**Figure 8.1** C). With C-33, C-66 and C-100 as the substrates, the TiO_2 loadings were 9.1 wt%, 11.3 wt%, and 12.6 wt%, respectively (**Figure 8.1** C and **Table 8-1**).

Table 8-1 Physical characteristics of the samples.

Samples	TiO_2 (wt%)	Surface area (m^2/g)	Pore volume (cc/g)	Microporous	
				Surface area (m^2/g)	Pore volume (cc/g)
CMK-3	N.A	1233	1.59	176	0.08
C-APS	N.A	970	1.39	109	0.04
C-TiO_2-0	5.2	792	1.09	184	0.09
C-TiO_2-33	9.1	780	1.00	73	0.03
C-TiO_2-67	11.3	757	0.94	62	0.02
C-TiO_2-100	12.6	729	0.90	75	0.03
C-Ti-N	N.A	1078	1.21	188	0.08

We investigated the deposition uniformity of the AHD method by looking at C-TiO_2-100 as the representative material. It is evident that C-TiO_2-100 maintains a long-range ordered nanostructure comparable to that of C-APS, as revealed by the high-angle angular dark field scanning TEM image (HAADF-STEM).

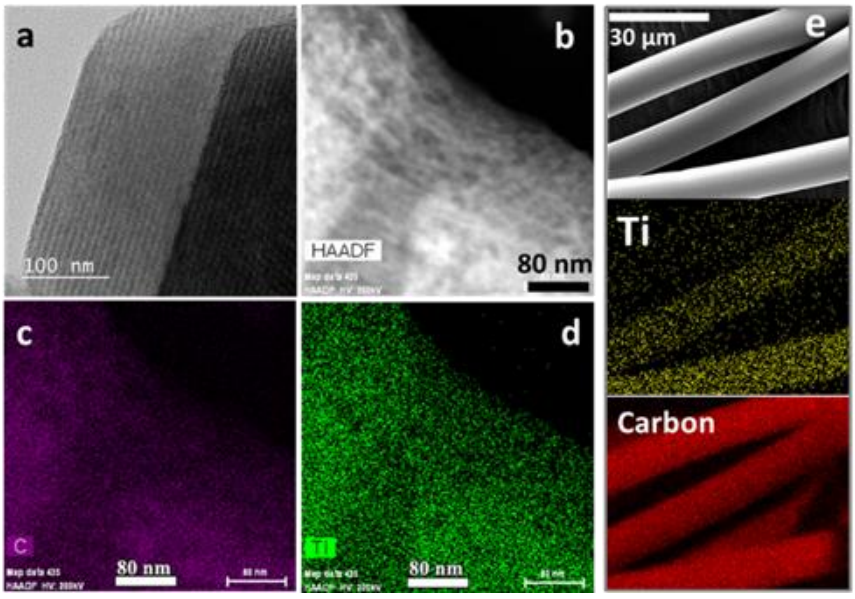

Figure 8.2 Electron microscopy studies of C-APS and C-TiO_2-100. a) A bright-field TEM image of C-APS. b) An HAADF-STEM image of C-TiO_2-100. c,d) Carbon and titanium

EDX mappings corresponding to the image in b. e) A SEM image of activated carbon, and the corresponding carbon and titanium EDX mappings.

More importantly, TiO_2 phase is uniformly distributed in the nanocomposite, as suggested by the corresponding titanium elemental mapping (**Figure 8.2** a,b,d). Note that HAADF-STEM is sensitive to the contrast of electron densities from different elements, which helps estimate the particle size of deposited TiO_2 in the carbon matrix. The absence of noticeable TiO_2 nanoparticles in the image demonstrates that the deposited TiO_2 particles are likely of subnanometer sizes.

It has been a long-standing challenge to impregnate microporous carbons with an oxide deposition. With same AHD method, we successfully deposited TiO_2 in an activated carbon that exhibits a high surface area of 2715 m^2/g and an average pore size around 2.3 nm. A representative SEM image with the corresponding titanium EDX mapping reveals the homogeneous TiO_2 deposition (**Figure 8.2** e). The activated carbon was prepared by activating a commercially available coal-derived carbon by CO_2 oxidation.

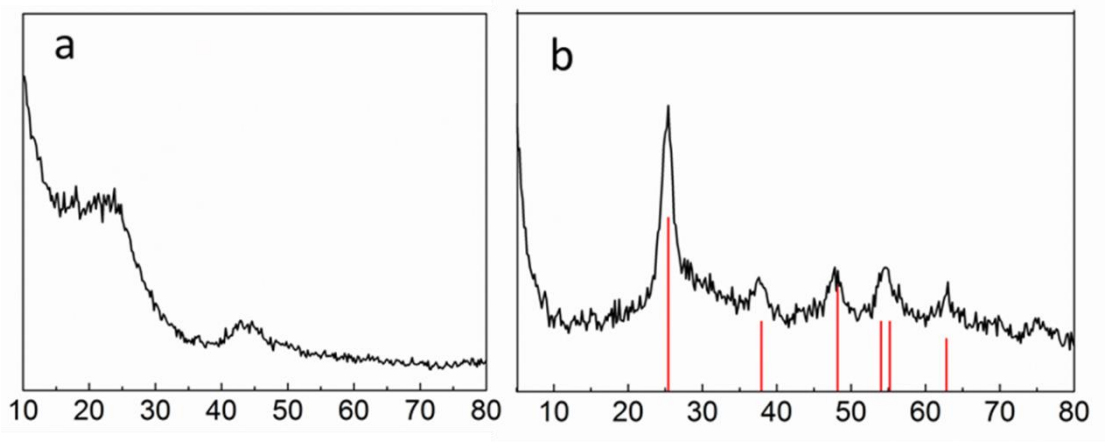

Figure 8.3 XRD patterns of a) C-TiO2-100 and b) bulk TiO2 powder.

The wide-angle X-ray diffraction (XRD) pattern of C–TiO_2-100 with no crystalline features confirms the small TiO_2 particle sizes observed by TEM (**Figure 8.3**).

From **Table 8-1** and **Figure 8.4**, it is evident that the functionalization of carboxylic groups does affect the CMK-3 nanostructure. After the TiO_2 deposition, the specific surface area and pore volume, particularly, the micropore characteristics were further diminished. The pore size distribution (PSD) of the C-TiO_2 samples slightly shifts to larger values, compared to that of C-APS (Fig. 3b). This indicates that the deposition primarily occurs in smaller mesopores or micropores in water-adsorbed C-APS.

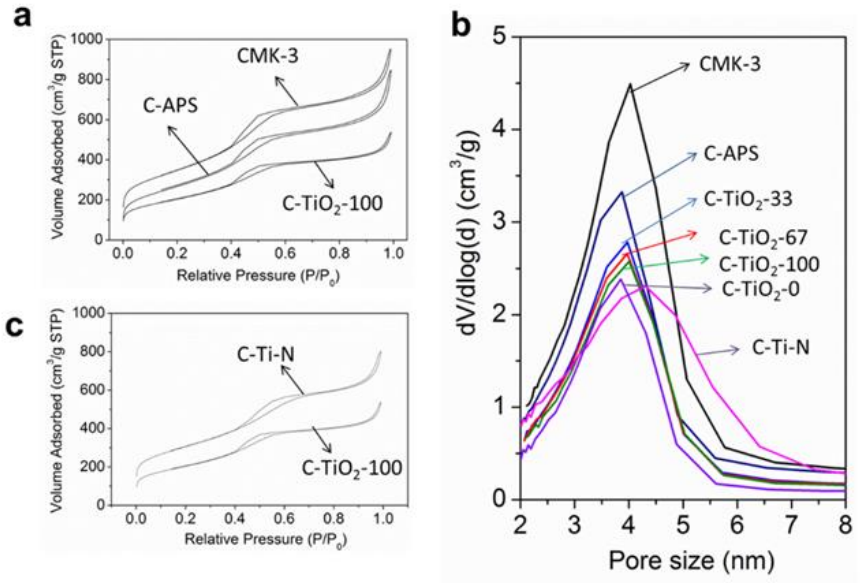

Figure 8.4 a) N_2 sorption isotherms of CMK-3, C-APS and C-TiO_2-100. b) Pore size distributions of different samples. c) Isotherms of C-TiO_2-100 and C-TiN.

As known, water vapor is preferably adsorbed in smaller pores.[211] In sharp contrast, the micropore features of C-TiO_2-0 were doubled after deposition, which suggests that the hydrolysis deposition in this case turned large mesopores into micropores. For C-TiO_2-0, hydrolysis water mainly comes from the precursor solution, and it is unfavorable for liquid water to reach smaller pores.

We have demonstrated that the AHD method enables ambient conformal deposition of TiO_2 in nanoporous carbons. A great advantage of oxide deposition is that oxides can be potentially turned to other compositions by chemical reactions. We chose to convert TiO_2 coating into TiN in C-APS as an electrode for enhanced rate performance in EDLCs. EDLCs operate on electrostatic interaction between polarized amorphous carbon surface and solvated ions.[121, 122, 216, 217] The low conductivity of amorphous carbon limits the kinetic performance of EDLCs. Thus, graphitic innovative carbons, such as graphene-based electrodes,[10, 98, 134, 218] have been investigated, demonstrating much improved power performance in EDLCs. Another approach is to improve the surface conductivity of carbon electrodes, and N-doping shows some effect.[141, 219-221] We chose to form a TiN layer on porous carbon surface due to its high electrical conductivity (5×10^6 S/m), two orders higher than theoretical graphene, and good corrosion resistance.[222-225] C-TiO_2-100, as the model composite, was annealed at 850 ºC under NH_3 for 6 hrs. We referred to the obtained composite as C-TiN. The XRD pattern of C-TiN depicts a single cubic phase of TiN (JCPDS 38-1420), and confirms the absence of crystalline TiO_2 and TiON (**Figure 8.5** a). The XRD pattern indicates a

complete nitridation because any remained TiO_2 or TiON would be crystallized at 850 °C and display crystalline peaks. The TiN coherence length is estimated by the Scherrer Equation to be 4.0 nm from the XRD peaks.

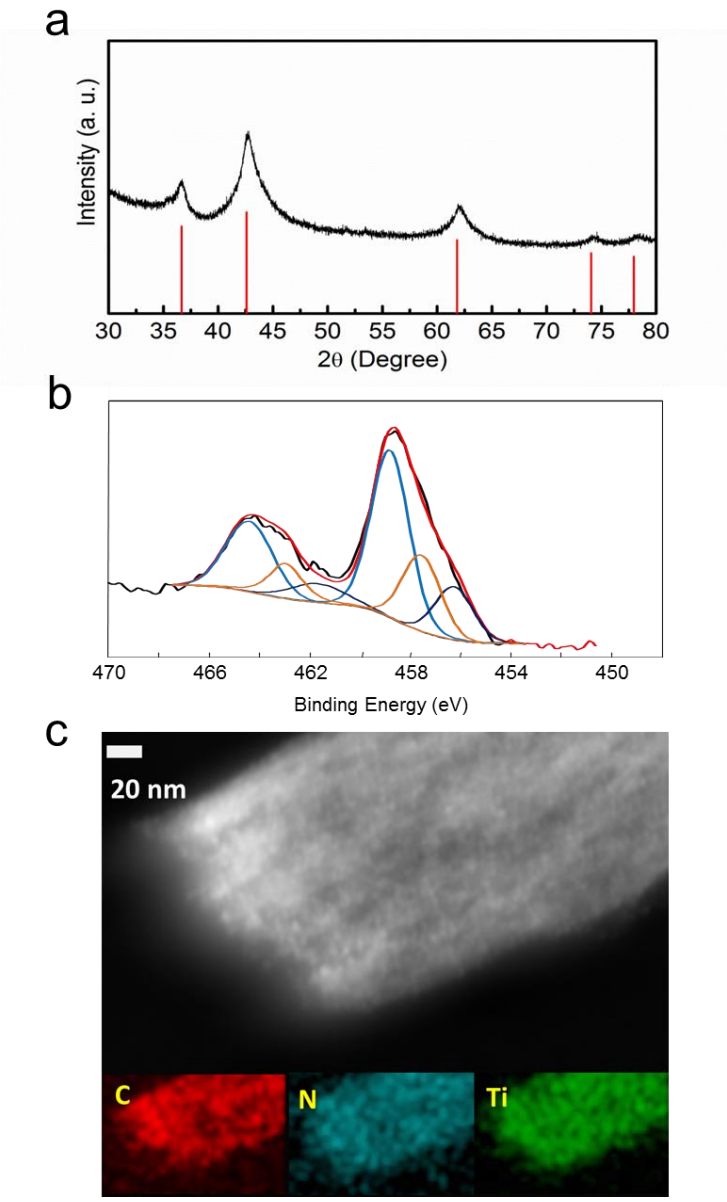

Figure 8.5 Compositional and structural characterizations of C-TiN. a) XRD pattern. b) XPS Ti [2p] signal. c) HAADF-STEM and carbon, nitrogen and titanium EDX mappings. The results reveal that TiN nanocrystallites are homogenously dispersed in C-APS.

To further identify the chemical compositions, we conducted X-ray photoelectron spectroscopy (XPS). The Ti $2p_{3/2}$ peak of C-TiN can be deconvoluted into three components at 456.3 eV (TiN), 457.6 eV (TiON), and 458.8 eV (TiO_2) (**Figure 8.5** b). The combined XRD and XPS results suggest that the amorphous TiO_2 and TiON phases were inevitably formed during the sample handling.[22638] The contribution of TiO_2 and TiON is certainly overestimated by XPS due to their overwhelming presence at particle surface. We further studied the structure of C-TiN by HAADF-STEM and the corresponding titanium EDX mapping, as shown in **Figure 8.5** c. The HAADF-TEM image depicts the well-maintained nanostructure of CMK-3 with finely-dispersed nanoparticles. The observed particle size is around 4 to 6 nm, which corroborates the coherence length estimated based on the XRD peaks. As **Table 8-1** summarizes, the porosity characteristics of C-TiN are larger than those of C-TiO_2-100. Particularly, the specific pore volume and surface area of micropores were dramatically increased after nitridation, compared to C-TiO_2-100. As shown in **Figure 8.4** c, the isotherm hysteresis of C-TiN shifts to a higher relative pressure (P/P_0) after nitridation, compared to C-TiO_2-100. The PSD peak of C-TiN shifts to 4.3 nm from 3.9 nm, as shown in Fig. 3b. This may be caused by the TiN nanoparticle formation process at the expense of TiO_2 clusters that migrated out of the micropores. Note that the micropore surface area of C-TiN is even larger than C-APS. It seems that there might be a carbon oxidation/activation phenomenon during the nitridation process.

We compared the electrochemical performances of C-TiN and pristine CMK-3 as EDLC electrodes. A control sample, referred to as CMK-N, was prepared by the nitridation of C-APS, and it contains nitrogen of ~3 at%, determined by EDX. Cyclic voltammetry (CV) measurements were conducted at different scanning rates of 50, 100, 200, and 500 mV/s. As **Figure 8.6** (a) shows, C-TiN maintains the rectangular shape very well in its CV curves even at 500 mV/s, and area enclosed in CV curves dos not shrink much upon higher scanning rates. In sharp contrast, the CV curves of CMK-3 are almost flattened upon high scanning rates (**Figure 8.6** b), and similar CV results were observed for CMK-N, as shown in **Figure 8.6** (c) shows the galvanostatic charge and discharge profiles of CMK-3 and C-Ti-N at different current rates. The two materials exhibit similar capacitance values but vastly different equivalent series resistance (ESR). For example, at the current rate of 0.5 A/g, the ESR is 21.9 Ω and 118 Ω for C-TiN and CMK-3, respectively. **Figure 8.6** (d) shows the Nyquist plots obtained at the frequency range from 200 kHz to 10 mHz, where C-TiN exhibits a smaller semicircle compared to CMK-3 (1 Ω vs. 2 Ω), indicating a lower electrode/electrolyte interface resistance for C-TiN than CMK-3. The high ohmic resistance of C-TiN may be due to the oxidation process in forming C-APS. It has been clearly demonstrated that the TiN coating significantly improves the kinetic response of the electrode although some TiO_2 and TiON phases are formed on the surface of TiN nanocrystallites, and the rate improvement is certainly not from the N-doping effect.

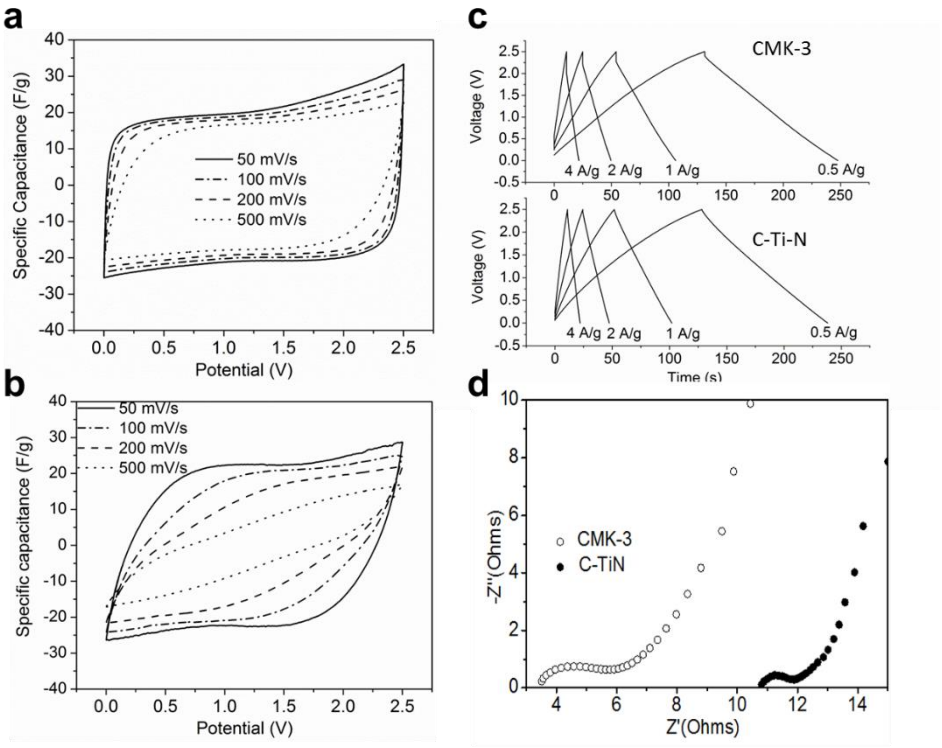

Figure 8.6 (a,b) CV curves at different scanning rates for C-TiN and CMK-3, respectively. (c) Galvanostatic charge/discharge profiles at different current densities of CMK-3 and C-TiN electrodes. (d) Nyquist plots of C-TiN and CMK-3 electrodes.

8.5 Conclusions

we have demonstrated a new ambient hydrolysis deposition methodology to coat TiO_2 onto nanoporous carbons. The novel approach can tune the hydrolysis scales by varying the levels of pre-adsorbed water inside the porous carbon. To the best of our knowledge, this is the first ambient deposition method for nanoporous materials. It is potentially scalable due to its simplicity and low cost. Furthermore, we converted deposited TiO_2 into TiN nanocrystallites on the carbon surface by an NH_3-based nitridation process to improve the surface conductivity of the nanoporous carbon electrodes in EDLCs. The

TiN phase greatly improves rate performance, which unequivocally demonstrates that metallizing surface of amorphous carbon electrodes is a viable approach for enhanced EDLCs.

9 Future Work

Although significant research has been conducted to increase the energy density of ECs, some of it works at the expense of lowering power and shortening cycle life significantly, producing mediocre batteries rather than high performance ECs. Hybrid capacitors may be a solution for energy dense ECs, which incorporate a battery-type electrode and a capacitor-type electrode. However, not all battery electrodes are viable in hybrid capacitors. Only those electrode materials with fast reaction kinetics and stable structures upon charge/discharge may work well in hybrid capacitors, not only storing more energy, but also performing high power and long cycle life, which differentiate capacitors from batteries.

Aqueous batteries may deliver high power and provide long cycle life, because of the potentially high ionic conductivity and no active material consumption due to solid electrolyte interface. In hydronium-ion batteries, because H_3O^+ has similar ionic radius as Na^+, electrode materials storing Na^+ may successfully accommodate H_3O^+, as long as the potential is within electrochemical window of aqueous electrolyte. Moreover, high-rate Na^+ electrodes are of particular interest to enable high power in aqueous electrolyte. Electrode dissolution harms the cycle life of batteries, which is a problem for some materials, especially in acidic electrolyte. This may be addressed by utilizing mixed electrolytes with weak acid and supporting electrolytes, which provide hydronium ions and high conductivity, respectively.

High ionic conductivity in acidic aqueous electrolyte can be explained by Grotthuss mechanism. It would be interesting to study this mechanism in organic electrolytes. Organic solvent molecules forming hydrogen bonding may experience similar proton conducting process as in aqueous electrolyte. If Grotthuss mechanism is proved to be viable in organic electrolyte, it may provide higher ionic conductivity, and lead to an evolution of ECs with enhanced power.

Bibliography

1. International Energy Outlook 2016 with Projections to 2040. www.eia.gov/forecasts/ieo.

2. The Future Arrives for Five Clean Energy Technologies – 2016 Update.

3. Marchant, W. H., *Wireless Telegraphy: A Handbook for the Use of Operators and Students*. Whittaker: 1914.

4. Zhang, L. L.; Zhao, X. S., Carbon-Based Materials as Supercapacitor Electrodes. *Chem. Soc. Rev.* **2009,** *38* (9), 2520-2531.

5. Conway, B. E., *Electrochemical Supercapacitors: Scientific Fundamentals and Technological Applications*. Kluwer Academic/Plenum Publishers: 1999.

6. Wang, G. P.; Zhang, L.; Zhang, J. J., A Review of Electrode Materials for Electrochemical Supercapacitors. *Chem. Soc. Rev.* **2012,** *41* (2), 797-828.

7. Salitra, G.; Soffer, A.; Eliad, L.; Cohen, Y.; Aurbach, D., Carbon Electrodes for Double-Layer Capacitors - I. Relations between Ion and Pore Dimensions. *J. Electrochem. Soc.* **2000,** *147* (7), 2486-2493.

8. Largeot, C.; Portet, C.; Chmiola, J.; Taberna, P. L.; Gogotsi, Y.; Simon, P., Relation between the Ion Size and Pore Size for an Electric Double-Layer Capacitor. *J. Am. Chem. Soc.* **2008,** *130* (9), 2730-+.

9. Chmiola, J.; Yushin, G.; Gogotsi, Y.; Portet, C.; Simon, P.; Taberna, P. L., Anomalous Increase in Carbon Capacitance at Pore Sizes Less Than 1 Nanometer. *Science* **2006,** *313* (5794), 1760-1763.

10. El-Kady, M. F.; Strong, V.; Dubin, S.; Kaner, R. B., Laser Scribing of High-Performance and Flexible Graphene-Based Electrochemical Capacitors. *Science* **2012,** *335* (6074), 1326-1330.

11. Niu, C. M.; Sichel, E. K.; Hoch, R.; Moy, D.; Tennent, H., High Power Electrochemical Capacitors Based on Carbon Nanotube Electrodes. *Appl. Phys. Lett.* **1997,** *70* (11), 1480-1482.

12. Wang, D. W.; Li, F.; Liu, M.; Lu, G. Q.; Cheng, H. M., 3d Aperiodic Hierarchical Porous Graphitic Carbon Material for High-Rate Electrochemical Capacitive Energy Storage. *Angew Chem Int Edit* **2008,** *47* (2), 373-376.

13. Tuckerman, M. E.; Marx, D.; Parrinello, M., The Nature and Transport Mechanism of Hydrated Hydroxide Ions in Aqueous Solution. *Nature* **2002,** *417* (6892), 925-929.

14. Balducci, A.; Dugas, R.; Taberna, P. L.; Simon, P.; Plee, D.; Mastragostino, M.; Passerini, S., High Temperature Carbon-Carbon Supercapacitor Using Ionic Liquid as Electrolyte. *J. Power Sources* **2007,** *165* (2), 922-927.

15. Zheng, J. P.; Jow, T. R., High Energy and High Power Density Electrochemical Capacitors. *J. Power Sources* **1996,** *62* (2), 155-159.

16. Ghodbane, O.; Pascal, J. L.; Favier, F., Microstructural Effects on Charge-Storage Properties in Mno2-Based Electrochemical Supercapacitors. *Acs Appl Mater Inter* **2009,** *1* (5), 1130-1139.

17. Lukatskaya, M. R.; Dunn, B.; Gogotsi, Y., Multidimensional Materials and Device Architectures for Future Hybrid Energy Storage. *Nat. Commun.* **2016,** *7*.

18. Lin, T. Q.; Chen, I. W.; Liu, F. X.; Yang, C. Y.; Bi, H.; Xu, F. F.; Huang, F. Q., Nitrogen-Doped Mesoporous Carbon of Extraordinary Capacitance for Electrochemical Energy Storage. *Science* **2015,** *350* (6267), 1508-1513.

19. Wang, D. W.; Li, F.; Chen, Z. G.; Lu, G. Q.; Cheng, H. M., Synthesis and Electrochemical Property of Boron-Doped Mesoporous Carbon in Supercapacitor. *Chem. Mater.* **2008,** *20* (22), 7195-7200.

20. Chen, L. F.; Huang, Z. H.; Liang, H. W.; Gao, H. L.; Yu, S. H., Three-Dimensional Heteroatom-Doped Carbon Nanofiber Networks Derived from Bacterial Cellulose for Supercapacitors. *Adv. Funct. Mater.* **2014,** *24* (32), 5104-5111.

21. Guo, H. L.; Gao, Q. M., Boron and Nitrogen Co-Doped Porous Carbon and Its Enhanced Properties as Supercapacitor. *J. Power Sources* **2009,** *186* (2), 551-556.

22. Li, H. L.; Wang, J. X.; Chu, Q. X.; Wang, Z.; Zhang, F. B.; Wang, S. C., Theoretical and Experimental Specific Capacitance of Polyaniline in Sulfuric Acid. *J. Power Sources* **2009,** *190* (2), 578-586.

23. Whittingham, M. S., Electrical Energy-Storage and Intercalation Chemistry. *Science* **1976,** *192* (4244), 1126-1127.

24. Yazami, R.; Touzain, P., A Reversible Graphite Lithium Negative Electrode for Electrochemical Generators. *J. Power Sources* **1983,** *9* (3-4), 365-371.

25. Goodenough, J. B.; Park, K. S., The Li-Ion Rechargeable Battery: A Perspective. *J. Am. Chem. Soc.* **2013,** *135* (4), 1167-1176.

26. Tarascon, J. M., Key Challenges in Future Li-Battery Research. *Philos T R Soc A* **2010,** *368* (1923), 3227-3241.

27. Trends in Lithium Project Transactions.

28. Slater, M. D.; Kim, D.; Lee, E.; Johnson, C. S., Sodium-Ion Batteries. *Adv. Funct. Mater.* **2013,** *23* (8), 947-958.

29. Li, Z. F.; Jian, Z. L.; Wang, X. F.; Rodriguez-Perez, I. A.; Bommier, C.; Ji, X. L., Hard Carbon Anodes of Sodium-Ion Batteries: Undervalued Rate Capability. *Chem. Commun.* **2017,** *53* (17), 2610-2613.

30. Bommier, C.; Surta, T. W.; Dolgos, M.; Ji, X. L., New Mechanistic Insights on Na-Ion Storage in Nongraphitizable Carbon. *Nano Lett.* **2015,** *15* (9), 5888-5892.

31. Lotfabad, E. M.; Ding, J.; Cui, K.; Kohandehghan, A.; Kalisvaart, W. P.; Hazelton, M.; Mitlin, D., High-Density Sodium and Lithium Ion Battery Anodes from Banana Peels. *ACS Nano* **2014,** *8* (7), 7115-7129.

32. Li, Z. F.; Ma, L.; Surta, T. W.; Bommierit, C.; Jian, Z. L.; Xing, Z. Y.; Stickle, W. F.; Dolgos, M.; Amine, K.; Lu, J.; Wu, T. P.; Ji, X. L., High Capacity of Hard Carbon Anode in Na-Ion Batteries Unlocked by Pox Doping. *Acs Energy Letters* **2016,** *1* (2), 395-401.

33. Senguttuvan, P.; Rousse, G.; Seznec, V.; Tarascon, J. M.; Palacin, M. R., Na2ti3o7: Lowest Voltage Ever Reported Oxide Insertion Electrode for Sodium Ion Batteries. *Chem. Mater.* **2011,** *23* (18), 4109-4111.

34. Xiao, L. F.; Cao, Y. L.; Xiao, J.; Wang, W.; Kovarik, L.; Nie, Z. M.; Liu, J., High Capacity, Reversible Alloying Reactions in Snsb/C Nanocomposites for Na-Ion Battery Applications. *Chem. Commun.* **2012,** *48* (27), 3321-3323.

35. Yabuuchi, N.; Kubota, K.; Dahbi, M.; Komaba, S., Research Development on Sodium-Ion Batteries. *Chem. Rev.* **2014,** *114* (23), 11636-11682.

36. Jian, Z. L.; Luo, W.; Ji, X. L., Carbon Electrodes for K-Ion Batteries. *J. Am. Chem. Soc.* **2015,** *137* (36), 11566-11569.

37. Jian, Z. L.; Xing, Z. Y.; Bommier, C.; Li, Z. F.; Ji, X. L., Hard Carbon Microspheres: Potassium-Ion Anode Versus Sodium-Ion Anode. *Adv Energy Mater* **2016,** *6* (3).

38. Jian, Z. L.; Hwang, S.; Li, Z. F.; Hernandez, A. S.; Wang, X. F.; Xing, Z. Y.; Su, D.; Ji, X. L., Hard-Soft Composite Carbon as a Long-Cycling and High-Rate Anode for Potassium-Ion Batteries. *Adv. Funct. Mater.* **2017,** *27* (26).

39. Share, K.; Cohn, A. P.; Carter, R.; Rogers, B.; Pint, C. L., Role of Nitrogen-Doped Graphene for Improved High-Capacity Potassium Ion Battery Anodes. *ACS Nano* **2016,** *10* (10), 9738-9744.

40. Ma, G. Y.; Huang, K. S.; Ma, J. S.; Ju, Z. C.; Xing, Z.; Zhuang, Q. C., Phosphorus and Oxygen Dual-Doped Graphene as Superior Anode Material for Room-Temperature Potassium-Ion Batteries. *J. Mater. Chem. A* **2017,** *5* (17), 7854-7861.

41. Zhao, Q.; Wang, J. B.; Lu, Y.; Li, Y. X.; Liang, G. X.; Chen, J., Oxocarbon Salts for Fast Rechargeable Batteries. *Angew Chem Int Edit* **2016,** *55* (40), 12528-12532.

42. Deng, Q. J.; Pei, J. F.; Fan, C.; Ma, J.; Cao, B.; Li, C.; Jin, Y. D.; Wang, L. P.; Li, J. Z., Potassium Salts of Para-Aromatic Dicarboxylates as the Highly Efficient Organic Anodes for Low-Cost K-Ion Batteries. *Nano Energy* **2017,** *33*, 350-355.

43. Han, J.; Xu, M. W.; Niu, Y. B.; Li, G. N.; Wang, M. Q.; Zhang, Y.; Jia, M.; Li, C. M., Exploration of K2ti8o17 as an Anode Material for Potassium-Ion Batteries. *Chem. Commun.* **2016,** *52* (75), 11274-11276.

44. Kishore, B.; Venkatesh, G.; Munichandraiah, N., K2ti4o9: A Promising Anode Material for Potassium Ion Batteries. *J. Electrochem. Soc.* **2016,** *163* (13), A2551-A2554.

45. Wu, X. Y.; Leonard, D. P.; Ji, X. L., Emerging Non-Aqueous Potassium-Ion Batteries: Challenges and Opportunities. *Chem. Mater.* **2017,** *29* (12), 5031-5042.

46. Crumbliss, A. L.; Lugg, P. S.; Morosoff, N., Alkali-Metal Cation Effects in a Prussian Blue Surface-Modified Electrode. *Inorg. Chem.* **1984,** *23* (26), 4701-4708.

47. Wessells, C. D.; Peddada, S. V.; Huggins, R. A.; Cui, Y., Nickel Hexacyanoferrate Nanoparticle Electrodes for Aqueous Sodium and Potassium Ion Batteries. *Nano Lett.* **2011,** *11* (12), 5421-5425.

48. Xue, L. G.; Li, Y. T.; Gao, H. C.; Zhou, W. D.; Lu, X. J.; Kaveevivitchai, W.; Manthiram, A.; Goodenough, J. B., Low-Cost High-Energy Potassium Cathode. *J. Am. Chem. Soc.* **2017,** *139* (6), 2164-2167.

49. Bie, X. F.; Kubota, K.; Hosaka, T.; Chihara, K.; Komaba, S., A Novel K-Ion Battery: Hexacyanoferrate(Ii)/Graphite Cell. *J. Mater. Chem. A* **2017,** *5* (9), 4325-4330.

50. Wu, X. Y.; Jian, Z. L.; Li, Z. F.; Ji, X. L., Prussian White Analogues as Promising Cathode for Non-Aqueous Potassium-Ion Batteries. *Electrochem. Commun.* **2017,** *77*, 54-57.

51. He, G.; Nazar, L. F., Crystallite Size Control of Prussian White Analogues for Nonaqueous Potassium-Ion Batteries. *Acs Energy Letters* **2017,** *2* (5), 1122-1127.

52. Hironaka, Y.; Kubota, K.; Komaba, S., P2-and P3-Kxcoo2 as an Electrochemical Potassium Intercalation Host. *Chem. Commun.* **2017,** *53* (26), 3693-3696.

53. Vaalma, C.; Giffin, G. A.; Buchholz, D.; Passerini, S., Non-Aqueous K-Ion Battery Based on Layered K0.3mno2 and Hard Carbon/Carbon Black. *J. Electrochem. Soc.* **2016,** *163* (7), A1295-A1299.

54. Yabuuchi, N.; Kajiyama, M.; Iwatate, J.; Nishikawa, H.; Hitomi, S.; Okuyama, R.; Usui, R.; Yamada, Y.; Komaba, S., P2-Type Na-X[Fe1/2mn1/2]O-2 Made from Earth-Abundant Elements for Rechargeable Na Batteries. *Nat. Mater.* **2012,** *11* (6), 512-517.

55. Mathew, V.; Kim, S.; Kang, J.; Gim, J.; Song, J.; Baboo, J. P.; Park, W.; Ahn, D.; Han, J.; Gu, L.; Wang, Y. S.; Hu, Y. S.; Sun, Y. K.; Kim, J., Amorphous Iron Phosphate: Potential Host for Various Charge Carrier Ions. *Npg Asia Mater* **2014,** *6*.

56. Chen, Y. N.; Luo, W.; Carter, M.; Zhou, L. H.; Dai, J. Q.; Fu, K.; Lacey, S.; Li, T.; Wan, J. Y.; Han, X. G.; Bao, Y. P.; Hu, L. B., Organic Electrode for Non-Aqueous Potassium-Ion Batteries. *Nano Energy* **2015,** *18*, 205-211.

57. Lota, G.; Fic, K.; Frackowiak, E., Alkali Metal Iodide/Carbon Interface as a Source of Pseudocapacitance. *Electrochem. Commun.* **2011,** *13* (1), 38-41.

58. Lota, G.; Frackowiak, E., Striking Capacitance of Carbon/Iodide Interface. *Electrochem. Commun.* **2009,** *11* (1), 87-90.

59. Senthilkumar, S. T.; Selvan, R. K.; Lee, Y. S.; Melo, J. S., Electric Double Layer Capacitor and Its Improved Specific Capacitance Using Redox Additive Electrolyte. *J. Mater. Chem. A* **2013,** *1* (4), 1086-1095.

60. Senthilkumar, S. T.; Selvan, R. K.; Ponpandian, N.; Melo, J. S.; Lee, Y. S., Improved Performance of Electric Double Layer Capacitor Using Redox Additive (Vo2+/Vo2+) Aqueous Electrolyte. *J. Mater. Chem. A* **2013,** *1* (27), 7913-7919.

61. Wang, B.; Maciá-Agulló, J. A.; Prendiville, D. G.; Zheng, X.; Liu, D.; Zhang, Y.; Boettcher, S. W.; Ji, X.; Stucky, G. D., A Hybrid Redox-Supercapacitor System with Anionic Catholyte and Cationic Anolyte. *Journal of the Electrochemical Society* **2014,** *161* (6), A1090-A1093.

62. Roldan, S.; Blanco, C.; Granda, M.; Menendez, R.; Santamaria, R., Towards a Further Generation of High-Energy Carbon-Based Capacitors by Using Redox-Active Electrolytes. *Angew Chem Int Edit* **2011,** *50* (7), 1699-1701.

63. Roldan, S.; Gonzalez, Z.; Blanco, C.; Granda, M.; Menendez, R.; Santamaria, R., Redox-Active Electrolyte for Carbon Nanotube-Based Electric Double Layer Capacitors. *Electrochim. Acta* **2011,** *56* (9), 3401-3405.

64. Roldan, S.; Granda, M.; Menendez, R.; Santamaria, R.; Blanco, C., Supercapacitor Modified with Methylene Blue as Redox Active Electrolyte. *Electrochim. Acta* **2012,** *83*, 241-246.

65. Demarconnay, L.; Raymundo-Pinero, E.; Beguin, F., A Symmetric Carbon/Carbon Supercapacitor Operating at 1.6 V by Using a Neutral Aqueous Solution. *Electrochem. Commun.* **2010,** *12* (10), 1275-1278.

66. Fic, K.; Lota, G.; Meller, M.; Frackowiak, E., Novel Insight into Neutral Medium as Electrolyte for High-Voltage Supercapacitors. *Energy Environ. Sci.* **2012,** *5* (2), 5842-5850.

67. Brousse, T.; Toupin, M.; Belanger, D., A Hybrid Activated Carbon-Manganese Dioxide Capacitor Using a Mild Aqueous Electrolyte. *J. Electrochem. Soc.* **2004,** *151* (4), A614-A622.

68. Ovshinsky, S. R.; Fetcenko, M. A.; Ross, J., A Nickel Metal Hydride Battery for Electric Vehicles. *Science* **1993,** *260* (5105), 176-181.

69. Nutzenadel, C.; Zuttel, A.; Chartouni, D.; Schlapbach, L., Electrochemical Storage of Hydrogen in Nanotube Materials. *Electrochem Solid St* **1999,** *2* (1), 30-32.

70. Rajalakshmi, N.; Dhathathreyan, K. S.; Govindaraj, A.; Satishkumar, B. C., Electrochemical Investigation of Single-Walled Carbon Nanotubes for Hydrogen Storage. *Electrochim. Acta* **2000,** *45* (27), 4511-4515.

71. Jurewicz, K.; Frackowiak, E.; Beguin, F., Enhancement of Reversible Hydrogen Capacity into Activated Carbon through Water Electrolysis. *Electrochem Solid St* **2001,** *4* (3), A27-A29.

72. Jurewicz, K.; Frackowiak, E.; Beguin, F., Towards the Mechanism of Electrochemical Hydrogen Storage in Nanostructured Carbon Materials. *Appl Phys a-Mater* **2004,** *78* (7), 981-987.

73. Qu, D. Y., Mechanism for Electrochemical Hydrogen Insertion in Carbonaceous Materials. *J. Power Sources* **2008,** *179* (1), 310-316.

74. Trasatti, S.; Buzzanca, G., Ruthenium Dioxide: A New Interesting Electrode Material. Solid State Structure and Electrochemical Behaviour. *Journal of Electroanalytical Chemistry and Interfacial Electrochemistry* **1971,** *29* (2), A1-A5.

75. Santos, M. C.; Terezo, A. J.; Fernandes, V. C.; Pereira, E. C.; Bulhoes, L. O. S., An Eqcm Investigation of Charging Ruo2 Thin Films Prepared by the Polymeric Precursor Method. *J. Solid State Electrochem.* **2005,** *9* (2), 91-95.

76. Fultz, B.; Howe, J. M., *Transmission Electron Microscopy and Diffractometry of Materials*. Springer Science & Business Media: 2012.

77. Scherrer, P., Bestimmung Der Größe Und Der Inneren Struktur Von Kolloidteilchen Mittels Röntgenstrahlen. *Nachrichten von der Gesellschaft der Wissenschaften zu Göttingen, Mathematisch-Physikalische Klasse* **1918,** *2*, 98-100.

78. Sing, K. S. W., Adsorption Methods for the Characterization of Porous Materials. *Adv. Colloid Interface Sci.* **1998,** *76*, 3-11.

79. Donohue, M. D.; Aranovich, G. L., Classification of Gibbs Adsorption Isotherms. *Adv. Colloid Interface Sci.* **1998,** *76*, 137-152.

80. ALOthman, Z. A., A Review: Fundamental Aspects of Silicate Mesoporous Materials. *Materials* **2012,** *5* (12), 2874-2902.

81. Schrader, B., *Infrared and Raman Spectroscopy: Methods and Applications*. John Wiley & Sons: 2008.

82. Suart, B., Infrared Spectroscopy: Fundamental and Applications. John Wiley & Sons, Ltd: 2004.

83. Embong, Z.; Raja, P.; Pahat, B., Xps, Aes and Laser Raman Spectroscopy: A Fingerprint for a Materials Surface Characterisation. *Jurnal Sains Nuklear Malaysia* **2011,** *23* (2), pp. 26-45.

84. Van der Heide, P., *X-Ray Photoelectron Spectroscopy: An Introduction to Principles and Practices*. John Wiley & Sons: 2011.

85. Stojilovic, N., Why Can't We See Hydrogen in X-Ray Photoelectron Spectroscopy? *J. Chem. Educ.* **2012,** *89* (10), 1331-1332.

86. Bard, A. J.; Fraulkner, L. R., *Electrochemical Methods: Fundamentals and Applications*. 2nd ed.; John Wiley & Sons, Inc.: New York, 2001.

87. Kuperman, A.; Aharon, I., Battery-Ultracapacitor Hybrids for Pulsed Current Loads: A Review. *Renewable Sustainable Energy Rev.* **2011,** *15* (2), 981-992.

88. Yoda, S.; Ishihara, K., The Advent of Battery-Based Societies and the Global Environment in the 21st Century. *J. Power Sources* **1999,** *81*, 162-169.

89. Kotz, R.; Carlen, M., Principles and Applications of Electrochemical Capacitors. *Electrochim. Acta* **2000,** *45* (15-16), 2483-2498.

90. Zhang, Y.; Feng, H.; Wu, X. B.; Wang, L. Z.; Zhang, A. Q.; Xia, T. C.; Dong, H. C.; Li, X. F.; Zhang, L. S., Progress of Electrochemical Capacitor Electrode Materials: A Review. *Int. J. Hydrogen Energy* **2009,** *34* (11), 4889-4899.

91. Frackowiak, E.; Khomenko, V.; Jurewicz, K.; Lota, K.; Beguin, F., Supercapacitors Based on Conducting Polymers/Nanotubes Composites. *J. Power Sources* **2006,** *153* (2), 413-418.

92. Lee, S. W.; Chen, S. O.; Sheng, W. C.; Yabuuchi, N.; Kim, Y. T.; Mitani, T.; Vescovo, E.; Shao-Horn, Y., Roles of Surface Steps on Pt Nanoparticles in Electro-Oxidation of Carbon Monoxide and Methanol. *J. Am. Chem. Soc.* **2009,** *131* (43), 15669-15677.

93. Wang, X. F.; Raju, V.; Luo, W.; Wang, B.; Stickle, W. F.; Ji, X. L., Ambient Hydrolysis Deposition of Tio2 in Nanoporous Carbon and the Converted Tin-Carbon Capacitive Electrode. *J. Mater. Chem. A* **2014,** *2* (9), 2901-2905.

94. Hantel, M. M.; Kaspar, T.; Nesper, R.; Wokaun, A.; Kotz, R., Partially Reduced Graphite Oxide for Supercapacitor Electrodes: Effect of Graphene Layer Spacing and Huge Specific Capacitance. *Electrochem. Commun.* **2011,** *13* (1), 90-92.

95. Futaba, D. N.; Hata, K.; Yamada, T.; Hiraoka, T.; Hayamizu, Y.; Kakudate, Y.; Tanaike, O.; Hatori, H.; Yumura, M.; Iijima, S., Shape-Engineerable and Highly Densely Packed Single-Walled Carbon Nanotubes and Their Application as Super-Capacitor Electrodes. *Nat. Mater.* **2006,** *5* (12), 987-994.

96. Liu, C. G.; Yu, Z. N.; Neff, D.; Zhamu, A.; Jang, B. Z., Graphene-Based Supercapacitor with an Ultrahigh Energy Density. *Nano Lett.* **2010,** *10* (12), 4863-4868.

97. Gogotsi, Y.; Nikitin, A.; Ye, H. H.; Zhou, W.; Fischer, J. E.; Yi, B.; Foley, H. C.; Barsoum, M. W., Nanoporous Carbide-Derived Carbon with Tunable Pore Size. *Nat. Mater.* **2003,** *2* (9), 591-594.

98. Zhu, Y. W.; Murali, S.; Stoller, M. D.; Ganesh, K. J.; Cai, W. W.; Ferreira, P. J.; Pirkle, A.; Wallace, R. M.; Cychosz, K. A.; Thommes, M.; Su, D.; Stach, E. A.; Ruoff, R. S., Carbon-Based Supercapacitors Produced by Activation of Graphene. *Science* **2011,** *332* (6037), 1537-1541.

99. Lee, S. W.; Kim, B. S.; Chen, S.; Shao-Horn, Y.; Hammond, P. T., Layer-by-Layer Assembly of All Carbon Nanotube Ultrathin Films for Electrochemical Applications. *J. Am. Chem. Soc.* **2009,** *131* (2), 671-679.

100. Jiang, D. E.; Wu, J. Z., Microscopic Insights into the Electrochemical Behavior of Nonaqueous Electrolytes in Electric Double-Layer Capacitors. *J. Phys. Chem. Lett.* **2013,** *4* (8), 1260-1267.

101. Jiang, D. E.; Jin, Z. H.; Henderson, D.; Wu, J. Z., Solvent Effect on the Pore-Size Dependence of an Organic Electrolyte Supercapacitor. *J. Phys. Chem. Lett.* **2012,** *3* (13), 1727-1731.

102. Augustyn, V.; Simon, P.; Dunn, B., Pseudocapacitive Oxide Materials for High-Rate Electrochemical Energy Storage. *Energ Environ Sci* **2014,** *7* (5), 1597-1614.

103. Malinauskas, A.; Malinauskiene, J.; Ramanavicius, A., Conducting Polymer-Based Nanostructurized Materials: Electrochemical Aspects. *Nanotechnology* **2005,** *16* (10), R51-R62.

104. Peng, C.; Jin, J.; Chen, G. Z., A Comparative Study on Electrochemical Co-Deposition and Capacitance of Composite Films of Conducting Polymers and Carbon Nanotubes. *Electrochim. Acta* **2007,** *53* (2), 525-537.

105. Sugimoto, W.; Yokoshima, K.; Murakami, Y.; Takasu, Y., Charge Storage Mechanism of Nanostructured Anhydrous and Hydrous Ruthenium-Based Oxides. *Electrochim. Acta* **2006,** *52* (4), 1742-1748.

106. Qu, L. B.; Zhao, Y. L.; Khan, A. M.; Han, C. H.; Hercule, K. M.; Yan, M. Y.; Liu, X. Y.; Chen, W.; Wang, D. D.; Cai, Z. Y.; Xu, W. W.; Zhao, K. N.; Zheng, X. L.; Mai, L. Q., Interwoven Three-Dimensional Architecture of Cobalt Oxide Nanobrush-Graphene@$Ni_xco_{2x}(Oh)_{6x}$ for High-Performance Supercapacitors. *Nano Lett.* **2015,** *15* (3), 2037-2044.

107. Ahn, Y. R.; Song, M. Y.; Jo, S. M.; Park, C. R.; Kim, D. Y., Electrochemical Capacitors Based on Electrodeposited Ruthenium Oxide on Nanofibre Substrates. *Nanotechnology* **2006,** *17* (12), 2865-2869.

108. Mastragostino, M.; Arbizzani, C.; Soavi, F., Polymer-Based Supercapacitors. *J. Power Sources* **2001,** *97-8*, 812-815.

109. Jiang, J. H.; Kucernak, A., Electrochemical Supercapacitor Material Based on Manganese Oxide: Preparation and Characterization. *Electrochim. Acta* **2002,** *47* (15), 2381-2386.

110. Nelson, P. A.; Owen, J. R., A High-Performance Supercapacitor/Battery Hybrid Incorporating Templated Mesoporous Electrodes. *J. Electrochem. Soc.* **2003,** *150* (10), A1313-A1317.

111. Hibino, M.; Abe, K.; Mochizuki, M.; Miyayama, M., Amorphous Titanium Oxide Electrode for High-Rate Discharge and Charge. *J. Power Sources* **2004,** *126* (1-2), 139-143.

112. Hu, C. C.; Huang, C. M.; Chang, K. H., Anodic Deposition of Porous Vanadium Oxide Network with High Power Characteristics for Pseudocapacitors. *J. Power Sources* **2008,** *185* (2), 1594-1597.

113. Chen, P. C.; Shen, G. Z.; Shi, Y.; Chen, H. T.; Zhou, C. W., Preparation and Characterization of Flexible Asymmetric Supercapacitors Based on Transition-Metal-Oxide Nanowire/Single-Walled Carbon Nanotube Hybrid Thin-Film Electrodes. *ACS Nano* **2010,** *4* (8), 4403-4411.

114. Brezesinski, T.; Wang, J.; Senter, R.; Brezesinski, K.; Dunn, B.; Tolbert, S. H., On the Correlation between Mechanical Flexibility, Nanoscale Structure, and Charge Storage in Periodic Mesoporous Ceo2 Thin Films. *ACS Nano* **2010,** *4* (2), 967-977.

115. Roldan, S.; Blanco, C.; Granda, M.; Menendez, R.; Santamaria, R., Towards a Further Generation of High-Energy Carbon-Based Capacitors by Using Redox-Active Electrolytes. *Angew. Chem. Int. Ed.* **2011,** *50* (7), 1699-1701.

116. Tomai, T.; Mitani, S.; Komatsu, D.; Kawaguchi, Y.; Honma, I., Metal-Free Aqueous Redox Capacitor Via Proton Rocking-Chair System in an Organic-Based Couple. *Sci. Rep.* **2014,** *4*.

117. Mai, L. Q.; Minhas-Khan, A.; Tian, X. C.; Hercule, K. M.; Zhao, Y. L.; Lin, X.; Xu, X., Synergistic Interaction between Redox-Active Electrolyte and Binder-Free Functionalized Carbon for Ultrahigh Supercapacitor Performance. *Nat. Commun.* **2013,** *4*.

118. Senthilkumar, S. T.; Selvan, R. K.; Lee, Y. S.; Melo, J. S., Electric Double Layer Capacitor and Its Improved Specific Capacitance Using Redox Additive Electrolyte. *J Mater Chem A* **2013,** *1* (4), 1086-1095.

119. Yu, H. Y.; Wu, J. H.; Fan, L. Q.; Xu, K. Q.; Zhong, X.; Lin, Y. Z.; Lin, J. M., Improvement of the Performance for Quasi-Solid-State Supercapacitor by Using Pva-Koh-Ki Polymer Gel Electrolyte. *Electrochim. Acta* **2011,** *56* (20), 6881-6886.

120. Fic, K.; Meller, M.; Frackowiak, E., Interfacial Redox Phenomena for Enhanced Aqueous Supercapacitors. *J. Electrochem. Soc.* **2015,** *162* (5), A5140-A5147.

121. Simon, P.; Gogotsi, Y., Materials for Electrochemical Capacitors. *Nat. Mater.* **2008,** *7* (11), 845-854.

122. Noked, M.; Soffer, A.; Aurbach, D., The Electrochemistry of Activated Carbonaceous Materials: Past, Present, and Future. *J. Solid State Electrochem.* **2011,** *15* (7-8), 1563-1578.

123. Katsounaros, I.; Cherevko, S.; Zeradjanin, A. R.; Mayrhofer, K. J. J., Oxygen Electrochemistry as a Cornerstone for Sustainable Energy Conversion. *Angew Chem Int Edit* **2014,** *53* (1), 102-121.

124. Parent, A. R.; Crabtree, R. H.; Brudvig, G. W., Comparison of Primary Oxidants for Water-Oxidation Catalysis. *Chem. Soc. Rev.* **2013,** *42* (6), 2247-2252.

125. Li, C.; White, C., Kinetics of Hypoiodite Decomposition. *J. Am. Chem. Soc.* **1943,** *65* (3), 335-339.

126. Buxton, G. V.; Mulazzani, Q. G., On the Hydrolysis of Iodine in Alkaline Solution: A Radiation Chemical Study. *Radiat. Phys. Chem.* **2007,** *76* (6), 932-940.

127. Wren, J. C.; Paquette, J.; Sunder, S.; Ford, B. L., Iodine Chemistry in the +1 Oxidation-State .2. A Raman and Uv-Visible Spectroscopic Study of the Disproportionation of Hypoiodite in Basic Solutions. *Canadian Journal Of Chemistry-Revue Canadienne De Chimie* **1986,** *64* (12), 2284-2296.

128. Jurewicz, K.; Frackowiak, E.; Beguin, F., Towards the Mechanism of Electrochemical Hydrogen Storage in Nanostructured Carbon Materials. *Appl. Phys. A: Mater. Sci. Process.* **2004,** *78* (7), 981-987.

129. Beguin, F.; Friebe, M.; Jurewicz, K.; Vix-Guterl, C.; Dentzer, J.; Frackowiak, E., State of Hydrogen Electrochemically Stored Using Nanoporous Carbons as Negative Electrode Materials in an Aqueous Medium. *Carbon* **2006,** *44* (12), 2392-2398.

130. Raju, V.; Rains, J.; Gates, C.; Luo, W.; Wang, X. F.; Stickle, W. F.; Stucky, G. D.; Ji, X. L., Superior Cathode of Sodium-Ion Batteries: Orthorhombic V2o5 Nanoparticles Generated in Nanoporous Carbon by Ambient Hydrolysis Deposition. *Nano Lett.* **2014,** *14* (7), 4119-4124.

131. Conway, B. E.; Pell, W. G.; Liu, T. C., Diagnostic Analyses for Mechanisms of Self-Discharge of Electrochemical Capacitors and Batteries. *J. Power Sources* **1997,** *65* (1-2), 53-59.

132. Ricketts, B. W.; Ton-That, C., Self-Discharge of Carbon-Based Supercapacitors with Organic Electrolytes. *J. Power Sources* **2000,** *89* (1), 64-69.

133. Miller, J. R.; Simon, P., Materials Science - Electrochemical Capacitors for Energy Management. *Science* **2008,** *321* (5889), 651-652.

134. Miller, J. R.; Outlaw, R. A.; Holloway, B. C., Graphene Double-Layer Capacitor with Ac Line-Filtering Performance. *Science* **2010,** *329* (5999), 1637-1639.

135. Li, Q.; Jiang, R. R.; Dou, Y. Q.; Wu, Z. X.; Huang, T.; Feng, D.; Yang, J. P.; Yu, A. S.; Zhao, D. Y., Synthesis of Mesoporous Carbon Spheres with a Hierarchical Pore Structure for the Electrochemical Double-Layer Capacitor. *Carbon* **2011,** *49* (4), 1248-1257.

136. Zhai, Y. P.; Dou, Y. Q.; Zhao, D. Y.; Fulvio, P. F.; Mayes, R. T.; Dai, S., Carbon Materials for Chemical Capacitive Energy Storage. *Adv. Mater.* **2011,** *23* (42), 4828-4850.

137. Xing, Z. Y.; Wang, B.; Gao, W. Y.; Pan, C. Q.; Halsted, J. K.; Chong, E. S.; Lu, J.; Wang, X. F.; Luo, W.; Chang, C. H.; Wen, Y. H.; Ma, S. Q.; Amine, K.; Ji, X. L.,

Reducing Co2 to Dense Nanoporous Graphene by Mg/Zn for High Power Electrochemical Capacitors. *Nano Energy* **2015,** *11*, 600-610.

138. Chmiola, J.; Largeot, C.; Taberna, P. L.; Simon, P.; Gogotsi, Y., Desolvation of Ions in Subnanometer Pores and Its Effect on Capacitance and Double-Layer Theory. *Angew Chem Int Edit* **2008,** *47* (18), 3392-3395.

139. Li, W. R.; Chen, D. H.; Li, Z.; Shi, Y. F.; Wan, Y.; Wang, G.; Jiang, Z. Y.; Zhao, D. Y., Nitrogen-Containing Carbon Spheres with Very Large Uniform Mesopores: The Superior Electrode Materials for Edlc in Organic Electrolyte. *Carbon* **2007,** *45* (9), 1757-1763.

140. Bichat, M. P.; Raymundo-Pinero, E.; Beguin, F., High Voltage Supercapacitor Built with Seaweed Carbons in Neutral Aqueous Electrolyte. *Carbon* **2010,** *48* (15), 4351-4361.

141. Candelaria, S. L.; Garcia, B. B.; Liu, D. W.; Cao, G. Z., Nitrogen Modification of Highly Porous Carbon for Improved Supercapacitor Performance. *J. Mater. Chem.* **2012,** *22* (19), 9884-9889.

142. Huang, Y. X.; Candelaria, S. L.; Li, Y. W.; Li, Z. M.; Tian, J. J.; Zhang, L. L.; Cao, G. Z., Sulfurized Activated Carbon for High Energy Density Supercapacitors. *J. Power Sources* **2014,** *252*, 90-97.

143. Deng, Y.; Xie, Y.; Zou, K.; Ji, X., Review on Recent Advances in Nitrogen-Doped Carbons: Preparations and Applications in Supercapacitors. *J. Mater. Chem. A* **2016,** *4* (4), 1144-1173.

144. Brezesinski, K.; Wang, J.; Haetge, J.; Reitz, C.; Steinmueller, S. O.; Tolbert, S. H.; Smarsly, B. M.; Dunn, B.; Brezesinski, T., Pseudocapacitive Contributions to Charge Storage in Highly Ordered Mesoporous Group V Transition Metal Oxides with Iso-Oriented Layered Nanocrystalline Domains. *J. Am. Chem. Soc.* **2010,** *132* (20), 6982-6990.

145. Hu, L. B.; Chen, W.; Xie, X.; Liu, N. A.; Yang, Y.; Wu, H.; Yao, Y.; Pasta, M.; Alshareef, H. N.; Cui, Y., Symmetrical Mno2-Carbon Nanotube-Textile Nanostructures for Wearable Pseudocapacitors with High Mass Loading. *ACS Nano* **2011,** *5* (11), 8904-8913.

146. Mai, L. Q.; Yang, F.; Zhao, Y. L.; Xu, X.; Xu, L.; Luo, Y. Z., Hierarchical Mnmoo4/Comoo4 Heterostructured Nanowires with Enhanced Supercapacitor Performance. *Nat. Commun.* **2011,** *2*.

147. Augustyn, V.; Come, J.; Lowe, M. A.; Kim, J. W.; Taberna, P. L.; Tolbert, S. H.; Abruna, H. D.; Simon, P.; Dunn, B., High-Rate Electrochemical Energy Storage through Li+ Intercalation Pseudocapacitance. *Nat. Mater.* **2013,** *12* (6), 518-522.

148. Leng, K.; Zhang, F.; Zhang, L.; Zhang, T. F.; Wu, Y. P.; Lu, Y. H.; Huang, Y.; Chen, Y. S., Graphene-Based Li-Ion Hybrid Supercapacitors with Ultrahigh Performance. *Nano Res* **2013,** *6* (8), 581-592.

149. Meng, F. L.; Fang, Z. G.; Li, Z. X.; Xu, W. W.; Wang, M. J.; Liu, Y. P.; Zhang, J.; Wang, W. R.; Guo, X. H., Porous Co3o4 Materials Prepared by Solid-State Thermolysis of a Novel Co-Mof Crystal and Their Superior Energy Storage Performances for Supercapacitors (Vol 1, Pg 7235, 2013). *J. Mater. Chem. A* **2013,** *1* (48), 15554-15554.

150. Jian, Z. L.; Raju, V.; Li, Z. F.; Xing, Z. Y.; Hu, Y. S.; Ji, X. L., A High-Power Symmetric Na-Ion Pseudocapacitor. *Adv. Funct. Mater.* **2015,** *25* (36), 5778-5785.

151. Wang, B.; Macia-Agullo, J. A.; Prendiville, D. G.; Zheng, X.; Liu, D.; Zhang, Y.; Boettcher, S. W.; Ji, X.; Stucky, G. D., A Hybrid Redox-Supercapacitor System with Anionic Catholyte and Cationic Anolyte. *J. Electrochem. Soc.* **2014,** *161* (6), A1090-A1093.

152. Wang, X. F.; Chandrabose, R. S.; Chun, S. E.; Zhang, T. Q.; Evanko, B.; Jian, Z. L.; Boettcher, S. W.; Stucky, G. D.; Ji, X. L., High Energy Density Aqueous Electrochemical Capacitors with a Ki-Koh Electrolyte. *Acs Appl Mater Inter* **2015,** *7* (36), 19978-19985.

153. Chun, S. E.; Evanko, B.; Wang, X. F.; Vonlanthen, D.; Ji, X. L.; Stucky, G. D.; Boettcher, S. W., Design of Aqueous Redox-Enhanced Electrochemical Capacitors with High Specific Energies and Slow Self-Discharge. *Nat. Commun.* **2015,** *6*.

154. Gyenge, E.; Jung, J.; Mahato, B., Electroplated Reticulated Vitreous Carbon Current Collectors for Lead-Acid Batteries: Opportunities and Challenges. *J. Power Sources* **2003,** *113* (2), 388-395.

155. Suo, L.; Borodin, O.; Gao, T.; Olguin, M.; Ho, J.; Fan, X.; Luo, C.; Wang, C.; Xu, K., "Water-in-Salt" Electrolyte Enables High-Voltage Aqueous Lithium-Ion Chemistries. *Science* **2015,** *350* (6263), 938-943.

156. Fic, K.; Meller, M.; Menzel, J.; Frackowiak, E., Around the Thermodynamic Limitations of Supercapacitors Operating in Aqueous Electrolytes. *Electrochim. Acta* **2016,** *206*, 496-503.

157. Mani, K. N., Electrodialysis Water Splitting Technology. *J. Membr. Sci.* **1991,** *58* (2), 117-138.

158. Varcoe, J. R.; Slade, R. C. T., Prospects for Alkaline Anion-Exchange Membranes in Low Temperature Fuel Cells. *Fuel Cells* **2005,** *5* (2), 187-200.

159. Mazrou, S.; Kerdjoudj, H.; Cherif, A. T.; Elmidaoui, A.; Molenat, J., Regeneration of Hydrochloric Acid and Sodium Hydroxide with Bipolar Membrane Electrodialysis from Pure Sodium Chloride. *New J. Chem.* **1998,** *22* (4), 355-359.

160. Blackburn, J. W., Electrodialysis Applications for Pollution Prevention in the Chemical Processing Industry. *J. Air Waste Manage. Assoc.* **1999,** *49* (8), 934-942.

161. Weingarth, D.; Noh, H.; Foelske-Schmitz, A.; Wokaun, A.; Kotz, R., A Reliable Determination Method of Stability Limits for Electrochemical Double Layer Capacitors. *Electrochim. Acta* **2013,** *103*, 119-124.

162. Xu, K.; Ding, S. P.; Jow, T. R., Toward Reliable Values of Electrochemical Stability Limits for Electrolytes. *J. Electrochem. Soc.* **1999,** *146* (11), 4172-4178.

163. Laheaar, A.; Przygocki, P.; Abbas, Q.; Beguin, F., Appropriate Methods for Evaluating the Efficiency and Capacitive Behavior of Different Types of Supercapacitors. *Electrochem. Commun.* **2015,** *60*, 21-25.

164. Ji, X. L.; Lee, K. T.; Nazar, L. F., A Highly Ordered Nanostructured Carbon-Sulphur Cathode for Lithium-Sulphur Batteries. *Nat. Mater.* **2009,** *8* (6), 500-506.

165. Schuster, J.; He, G.; Mandlmeier, B.; Yim, T.; Lee, K. T.; Bein, T.; Nazar, L. F., Spherical Ordered Mesoporous Carbon Nanoparticles with High Porosity for Lithium-Sulfur Batteries. *Angew Chem Int Edit* **2012,** *51* (15), 3591-3595.

166. Zheng, G. Y.; Yang, Y.; Cha, J. J.; Hong, S. S.; Cui, Y., Hollow Carbon Nanofiber-Encapsulated Sulfur Cathodes for High Specific Capacity Rechargeable Lithium Batteries. *Nano Lett.* **2011,** *11* (10), 4462-4467.

167. Lu, J.; Lee, Y. J.; Luo, X. Y.; Lau, K. C.; Asadi, M.; Wang, H. H.; Brombosz, S.; Wen, J. G.; Zhai, D. Y.; Chen, Z. H.; Miller, D. J.; Jeong, Y. S.; Park, J. B.; Fang, Z. Z.; Kumar, B.; Salehi-Khojin, A.; Sun, Y. K.; Curtiss, L. A.; Amine, K., A Lithium-Oxygen Battery Based on Lithium Superoxide. *Nature* **2016,** *529* (7586), 377-+.

168. Peng, Z. Q.; Freunberger, S. A.; Chen, Y. H.; Bruce, P. G., A Reversible and Higher-Rate Li-O-2 Battery. *Science* **2012,** *337* (6094), 563-566.

169. Jian, Z. L.; Han, W. Z.; Lu, X.; Yang, H. X.; Hu, Y. S.; Zhou, J.; Zhou, Z. B.; Li, J. Q.; Chen, W.; Chen, D. F.; Chen, L. Q., Superior Electrochemical Performance and Storage Mechanism of Na3v2(Po4)3 Cathode for Room-Temperature Sodium-Ion Batteries. *Adv Energy Mater* **2013,** *3* (2), 156-160.

170. Ding, J.; Wang, H. L.; Li, Z.; Kohandehghan, A.; Cui, K.; Xu, Z. W.; Zahiri, B.; Tan, X. H.; Lotfabad, E. M.; Olsen, B. C.; Mitlin, D., Carbon Nanosheet Frameworks Derived from Peat Moss as High Performance Sodium Ion Battery Anodes. *ACS Nano* **2013,** *7* (12), 11004-11015.

171. Eftekhari, A.; Jian, Z.; Ji, X., Potassium Secondary Batteries. *Acs Appl Mater Inter* **2016**.

172. Zhang, W. C.; Han, S. M.; Hao, J. S.; Li, Y.; Bai, T. Y.; Zhang, J. W., Study on Kinetics and Electrochemical Properties of Low-Co Ab(5)-Type Alloys for High-Power Ni/Mh Battery. *Electrochim. Acta* **2009,** *54* (4), 1383-1387.

173. Leitner, K. W.; Gollas, B.; Winter, M.; Besenhard, J. O., Combination of Redox Capacity and Double Layer Capacitance in Composite Electrodes through Immobilization of an Organic Redox Couple on Carbon Black. *Electrochim. Acta* **2004,** *50* (1), 199-204.

174. Kalinathan, K.; DesRoches, D. P.; Liu, X. R.; Pickup, P. G., Anthraquinone Modified Carbon Fabric Supercapacitors with Improved Energy and Power Densities. *J. Power Sources* **2008,** *181* (1), 182-185.

175. Donald, W. A.; Leib, R. D.; Demireva, M.; O'Brien, J. T.; Prell, J. S.; Williams, E. R., Directly Relating Reduction Energies of Gaseous Eu(H2o)(N)(3+), N=55-140, to Aqueous Solution: The Absolute She Potential and Real Proton Solvation Energy. *J. Am. Chem. Soc.* **2009,** *131* (37), 13328-13337.

176. Marcus, Y., Volumes of Aqueous Hydrogen and Hydroxide Ions at 0 to 200 Degrees C. *J. Chem. Phys.* **2012,** *137* (15).

177. Shannon, R. D., Revised Effective Ionic-Radii and Systematic Studies of Interatomic Distances in Halides and Chalcogenides. *Acta Crystallogr A* **1976,** *32* (Sep1), 751-767.

178. Xing, Z.; Jian, Z.; Luo, W.; Qi, Y.; Bommier, C.; Chong, E. S.; Li, Z.; Hu, L.; Ji, X., A Perylene Anhydride Crystal as a Reversible Electrode for K-Ion Batteries. *Energy Storage Materials* **2016,** *2*, 63-68.

179. Jian, Z. L.; Liang, Y. L.; Rodriguez-Perez, I. A.; Yao, Y.; Ji, X. L., Poly(Anthraquinonyl Sulfide) Cathode for Potassium-Ion Batteries. *Electrochem. Commun.* **2016,** *71*, 5-8.

180. Rodríguez-Pérez, I. A.; Jian, Z.; Waldenmaier, P. K.; Palmisano, J. W.; Chandrabose, R. S.; Wang, X.; Lerner, M. M.; Carter, R. G.; Ji, X., A Hydrocarbon Cathode for Dual-Ion Batteries. *ACS Energy Letters* **2016,** *1* (4), 719-723.

181. Han, X. Y.; Chang, C. X.; Yuan, L. J.; Sun, T. L.; Sun, J. T., Aromatic Carbonyl Derivative Polymers as High-Performance Li-Ion Storage Materials. *Adv. Mater.* **2007,** *19* (12), 1616-+.

182. Luo, W.; Allen, M.; Raju, V.; Ji, X. L., An Organic Pigment as a High-Performance Cathode for Sodium-Ion Batteries. *Adv Energy Mater* **2014,** *4* (15).

183. Kresse, G.; Hafner, J., Ab Initiomolecular Dynamics for Liquid Metals. *Physical Review B* **1993,** *47* (1), 558-561.

184. Kresse, G.; Hafner, J., Ab Initiomolecular-Dynamics Simulation of the Liquid-Metal–Amorphous-Semiconductor Transition in Germanium. *Physical Review B* **1994,** *49* (20), 14251-14269.

185. Kresse, G.; Furthmüller, J., Efficient Iterative Schemes Forab Initiototal-Energy Calculations Using a Plane-Wave Basis Set. *Physical Review B* **1996,** *54* (16), 11169-11186.

186. Blöchl, P. E., Projector Augmented-Wave Method. *Physical Review B* **1994,** *50* (24), 17953-17979.

187. Kresse, G.; Joubert, D., From Ultrasoft Pseudopotentials to the Projector Augmented-Wave Method. *Physical Review B* **1999,** *59* (3), 1758-1775.

188. Perdew, J. P.; Burke, K.; Ernzerhof, M., Generalized Gradient Approximation Made Simple. *Physical Review Letters* **1996,** *77* (18), 3865-3868.

189. Grimme, S.; Antony, J.; Ehrlich, S.; Krieg, H., A Consistent and Accurate Ab Initio Parametrization of Density Functional Dispersion Correction (Dft-D) for the 94 Elements H-Pu. *The Journal of Chemical Physics* **2010,** *132* (15), 154104.

190. Grimme, S.; Ehrlich, S.; Goerigk, L., Effect of the Damping Function in Dispersion Corrected Density Functional Theory. *Journal of Computational Chemistry* **2011,** *32* (7), 1456-1465.

191. Monkhorst, H. J.; Pack, J. D., Special Points for Brillouin-Zone Integrations. *Physical Review B* **1976,** *13* (12), 5188-5192.

192. Tojo, K.; Mizuguchi, J., Refinement of the Crystal Structure of 3,4 : 9,10-Perylene-Bis(Dicarboximide), C24h10n2o4, at 263 K. *Z Krist-New Cryst St* **2002,** *217* (1), 45-46.

193. Tawa, G. J.; Topol, I. A.; Burt, S. K.; Caldwell, R. A.; Rashin, A. A., Calculation of the Aqueous Solvation Free Energy of the Proton. *J. Chem. Phys.* **1998,** *109* (12), 4852-4863.

194. Feng, X.; Fryxell, G. E.; Wang, L. Q.; Kim, A. Y.; Liu, J.; Kemner, K. M., Functionalized Monolayers on Ordered Mesoporous Supports. *Science* **1997,** *276* (5314), 923-926.

195. Tan, Z.; Sun, Z. H.; Wang, H. H.; Guo, Q.; Su, D. S., Fabrication of Porous Sn-C Composites with High Initial Coulomb Efficiency and Good Cyclic Performance for Lithium Ion Batteries. *J. Mater. Chem. A* **2013,** *1* (33), 9462-9468.

196. Sun, Z. H.; Wang, L. F.; Liu, P. P.; Wang, S. C.; Sun, B.; Jiang, D. Z.; Xiao, F. S., Magnetically Motive Porous Sphere Composite and Its Excellent Properties for the Removal of Pollutants in Water by Adsorption and Desorption Cycles. *Adv. Mater.* **2006,** *18* (15), 1968-+.

197. Tan, Z.; Sun, Z. H.; Guo, Q.; Wang, H. H.; Su, D. S., A Novel Ion-Exchange Method for the Synthesis of Nano-Sno/Micro-C Hybrid Structure as High Capacity Anode Material in Lithium Ion Batteries. *Journal of Materials Science & Technology* **2013,** *29* (7), 609-612.

198. Datta, M., Electrochemical Processing Technologies in Chip Fabrication: Challenges and Opportunities. *Electrochim. Acta* **2003,** *48* (20-22), 2975-2985.

199. Dubin, V.; Hong, K.; Baxter, N. Electroplating Bath Composition and Method of Using. US6893550 B2, 2005.

200. Menon, V. P.; Martin, C. R., Fabrication and Evaluation of Nanoelectrode Ensembles. *Anal. Chem.* **1995,** *67* (13), 1920-1928.

201. Schlesinger, M.; Paunovic, M., *Modern Electroplating*. John Wiley & Sons: 2011; Vol. 55.

202. Meyers, S. T.; Anderson, J. T.; Hong, D.; Hung, C. M.; Wager, J. F.; Keszler, D. A., Solution-Processed Aluminum Oxide Phosphate Thin-Film Dielectrics. *Chem. Mater.* **2007,** *19* (16), 4023-4029.

203. Marichy, C.; Bechelany, M.; Pinna, N., Atomic Layer Deposition of Nanostructured Materials for Energy and Environmental Applications. *Adv. Mater.* **2012,** *24* (8), 1017-1032.

204. Elam, J. W.; Routkevitch, D.; Mardilovich, P. P.; George, S. M., Conformal Coating on Ultrahigh-Aspect-Ratio Nanopores of Anodic Alumina by Atomic Layer Deposition. *Chem. Mater.* **2003,** *15* (18), 3507-3517.

205. King, D. M.; Spencer, J. A.; Liang, X.; Hakim, L. F.; Weimer, A. W., Atomic Layer Deposition on Particles Using a Fluidized Bed Reactor with in Situ Mass Spectrometry. *Surf. Coat. Technol.* **2007,** *201* (22-23), 9163-9171.

206. Sheridan, L. B.; Gebregziabiher, D. K.; Stickney, J. L.; Robinson, D. B., Formation of Palladium Nanofilms Using Electrochemical Atomic Layer Deposition (E-Ald) with Chloride Complexation. *Langmuir* **2013,** *29* (5), 1592-1600.

207. Colletti, L. P.; Flowers, B. H.; Stickney, J. L., Formation of Thin Films of Cdte, Cdse, and Cds by Electrochemical Atomic Layer Epitaxy. *J. Electrochem. Soc.* **1998,** *145* (5), 1442-1449.

208. Wan, Y.; Yang, H. F.; Zhao, D. Y., "Host-Guest" Chemistry in the Synthesis of Ordered Nonsiliceous Mesoporous Materials. *Acc. Chem. Res.* **2006,** *39* (7), 423-432.

209. Tian, B. Z.; Liu, X. Y.; Yang, H. F.; Xie, S. H.; Yu, C. Z.; Tu, B.; Zhao, D. Y., General Synthesis of Ordered Crystallized Metal Oxide Nanoarrays Replicated by Microwave-Digested Mesoporous Silica. *Adv. Mater.* **2003,** *15* (16), 1370-+.

210. Zhang, L.; Holt, C. M. B.; Luber, E. J.; Olsen, B. C.; Wang, H. T.; Danaie, M.; Cui, X. W.; Tan, X. H.; Lui, V. W.; Kalisvaart, W. P.; Mitlin, D., High Rate Electrochemical Capacitors from Three-Dimensional Arrays of Vanadium Nitride Functionalized Carbon Nanotubes. *J. Phys. Chem. C* **2011,** *115* (49), 24381-24393.

211. Striolo, A.; Chialvo, A. A.; Cummings, P. T.; Gubbins, K. E., Water Adsorption in Carbon-Slit Nanopores. *Langmuir* **2003,** *19* (20), 8583-8591.

212. Ohba, T.; Kanoh, H.; Kaneko, K., Affinity Transformation from Hydrophilicity to Hydrophobicity of Water Molecules on the Basis of Adsorption of Water in Graphitic Nanopores. *J. Am. Chem. Soc.* **2004,** *126* (5), 1560-1562.

213. Cailliez, F.; Trzpit, M.; Soulard, M.; Demachy, I.; Boutin, A.; Patarin, J.; Fuchs, A. H., Thermodynamics of Water Intrusion in Nanoporous Hydrophobic Solids. *PCCP* **2008,** *10* (32), 4817-4826.

214. Zhao, D. Y.; Feng, J. L.; Huo, Q. S.; Melosh, N.; Fredrickson, G. H.; Chmelka, B. F.; Stucky, G. D., Triblock Copolymer Syntheses of Mesoporous Silica with Periodic 50 to 300 Angstrom Pores. *Science* **1998,** *279* (5350), 548-552.

215. Jun, S.; Joo, S. H.; Ryoo, R.; Kruk, M.; Jaroniec, M.; Liu, Z.; Ohsuna, T.; Terasaki, O., Synthesis of New, Nanoporous Carbon with Hexagonally Ordered Mesostructure. *J. Am. Chem. Soc.* **2000,** *122* (43), 10712-10713.

216. Wei, L.; Sevilla, M.; Fuertes, A. B.; Mokaya, R.; Yushin, G., Hydrothermal Carbonization of Abundant Renewable Natural Organic Chemicals for High-Performance Supercapacitor Electrodes. *Adv Energy Mater* **2011,** *1* (3), 356-361.

217. Simon, P.; Gogotsi, Y., Capacitive Energy Storage in Nanostructured Carbon-Electrolyte Systems. *Acc. Chem. Res.* **2013,** *46* (5), 1094-1103.

218. Cheng, H. H.; Dong, Z. L.; Hu, C. G.; Zhao, Y.; Hu, Y.; Qu, L. T.; Chena, N.; Dai, L. M., Textile Electrodes Woven by Carbon Nanotube-Graphene Hybrid Fibers for Flexible Electrochemical Capacitors. *Nanoscale* **2013,** *5* (8), 3428-3434.

219. Wen, Z. H.; Wang, X. C.; Mao, S.; Bo, Z.; Kim, H.; Cui, S. M.; Lu, G. H.; Feng, X. L.; Chen, J. H., Crumpled Nitrogen-Doped Graphene Nanosheets with Ultrahigh Pore Volume for High-Performance Supercapacitor. *Adv. Mater.* **2012,** *24* (41), 5610-5616.

220. Zhao, L.; Fan, L. Z.; Zhou, M. Q.; Guan, H.; Qiao, S. Y.; Antonietti, M.; Titirici, M. M., Nitrogen-Containing Hydrothermal Carbons with Superior Performance in Supercapacitors. *Adv. Mater.* **2010,** *22* (45), 5202-+.

221. Qie, L.; Chen, W. M.; Xu, H. H.; Xiong, X. Q.; Jiang, Y.; Zou, F.; Hu, X. L.; Xin, Y.; Zhang, Z. L.; Huang, Y. H., Synthesis of Functionalized 3d Hierarchical Porous Carbon for High-Performance Supercapacitors. *Energy Environ. Sci.* **2013,** *6* (8), 2497-2504.

222. Higgins, D. C.; Choi, J. Y.; Wu, J.; Lopez, A.; Chen, Z. W., Titanium Nitride-Carbon Nanotube Core-Shell Composites as Effective Electrocatalyst Supports for Low Temperature Fuel Cells. *J. Mater. Chem.* **2012,** *22* (9), 3727-3732.

223. Liu, X. Y.; Zhang, Y. H.; Wu, T.; Huang, J. G., Hierarchical Nanotubular Titanium Nitride Derived from Natural Cellulose Substance and Its Electrochemical Properties. *Chem. Commun.* **2012,** *48* (80), 9992-9994.

224. Choi, D.; Kumta, P. N., Nanocrystalline Tin Derived by a Two-Step Halide Approach for Electrochemical Capacitors. *J. Electrochem. Soc.* **2006,** *153* (12), A2298-A2303.

225. Lu, X. H.; Wang, G. M.; Zhai, T.; Yu, M. H.; Xie, S. L.; Ling, Y. C.; Liang, C. L.; Tong, Y. X.; Li, Y., Stabilized Tin Nanowire Arrays for High-Performance and Flexible Supercapacitors. *Nano Lett.* **2012,** *12* (10), 5376-5381.

226. Zukalova, M.; Prochazka, J.; Bastl, Z.; Duchoslav, J.; Rubacek, L.; Havlicek, D.; Kavan, L., Facile Conversion of Electrospun Tio2 into Titanium Nitride/Oxynitride Fibers. *Chem. Mater.* **2010,** *22* (13), 4045-4055.